Optimization of Image Quality in High-Resolution X-Ray Imaging

Dissertation zur Erlangung des
naturwissenschaftlichen Doktorgrades
der Julius-Maximilians-Universität Würzburg

vorgelegt von

Maximilian Ullherr

aus Nürnberg

Würzburg, 2020

Eingereicht am: .....
bei der Fakultät für Physik und Astronomie

1. Gutachter: .....
2. Gutachter: .....
3. Gutachter: .....
der Dissertation

Vorsitzende(r).....

1. Prüfer: .....
2. Prüfer: .....
3. Prüfer: .....
im Promotionkolloquium

Tag des Promotionskolloquiums: .....

Doktorurkunde ausgehändigt am: .....

Contents

Publications

The following three papers were published by the author of this work on the same topic:

[1] M. Ullherr et al. “Using measurements of the spatial SNR to optimize phase contrast X-ray imaging”. In: *Nucl Instr Meth A* 877 (2018), pp. 44–50. DOI: 10.1016/j.nima.2017.09.044

Introduces the SNR spectra measurement method for the application of optimizing the image quality of inline phase contrast measurements.

[2] M. Ullherr and S. Zabler. “SNR spectra as a quantitative model for image quality in polychromatic X-ray imaging”. In: *Nucl Instr Meth A* 943 (2019), p. 162385. ISSN: 0168-9002. DOI: 10.1016/j.nima.2019.162385. URL: https://arxiv.org/abs/1904.13313

Proposes SNR spectra as a theoretical model and demonstrates how polychromatic image quality works by using physical models and simulations.

[3] S. Zabler et al. “Comparing image quality in phase contrast submu X-ray tomography—A round-robin study”. In: *Nucl Instr Meth A* (2019), p. 162992. ISSN: 0168-9002. DOI: 10.1016/j.nima.2019.162992. URL: https://arxiv.org/abs/1905.02651
(as second author, responsible for theory and data evaluation)

Compares the performance of different sub-μ imaging setups using methods developed in the prior two publications.

In addition, two papers were published that are not about x-ray image quality but concern other topics within x-ray imaging:

[4] M. Ullherr and S. Zabler. “Correcting multi material artifacts from single material phase retrieved holo-tomograms with a simple 3D Fourier method”. In: *Optics Express* 23.25 (2015), pp. 32718–32727. DOI: 10.1364/OE.23.032718

A practical algorithm for phase retrieval of multi material samples using masked volume Fourier filters.

[5] S. Zabler et al. “Characterization of aluminum alloy microstructures by means of synchrotron X-ray micro-tomography – a simple toolchain for extracting quantitative 3D morphological features”. In: *Int. J. Mater. Res.* 110 (2019). DOI: 10.3139/146.111854

(as second author, responsible for evaluation method development)

An application of phase contrast micro-CT imaging to metal alloys, specifically concerning the material interface of Al and Si (e.g. alloys with 7 % and 12 % Si). Methods include the segmentation and separation of complexly shaped material areas in an alloy.

The text length of this document is 179.0 standard pages (1500 characters each), it has 46 figures and 7 tables.

1. Introduction

X-ray imaging is a measurement technique that has many applications, for example in medical imaging, nondestructive testing and material science. Due to the fact that matter is partially transparent for x-rays, they can be used to produce images of the inner structure of objects.

The aim of this work is to develop methods for the optimization of image quality of measurements with a high spatial resolution. Here, spatial resolutions below 5 µm are considered high resolution. Having a spatial resolution of a specific size means that image details of that size can be recognized in an image.

Commonly used image quality descriptions and measurement methods need to be extended to correctly model this area of x-ray imaging. To do so, a new and broader theoretical framework for image quality and a corresponding measurement method are developed in this work. Also emphasized is a direct correspondence between theory and measured quantities.

A high enough image quality is required to evaluate the spatial structures in a volume image. Improving the image quality is always possible by increasing the measurement time. In this work, the aim is to optimize an imaging setup for a higher image quality without increasing the measurement time. Optimizing the performance of an imaging device therefore means that the image quality per measurement time is optimized.

Imaging at a higher spatial resolution fundamentally requires a higher image quality. For volume imaging (computed tomography), many images ($>$ 1000) need to be acquired and a reduction of the measurement time is then important. The technical capabilities and the configuration of the measurement setup then decide if a measurement can be done in a realistic amount of time.

There are two applications of x-ray imaging for which publications about image quality exist: Medical imaging (MI) and (industrial) nondestructive testing (NDT). They have in common that the spatial resolutions used are (far) above high resolution and that larger samples and higher x-ray energy ranges are used.

The image quality models in MI and NDT focus more on standardization (of devices) and less on optimization. In this work, the focus is on optimization. Important for optimization are accuracy and completeness of the description For standardization, the focus is on comparability between devices and simplicity of the interpretation. Optimizations can be very application-specific, and the methods used here yield application-specific results for which comparability is optional. The concept here is that evaluating the image quality directly for different examples should yield more accurate results than an evaluation of device properties.

MI and NDT imaging almost exclusively use x-ray attenuation as the contrast mechanism that generates the sample structure visible in the image. For high resolution imaging, effects from spatially coherent x-rays are possible. The most common additional contrast mechanisms made possible by this are inline phase contrast, grating phase contrast and setups with various x-ray optics. To represent these effects, a more general model for x-ray image quality is developed in this work.

The higher x-ray energies of MI and NDT measurement mean that the energy-dependency of the amplitude of image features is often weak (Compton attenuation) while this dependency can be strong at lower energies (Photoeffect attenuation). This amplitude is also called contrast, in this work the more general concept of ”signal strength” is used instead.

Consequently, in MI, imaging performance is approximated to be independent of the signal the imaged object generates. For high resolution imaging, the signal strength strongly varies within the detected x-ray energy spectrum of the setup and this approximation no longer works. In particular, lower x-ray energies typically imply stronger signals—utilizing this fact may greatly increase image quality for very small samples.

This work is divided into three parts:

In the first chapter, I will briefly summarize the fundamentals of x-ray imaging and establish the necessary theoretical background for the rest of the work. This also serves to introduce the mathematical nota-

tion used. The first three sections do not include own work, but emphasize certain aspects of the topics and the application of certain theoretical frameworks to x-ray imaging may be new. Beginning with section 2.4.2, significant parts are own work.

The second chapter introduces a model for describing image quality in high resolution x-ray imaging. The proposed model is based on using SNR (signal to noise ratio) spectra as a quantitative description of image quality. While SNR spectra have been used in x-ray imaging before, here a more general definition is used, which includes the influence of the measured object. Superposition of signal and noise for different x-ray energies yields a polychromatic image quality model, which is used to predict how an experimental setup could be optimized.

The third chapter introduces a new method for directly measuring SNR spectra. It is used both to test the predictions of the prior chapter and also as a practical image quality optimization tool. Measuring SNR spectra is a powerful and useful method, but it does have measurement errors and the interpretation of the results can sometimes be difficult.

Altogether, optimizing high resolution x-ray imaging implies that the different contrast mechanisms are modeled and that the resulting image quality can be simulated accurately and measured reliably. Energy-dependencies of the signal also need to be considered. To achieve both aims, it is necessary to understand how a (polychromatic) signal is generated for all contrast mechanisms. Methods used in MI and NDT mainly consider the capabilities of the imaging device itself. In this work, both the properties of the sample and also the interactions between sample and device properties are additionally considered.

The main novel aspects of the methods described here are:

1. A much closer correspondence between image quality measurements and theory, including a novel measurement technique.

2. A clear theoretical description of polychromatic imaging – the effect of intensity superposition on image quality.

3. The possibility to include contrast mechanisms like phase contrast in the image quality measure.

4. Laying the focus on optimization instead of absolute quantification.

2. Fundamentals of x-ray imaging

2.1. Image Formation

2.1.1. Radiography

Radiography is a measurement process first discovered by W.C. Röntgen in 1895 [6]. The method works by shining x-ray light through an object and capturing the transmitted intensity on a two-dimensional imaging detector (film or digital). Refer e.g. to [7] section 4.11 for the fundamentals. X-ray imaging fundamentally works like any other imaging based on transmission of light through an absorbing medium. The main difference is that matter is comparatively transparent in the wavelength range of x-rays.

In a radiography image, the inner structure of the object is superimposed along the light direction (beam) in the resulting image and can thus be difficult to evaluate. This inner structure can be imaged with a computed tomography measurement process (see section 2.4), which in itself consists of a series of radiography measurements. Therefore, any discussion of the fundamentals of x-ray imaging must start with the radiography.

The two-dimensional x-ray image is measured by exposing a x-ray detector to the transmitted x-ray light for a specific time t and counting detection events. The number of these events is called the intensity $I(x)$ at pixel position x. Due to the fact that the base intensity of x-rays in the detector area is not constant, a so called reference intensity $I_\mathrm{r}(x)$ is measured without a sample in the beam. Additionally, the detector may produce intensity that does not originate from x-ray photons. This is called the dark intensity $I_d(x)$, it mainly stems from processes in the detector electronic (e.g. readout noise and dark current). The x-ray image $d(x)$ is thus computed as:

$$d(x) = \frac{I(x) - I_\mathrm{d}(x)}{I_\mathrm{r}(x) - I_\mathrm{d}(x)} \tag{2.1}$$

Attenuation x-ray imaging is a the case in which approximately the only interaction of the x-ray photons with matter are processes which directly reduce the detected intensity. For monochromatic x-rays, the x-ray image is then derived from the sum over the attenuation coefficient μ (units of inverse length) along the beam $r \in\!\!\rightarrow x$ that starts in the x-ray source and ends in the pixel x as (Lambert-Beer law):

$$d(x) = \exp\left(-\int_{\rightarrow x} \mathrm{d}r\mu(r))\right) \tag{2.2}$$

$$\Leftrightarrow \int_{\rightarrow x} \mathrm{d}r\mu(r) = -\ln\left(d(x)\right) \tag{2.3}$$

This is a formula for monochromatic x-rays. On the one hand, these equations can be used to compute the material thickness in the beam path, if $\mu(r)$ is known. On the other hand, the transparency of a sample is given by the Lambert-Beer law. Fundamentally, x-ray photons need to pass through the sample in order to allow imaging of the inner structure. A high transparency means that a higher number of x-ray photons contribute to the image, which results in lower noise.

In general, x-ray images can be generated by different physical processes (contrast mechanisms). They have in common that they somehow cause the sample to influence the x-ray image on the detector. On a more fundamental level, x-ray light interacts with matter it passes through. Independently of the contrast mechanism used, the information that one is interested in is usually the spatial density distributions of the different materials in the sample (sample shape). The most important contrast mechanisms are:

- X-ray attenuation: Different interactions between the x-ray photons and matter may result in a reduced detected intensity in the pixel that is along the beam between x-ray source and object. The possible interactions have different strengths and different effects are most important at different energy ranges:
  - Photoabsorption: Absorption of the x-ray photon in the sample material. Florescence emissions from such an absorption may also be detected.
    Low-energy interaction.
  - Scattering: Elastic (Rayleigh) or inelastic (Compton) scattering deflects the x-ray photons to another path. Reduces the detected intensity similar as absorption, but the scattered x-rays may be detected. Scattered x-rays originating not from the object but from

the measurement setup may also be detected as noise.
Higher energy interaction.

– Pair production.
Highest energy interaction (only above 1022 keV).

- Inline phase contrast (see section 2.1.2). Interference patterns in (partially) coherent x-ray images appear due to the wavefront deformation caused by the object in the beam. It increases the image quality through amplification of high spatial frequencies. Especially for materials with a weaker x-ray absorption (low atomic number), phase contrast is often the main contrast mechanism.

- X-ray optics [8], e.g. diffraction and refraction lenses or grating interferometers. The efficiency of a x-ray optic can strongly vary with the x-ray energy.

Note that "attenuation" describes all effects which reduce the intensity of the beam passing through matter, while the term "absorption" is used if the absorbed intensity is of interest (e.g. in an x-ray detector).

The standard geometry for x-ray imaging is a sample placed between a (point) source and a two-dimensional area detector. It is called cone beam, because the sample can be placed within a volume corresponding to a (rectangular) cone between source and detector edges. A top view sketch of this geometry is shown in fig. 2.1. In this geometry, the x-ray image is magnified by the x-ray magnification M is defined as:

$$M = \frac{l_{SDD}}{l_{SSD}} \tag{2.4}$$

with l_{SSD} the source sample distance and l_{SDD} the source detector distance. M defines the length scaling between the sample/voxel coordinates and the detector/pixel coordinates. This means that a sample structure of length l will be imaged on the x-ray detector with length Ml. Note that the magnification varies within a sample that extends in the beam direction.

Due to the inverse square law, the x-ray intensity per (pixel) area gets weaker the longer the distance between source and detector according to:

$$I(x) \propto \frac{1}{l_{SDD}^2} \tag{2.5}$$

Due to the effect discussed in section 3.6, the image quality is not changed by changing l_{SDD}, only the field of view is.

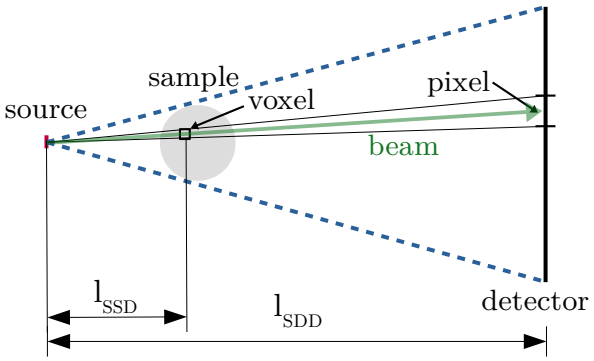

Figure 2.1.: Sketch for the cone geometry viewed from above. The gray area is also called the field of view (FOV) for a sample which is rotated in a CT (with centered rotational axis). The projection image is measured at the detector.

Polychromatic x-ray imaging is the situation where an image with a single color channel is generated by the superposition of contributions from different x-ray energies ("colors"). The resulting image value $d(x)$ is then also called "gray value". This can be written as a sum over the set of contributing energies $\{E\}$:

$$I_{\text{poly}} = \sum_{\{E\}} I_{\text{mono}}(E) \tag{2.6}$$

Note that in physics, there is usually no need to differentiate between sums and integrals, the equation above could be rewritten as an energy integral without changing the meaning. The only difference is that the integrand then would need to be (or include) a density.

All current technical implementations of x-ray sources suited for CT are polychromatic and can only be made monochromatic by filtering energy ranges from the beam or by only detecting specific energy ranges. The latter is a new approach made possible by direct x-ray detectors with multiple energy thresholds.

2.1.2. Inline phase contrast

Inline phase contrast (IPC) is an effect that appears in high-resolution x-ray imaging due to the constructive superposition of interference patterns of weakly coherent x-ray light [8]. In general, the term "phase contrast" is used to describe different imaging techniques that use (partially) coherent x-rays or optical elements in the beam (e.g. gratings). The inline phase contrast enhances image details and is therefore an effect that improves image quality. Depending on the experimental setup, phase contrast is the main effect which generates the image information and it

is therefore interesting to quantify this effect. The enhancement by phase contrast can be interpreted as a modulation transfer effect, but it is caused by the sample and not by the imaging setup.

The image quality models and methods chosen in this work were heavily influenced by the need to describe the image quality not only for attenuation x-ray imaging but also for phase contrast x-ray imaging.

The first practical application for inline phase contrast is [9] (in synchrotron imaging). It was later also used in laboratory setups, and is a common part of most x-ray imaging setups with spatial resolutions of a few µm and better [10].

Phase retrieval is a class of algorithms that reconstruct material properties (e.g. thickness in projections) from the measured interference pattern. In the case of weak phase contrast, this is a simple Fourier filter [11] applied to the projections. These algorithms typically are limited to single-material cases, samples having multiple materials with highly different atomic numbers can only have a correct phase retrieval for one material—the other will show artifacts. I developed an extension of this simple Fourier filter [4], which applies different filters in the regions corresponding to different materials. This algorithm is able to apply a phase retrieval to multi material samples, given that the regions with the different materials can be determined (segmented). See appendix A.3 on the lower left for an application example.

2.2. Fourier analysis

Fourier analysis [12] is a mathematical framework that has many applications in physics, e.g. linear differential equations, electrodynamics or quantum mechanics. It allows an easier treatment of phenomena where size scales in the analyzed quantity (signal) play an important role. The basic approach is that a continuous signal is decomposed into a basis of oscillating functions. In the 1-dimensional case, the Fourier transform $\mathcal{F}$ of a function $s(x)$ can be written as:

$$\mathbf{s}(u) = \mathcal{F}\{s\}(u) = \int_{\mathbb{I}} \mathrm{d}x\, s(x) \exp(-2\pi i x u) \tag{2.7}$$

where the complex exponential functions are the basis functions and $\mathbb{I}$ stands for the whole image space (similar to $\mathbb{R}$ or $\mathbb{N}$). The notation used here is that bold lowercase characters represent Fourier transformed, regular lowercase represent real space functions and Power spectra (see later) are written as regular uppercase characters. The variable u is called the spatial frequency if x is a spatial coordinate. This equation can easily be extended into higher dimensions by interpreting u and x as vectors and xu as a scalar product.

In imaging, Fourier analysis is used to analyze or modify (filter) specific structure sizes in an image. Thereby the higher spatial frequencies correspond to smaller structures in the image. A blurring filter (e.g. gaussian blur) reduces the amplitude of the higher spatial frequencies and results in a "smoother" image.

From the definition of the Fourier transform, many computation rules follow, of which the following are used (implicitly) later in this work [12]:

$$\mathcal{F}\{af\} = a\mathcal{F}\{f\} \tag{2.8}$$

$$\mathcal{F}\{f+g\} = \mathcal{F}\{f\} + \mathcal{F}\{g\} \tag{2.9}$$

$$\mathcal{F}\{f(x+\chi)\} = \mathcal{F}\{f(x)\}\exp(-2\pi i \chi u)$$

$$\Leftrightarrow |\mathcal{F}\{f(x+\chi)\}|^2 = |\mathcal{F}\{f(x)\}|^2 \tag{2.10}$$

2.2.1. Modulation transfer

The convolution $*$ of a signal with a point spread function (PSF) h corresponds to a multiplication of the Fourier transformed signal with its Fourier transformed $\mathbf{h}$ (called optical transfer function, OTF):

$$s_h(x) = (s * h)(x) = \int \mathrm{d}\chi s(x) h(\chi - x) \tag{2.11}$$

$$\Leftrightarrow \mathbf{s}_h(u) = \mathbf{s}(u)\mathbf{h}(u) \tag{2.12}$$

In a physical imaging setup, the measurement setup causes a blurring of the measured signal due to different effects (e.g. size of the light source, diffraction limit). If the mapping of a delta-peak like intensity distribution to the measured intensity is interpreted as a point spread function, then the absolute of $\mathbf{h}$ is called the modulation transfer function (MTF). In the rest of this work, $\mathbf{h}$ will be called MTF, as for most physical systems in x-ray imaging, the OTF is identical to the MTF (except for phase shifts, which are irrelevant).

The MTF is an important factor in the formation of x-ray imaging quality. It describes with what amplitude a signal structure of a specific size is transferred through the measurement apparatus. Lower amplitudes are more difficult to detect, thus a lower MTF towards higher frequencies means that small image structure is more difficult to detect. The MTF starts at $\mathrm{MTF}(u = 0) = 1$ and decreases towards higher frequencies. A faster decrease is a worse MTF.

PSF $\Leftrightarrow$	MTF	names
$\exp\left(\frac{-x^2}{2\sigma^2}\right)$	$\exp\left(-2\pi^2u^2\sigma^2\right)$	Gaussian
$\frac{1}{1+\mu^2x^2}$	$\exp\left(-2\pi\lvert u\rvert\mu\right)$	Lorentz/Exp
$\mathrm{rect}(\frac{x}{d})$	$\mathrm{sinc}(du)$	
$\mathrm{tri}(\frac{x}{d})$	$\mathrm{sinc}(du)^2$	
$\delta(x)$	1	delta distr./const.

Table 2.1.: Fourier transform pairs for some commonly used functions. $\mathrm{rect}(x)$ is the rectangular function, which is 1 in $[-\frac{1}{2},\frac{1}{2}]$ and 0 else and the triangle function $\mathrm{tri} = \max(1-|x|,0) = (\mathrm{rect} * \mathrm{rect})(x)$.

The validity of the convolution as a model for the intensity mapping implies that we assume the measurement apparatus as a linear translationally invariant system (LTI). Thereby linear means that multiplication with a factor h models the response of the input intensity to the output intensity, and translationally invariant means that h is constant over the whole signal. In many cases, h is also radially symmetric, in which case $\mathbf{h}$ can be radially averaged before the evaluation.

Fourier transform pairs are two functions that are the Fourier transformed of each other. Some PSF/MTF pairs commonly used in imaging are given in table 2.1. The first two are commonly used as simplified approximations for physical blurring, and the product of both is called the Voigt MTF. The triangle function/sinc^2 corresponds to the blurring caused by a linear interpolation, the rectangular function to the effect an area pixel sampling has. The $\delta \Leftrightarrow 1$ pair is important for modeling white noise.

Measurements of the MTF are done e.g. with a slanted edge/slit test phantom, see e.g. [13]. The commonly used line patterns (or similar test phantoms) can be used to roughly estimate the modulation transfer but they do not replace an actual measurement. If a poylchromatic x-ray imaging device has a energy-dependent MTF, the MTF measurement needs to consider the possibility that the MTF depends on the sample. The edge test phantom may therefore have a different MTF than the actual sample (and the MTF may vary within the sample). See section 3.4.4 for details.

2.2.2. Discrete pixel sampling

Measuring a spatially continuous signal in a physical setup implies that the data is discretely sampled spatially.[1] To do so, one defines either areas or points in space (pixels) for which one gray value represents the measurement result. While in practice, one always works with pixelized data, it is important to keep in mind that the physics happens on continuous data spaces:

> Imaging physics works on continuous image spaces and the discrete pixel space is applied only after the detection.

Only in the very last step of the measurement this continuous function is sampled to generate a discrete image. Usually, this sampling is (and should be) done in a way that does not decrease image quality. The sampling distance of an image therefore is not an indicator of the spatial resolution which is achieved by a setup, this is instead given by the modulation transfer discussed above. Of course, the spatial resolution cannot be better than the sampling distance/pixel size. Note that even for noise, the physics happens in continuous space and is later made discrete. Simulations can be done on a smaller pixel size (oversampling) and then averaged to the actual pixel size to approximate this.

Real physical detectors collect all detection events in a specific detector area into one pixel gray value $d(x)$. Consequently, the shape of this area acts as a PSF (rect() function in table 2.1), which has the effect of a smoothing of the image. Another consequence is that image features that are smaller than one pixel reliably produce a signal in the corresponding pixel. (This is not the case for point-wise sampling.) The strength of this signal is scaled by the fraction of the feature area to the pixel area. Therefore, a too coarse sampling does not make it impossible to detect small objects, but the spatial precision is limited by the pixel size.

Features of higher subdimensions (line in 2D/3D, plane in 3D) are easier to detect than point-shaped features because they have a higher area. They also can span multiple pixels, so correlating multiple pixels makes the detection of such objects even easier.

[1] Continuous image data would require an infinite amount of information storage. This is why measured image data is always composed of discrete values both spatially and also for the gray values. For the same reason, real number representations on computers (float) also have limited precision.

2.2.3. Power spectra

An image power spectrum $D(u)$ is the square of the absolute value of the Fourier transformed of the image d (data):

$$D(u) = \left| \frac{1}{A} \mathcal{F}\{d\}(u) \right|^2 \tag{2.13}$$

A is the area of the whole image, given in physical lengths. Typically, A can be computed as number of pixels/voxels in the image times a^ν. a is the side length of the digital image element (pixel or voxel) and ν is the number of dimensions of the image (here: 2 or 3). The factor containing these two quantities is a normalization and ensures that the continuous signal is represented correctly. It is only applicable if area sampling is used and corrects the effect of the gray value (intensity) being proportional to the sampling area. When computing SNR spectra, this factor cancels out because it appears both in the nominator and the denominator; the factor $\frac{1}{A}$ is therefore later often omitted.

Power spectra are especially useful if d is a (partially) random quantity. Physical equations of power spectra in this work describe physical properties of the image and underlying stochastic processes, not measured values of a specific image. Determining $D(u)$ for a specific realization of $d(x)$ therefore has corresponding measurement errors.

The autocorrelation function describes the correlation of a signal with itself at a different point in space. It is defined as:

$$\Psi\{dd\}(x) = \int \mathrm{d}\chi d^*(\chi) d(\chi + x) = d^*(-x) * d(x) \tag{2.14}$$

In the last step, the autocorrelation function is rewritten as a convolution, from which the following relationship can be derived:

$$\mathcal{F}\{\Psi_{dd}\}(u) = \left| \mathcal{F}\{d\}(u) \right|^2 = D(u) \tag{2.15}$$

The fact that the Fourier transformed of the autocorrelation function is identical with the power spectrum is called the Wiener-Chinchin-Theorem. The main use of investigating power spectra lies in the fact that one can make use of this relation in the following way:

For uncorrelated images n_1 and n_2 and

$$n = n_1 + n_2 \tag{2.16}$$

we can write:

$$\begin{aligned} \Psi\{nn\}(x) &= \Psi\{(n_1 + n_2)(n_1 + n_2)\}(x) && (2.17)\\ &= \Psi\{n_1 n_1 + n_2 n_2 + 2 n_1 n_2\}(x) && (2.18)\\ &= \Psi\{n_1 n_1\}(x) + \Psi\{n_2 n_2\}(x) \\ &\quad + 2\Psi\{n_1 n_2\}(x) && (2.19) \end{aligned}$$

As the images n_1 and n_2 are uncorrelated, the mixed term is zero:

$$\begin{aligned} &\Psi\{n_1 n_2\}(x) = 0 && (2.20)\\ \Rightarrow\ &\Psi\{nn\}(x) = \Psi\{n_1 n_1\}(x) + \Psi\{n_2 n_2\}(x) && (2.21) \end{aligned}$$

Using eq. (2.15), we can write:

$$N = N_1 + N_2 \tag{2.22}$$

which can easily be extended to

$$N = \textstyle\sum_{k=1}^{K} N_k \quad \text{if} \quad \Psi_{n_k n_j} = 0 \text{ for } k \neq j \tag{2.23}$$

This relation is the main reason why power spectra are useful in imaging and why they are used in this work instead of e.g. amplitude spectra. Due to the fact that noise is always uncorrelated with noise (this is part of the definition of what is noise), and that signal and noise are also always uncorrelated, power spectra allow the use of the very convenient simplification above (e.g. for superposition).

For signal sums on the other hand, the individual contributions are fully correlated and we get:

$$\begin{aligned} S &= \left| \textstyle\sum_{k=1}^{K} \mathcal{F}\{s\}(u) \right|^2 = K^2 S_1 && (2.24)\\ &\text{if } \Psi_{n_k n_j} = \Psi_{n_k n_k} \text{ for arbitrary } k, j && (2.25) \end{aligned}$$

A power spectrum which is constant with respect to the spatial frequency

$$D(u) = \mathrm{const}(u) \tag{2.26}$$

is called a "white" power spectrum. This stems from the fact that for (idealized) white light, all frequencies have equal amplitude and power. A noise power spectrum which is white is called white noise. It has the property that noise at one pixel is independent of noise at another pixel, which can be derived from eq. (2.15):

$$\Psi_{dd}(x) = \mathcal{F}^{-1}\{D(u)\} \propto \delta(x) \tag{2.27}$$

This is represented by a correlation function $\delta(x)$, which is zero for different pixels (or points in space).

Spatial frequency axis

The spatial frequency u has units 1/length. To simplify the understanding of what the value of u represents, one can compute the corresponding structure size l:

$$l = \frac{1}{2u} \tag{2.28}$$

In a discretely sampled image, the maximal spatial frequency is given by the Nyquist frequency u_{ny} for a pixel size l_{PS}:

$$u_{ny} = \frac{1}{2l_{PS}} \tag{2.29}$$

In the x-axes of power spectra or SNR spectra plots (e.g. fig. 3.10), the value of l is used to label the x-axis. In combination with the value for the Nyquist frequency, this means that the spatial frequency axis goes from a structure size of ∞ to l_{PS} and that the numbers on the axis directly correspond to the actual structure size. This scale is *not* one of wave periodicity (= line pair distance). I consider this notation to be much easier to understand than units based on periodicity.

A structure size of l corresponds to a periodicity of $2l$, this means that the smallest structure possible is a feature with a size of a single pixel or a periodic pattern with a period of two pixels (consecutive dark/bright). Because image features are typically not similar in shape to waves, the use of the structure size is more natural. The axis notation chosen in this work also avoids this complication.

In higher dimensions, the highest absolute spatial frequency possible is not the Nyqist frequency. Instead, the corners of the K-dimensional u-rectangle correspond to the highest spatial frequency possible:

$$|u|_{max} = \sqrt{u_{ny,\,x}^2 + u_{ny,\,y}^2 + ...} = u_{ny}\sqrt{K} \tag{2.30}$$

Where the last simplification is only valid for pixels with equal side lengths. A practical consequence of this fact is that if a radially symmetric analytic Fourier filter is applied to an image and this filter strongly amplifies higher frequencies, checkerboard patterns appear. This commonly happens with wrongly parameterized deconvolution filters.

In this work, spatial frequency plots are usually radially averaged. The radially averaged coordinate is called u. It is plotted over the range of $[0,\ u_{\mathrm{ny}}]$, excluding the corners of the spatial frequency rectangle. Radial averaging is appropriate if e.g. the power spectrum of an image is isotropic, meaning that its properties are independent of angular orientation. Even in cases where some properties are highly anisotropic (e.g. noise in a CT 3D image, see eq. (2.56)), the radially averaged representation is still useful if the relevant properties (e.g. MTF) are isotropic.

2.3. Probability theory

Random noise plays an important role for the analysis of image quality in x-ray imaging. The properties and consequences of this random noise are described by probability theory. In fact, noise is equivalent to the random measurement error (not systematical errors). Therefore, probability theory is an important part of any discussion of image quality. I will consider the bayesian interpretation of the theory [14], in which probability is understood to describe a state of knowledge or uncertainty. As an extension of true/false logic [15], a probability value p between 0 (false) and 1 (true) describes a degree of plausibility that a statement is true based on specific knowledge. In bayesian probability theory, there is no concept of objective probabilities, they are instead by definition dependent on the knowledge of the observer.

The basic mathematical rules of probability theory can be looked up in any standard text book (e.g. [14, 15]). Of specific interest here is the case of a measurement error: A high image quality corresponds to a low measurement error.

2.3.1. Measurement error

If an observer measures a value d (data), the problem of the measurement error can be stated as such: What is the probability distribution for the true value s (signal)? s can be seen as the quantity which the measurement result d aims to determine. This uncertainty about the true value given the knowledge of the measurement(s) is the measurement error. It can be written using Bayes' law as:

$$p(s|d) = \frac{p(d|s)p(s)}{p(d)} \tag{2.31}$$

which is derived from the more fundamental law:

$$p(s,d) = p(d|s)p(s) = p(s|d)p(d) \tag{2.32}$$

Here, $p(s,d)$ is the probability that both s and d are true and $p(s|d)$ is the probability of s given that d is true (was observed). $p(d)$ is a normalization constant (independent of s) and $p(s)$ is called the prior probability, it is used to describe the state of knowledge

before the current measurement. If we assume no prior knowledge, then $p(s) = \text{const.}$[2]

This equation implies that the probability for a certain true value s if we know a measurement d is determined by the probability that the measurement d takes a certain value given the true value s. The latter is simply given by the measurement process, while the former is of interest. This requires a flexibility of the interpretation of what probability means: Independent from what the observer knows, s has a specific value. The observer cannot know this value with absolute certainty, but the knowledge of the observer can be stated with $p(s|d)$. Interpreting $p(s|d)$ as a frequency makes no sense, because s has exactly one value from an objective point of view.

The Bayesian interpretation of probability theory thus can be used to formulate observer uncertainty about quantities which are not random. This comprehension is important to understand both the SNR spectra model and the SNR measurement scheme presented later.

2.3.2. Signal, noise and error propagation

Another important tool is the linear additive noise model [16]. With s and d as defined above and the noise n, one can always define:

$$d = s + n \tag{2.33}$$

which can be seen as the defining equation for n. This is done to separate the random and deterministic parts of the measured value conceptually: s is purely deterministic and n is purely random. It also gives the definition of noise as the difference between signal (true value) and data (measured value). This equation does not imply that the properties of signal and noise are independent—e.g. Poisson noise is an example where the noise properties depend on the signal.

Error propagation is important for measurements where there is more than one source of uncertainty or if the quantity of interest is derived from the measured value by applying some mathematical transformation. We then need to insert the knowledge of how the different uncertainty sources influence the result into a computation with probabilities. Sources of randomness are here given by different physical processes, for example b and c (e.g. x-ray intensity + dark current). Then the measured value a is given by:

$$a = b + c \Leftrightarrow p(a|b,c) = \delta(a - b - c) \tag{2.34}$$

For more complex dependencies, the function can be linearized with respect to all variables. Alternatively, the probability distributions can be propagated through the mathematical transformation. The latter is necessary in some special cases, e.g. around the extrema of a function.

At this point, an ambiguity in the commonly used notation of probabilities needs to be corrected [14]. Strictly speaking, the functions $p(b)$ and $p(c)$ must not both use the function name p, but should instead use different function names, e.g. $p_b(b)$ and $p_c(c)$.[3] This becomes necessary if we do a variable transformation for b or c, but in other contexts, the ambiguous notation can also lead to subtle errors if used without care.

If $p_b(b)$ and $p_c(c)$ are known, $p_a(a)$ can be computed via:

$$\begin{aligned} p_a(a) &= \int \mathrm{d}b\, p_{a,b}(a,b) = \int \mathrm{d}b \int \mathrm{d}c\, p_{a,b,c}(a,b,c) \\ &= \int \mathrm{d}b \int \mathrm{d}c\, p_a(a|b,c) p_{b,c}(b,c) \\ &= \int \mathrm{d}b \int \mathrm{d}c\, \delta(a-b-c) p_b(b) p_c(c) \\ &= \int \mathrm{d}b\, p_b(b) p_c(a-b) \end{aligned} \tag{2.35}$$

Here, we use the computational trick of extending a marginalization twice and then inserting eq. (2.34). The last form is identical to a convolution of the probability distributions describing the measurement errors of the individual quantities. The error distribution is therefore given by the convolution of the individual error distributions. We can therefore use the multiplication in Fourier space, eq. (2.12), to compute the measurement error of a sum of contributing quantities. In the case of Gaussian error distributions, one can easily derive the additivity of the variances if p_b and p_c are uncorrelated:

$$\mathrm{var}(a) = \mathrm{var}(b) + \mathrm{var}(c) \tag{2.36}$$

Note that the Fourier transformed of a probability distribution is also called "characteristic function"

[2] Defining an actual neutral prior is more complicated than implied here, e.g. a prior that has a constant probability for a quantity whose value range spans several orders of magnitude is the inverse of the value. A constant prior would bias the probability towards higher values. See [14].

[3] There is no strict differentiation between variables and functions—$p(b)$ and p describe the same quantity, only the dependency is not stated explicitly in the latter notation. Relying on the assumption that the brackets contain all dependencies can easily lead to errors, as the actual dependencies are given by the problem and not the representation chosen.

and can be used to simplify various computations, specifically in stochastic processes [17].

2.3.3. Wiener filter and deconvolution

In general all image restoration filters like the Wiener filter [18, 19, 16] are limited by the SNR (or information content) of the measurement. These filters attempt to optimally reconstruct the signal from the data. Thereby, information which is not in the measurement can not be restored by a filter—except if this filter *adds* the information. In the latter case, it is not (only) a reconstruction filter. The Wiener filter makes this limitation clearly understandable and is important to understand from two points of view:

- To understand the limitations of any kind of image improvement or reconstruction filter whose aim it is to improve image quality.
- To understand how image quality works and how SNR and modulation transfer interact.

The Wiener filter is an important theoretical context in which SNR spectra are commonly used and understanding the Wiener filter makes it easier to understand why SNR spectra are a good model for image quality.

For the derivation of the Wiener filter with deconvolution, I use a modified form of the data model, eq. (2.33), that includes the convolution with the MTF $\mathbf{h}$. For simplicity, only Fourier coordinates (e.g. $\mathbf{d} = \mathcal{F}\{d\}$) are used—similarly to how some problems are easier in e.g. a spherical coordinate system. This implies that we assume a LTI system. The data model of a Wiener filter states how the measured data $\mathbf{d}$ is produced from the signal $\mathbf{s}$, this represents the measurement process:

$$\mathbf{d} = \mathbf{h}\mathbf{s} + \mathbf{n} \tag{2.37}$$

In general, the optimally reconstructed signal $\mathbf{r}_d$ is defined such that the statistical mean of the deviation between $\mathbf{r}_d$ and the actual signal $\mathbf{s}$ is minimal:

$$\mathbf{r}_d = \operatorname{argmin}\{\operatorname{diff}(\mathbf{r}_d - \mathbf{s})\} \tag{2.38}$$

where the diff function can e.g. be a linear or quadratic difference. The probability of the value $\mathbf{s}$ if data $\mathbf{d}$ was measured can be written with Bayes' theorem as:

$$p(\mathbf{s}|\mathbf{d}) = \frac{p(\mathbf{d}|\mathbf{s})p(\mathbf{s})}{p(\mathbf{d})} \propto p(\mathbf{d}|\mathbf{s})p(\mathbf{s})$$

If we minimize the (global) average of the square of the difference,

$$\frac{\mathrm{d}}{\mathrm{d}\mathbf{r}_d} \int \mathrm{d}\mathbf{s}\, p(\mathbf{s}|\mathbf{d})\, (\mathbf{s} - \mathbf{r}_d)^2 \stackrel{!}{=} 0 \tag{2.39}$$

$$\Leftrightarrow -\int \mathrm{d}\mathbf{s}\, p(\mathbf{s}|\mathbf{d}) 2\, (\mathbf{s} - \mathbf{r}_d) \stackrel{!}{=} 0 \tag{2.40}$$

$$\Leftrightarrow \int \mathrm{d}\mathbf{s}\, p(\mathbf{s}|\mathbf{d})\mathbf{s} \stackrel{!}{=} \mathbf{r}_d \int \mathrm{d}\mathbf{s}\, p(\mathbf{s}|\mathbf{d}) \tag{2.41}$$

$$\Rightarrow \quad \mathbf{r}_d = \int \mathrm{d}\mathbf{s}\, p(\mathbf{s}|\mathbf{d})\mathbf{s} \tag{2.42}$$

If use the following approximations: (1) $p(\mathbf{d}|\mathbf{s})$ and $p(\mathbf{s})$ are Gaussian distributions (2) the power spectrum matrix is the Fourier transform of the auotcorrelation matrix (Wiener–Khinchin theorem) and (3) translational invariance. Then power spectra matrices S and N are diagonal and we get:

$$p(\mathbf{s}) \propto \exp\left(-2\pi^2\, \mathbf{s}^2 S^{-1}\right)$$

$$p(\mathbf{n}) \propto \exp\left(-2\pi^2\, \mathbf{n}^2 N^{-1}\right)$$

$$p(\mathbf{d}|\mathbf{s}) \propto \int \mathrm{d}\mathbf{n}\, p(\mathbf{d}|\mathbf{s}\mathbf{n})p(\mathbf{n}) \tag{2.43}$$

$$= \int \mathrm{d}\mathbf{n}\, \delta(\mathbf{d} - \mathbf{h}\mathbf{s} - \mathbf{n})p(\mathbf{n}) \tag{2.44}$$

$$= \exp\left(-2\pi^2\, (\mathbf{d} - \mathbf{s}\mathbf{h})^2 N^{-1}\right)$$

where all probability distributions are normalized to one but the normalization factors are omitted.

The optimal signal reconstruction $\mathbf{r}_d$ is given by

$$\mathbf{r}_d = \int \mathrm{d}\mathbf{s}\, \mathbf{s} p(\mathbf{s}|\mathbf{d}) \propto \int \mathrm{d}\mathbf{s}\, \mathbf{s}\, p(\mathbf{d}|\mathbf{s})p(\mathbf{s})$$

$$p(\mathbf{d}|\mathbf{s})p(\mathbf{s}) = \tag{2.45}$$

$$= \exp\left(-2\pi^2\left[(\mathbf{d}^2 - 2\mathbf{d}\mathbf{s}\mathbf{h} + \mathbf{s}^2\mathbf{h}^2)N^{-1} + \mathbf{s}^2 S^{-1}\right]\right)$$

$$\propto \exp\left(-2\pi^2\left[(\mathbf{h}^2 N^{-1} + S^{-1})\mathbf{s}^2 - 2\mathbf{d}HN^{-1}\mathbf{s}\right]\right)$$

If we compare this to an arbitrary Gaussian distribution $\mathcal{G}(s|\mathbf{r}_d P)$ for $\mathbf{s}$ with mean $\mathbf{r}_d$ and power spectrum P:

$$\mathcal{G}(s|\mathbf{r}_d P) \propto \exp\left(-2\pi^2\, (\mathbf{s} - \mathbf{r}_d)^2 P^{-1}\right)$$

$$\propto \exp\left(-2\pi^2\left[(P^{-1}\mathbf{s}^2 - 2\mathbf{r}_d P^{-1}\mathbf{s}\right]\right) \tag{2.46}$$

Then we can identify by comparison:

$$P^{-1} = \mathbf{h}^2 N^{-1} + S^{-1}$$

$$\mathbf{r}_d = \frac{\mathbf{d}HN^{-1}}{\mathbf{h}^2 N^{-1} + S^{-1}} = \frac{1}{1 + NS^{-1}\mathbf{h}^{-2}}\mathbf{h}^{-1}\mathbf{d} \tag{2.47}$$

We can define:

$$\mathrm{SNR}^{-1} = NS^{-1}\mathbf{h}^{-2} \tag{2.48}$$

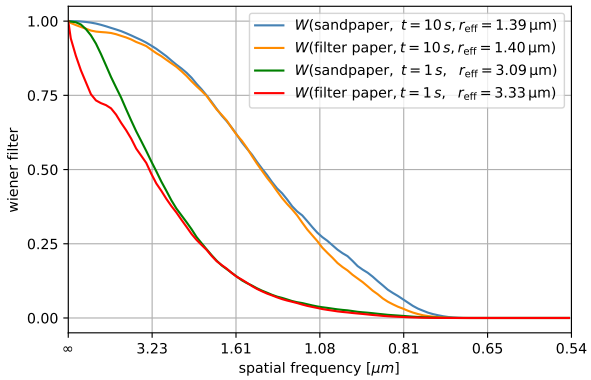

Figure 2.2.: Examples for Wiener filter curves from measured $SNR(u)$, see section 4.2.1 on page 61 for a description of the setup and methods. The effective resolution r_{eff} is here defined as the structure size equivalent to $W(u) = 0.5$ or $SNR(u) = 1$. t is the exposure time for the image.

Note that the rest of this work uses eq. (2.33) as the data model and a different definition of the SNR applies. The final result for the Wiener Deconvolution, is given by the optimal signal reconstruction from the data. This is a multiplication in Fourier space with the filter $W_H(u)$:

$$W_H(u) = \frac{1}{1 + \text{SNR}(u)^{-1}} \mathbf{h}(u)^{-1} \tag{2.49}$$

The noise suppression part of this filter is the Wiener Filter $W(u)$, where we exclude the deconvolution step:

$$W(u) = \frac{1}{1 + \text{SNR}(u)^{-1}} \tag{2.50}$$

In fig. 2.2, examples for Wiener filter curves computed from measured SNR spectra are shown.

In principle, the Wiener filter can be seen to already include the deconvolution due to how the data model is defined. The term Wiener deconvolution is thus mainly used to emphasize that the effect of the filter is not just noise suppression, but also sharpening (deconvolution). Note that applying a Wiener deconvolution does not change the $\text{SNR}(u)$ (like any other Fourier filter), but a filtered image my appear less noisy or sharper.

The Wiener filter only uses very weak assumptions about the data. This is an advantage in that applying a Wiener filter does not add strong assumptions during the signal reconstruction, which could lead to artificial image features produced by the filter. Such artifacts are a problem for noise suppression/deconvolution filters in general, because too aggressive image improvement can add image information which is actually not in the signal. On the other hand, a filter using weak assumptions is strongly limited in the amount of image improvement it can do. If the assumptions of a strong filter are true, the possible image improvements are great. Such a example is if the image only contains two gray values (two material CT image).

By combining eq. (2.37) and eq. (2.49), we can see that the effective modulation transfer for a noise suppressed image is given by eq. (2.50). This equation can be seen as defining an MTF which includes modulation transfer and noise effects. Both effects are unified in this equation and one could argue that image quality is wholly determined by $W(u)$ and therefore by $SNR(u)$.

The Wiener filter can also be used to reconstruct noise:

$$W_N(u) = \frac{1}{1 + SNR(u)} \tag{2.51}$$

$$\Rightarrow W(u) + W_N(u) = 1 \tag{2.52}$$

So that the sum of signal reconstruction and noise reconstruction is the data. Note that the Wiener filter is an optimization on the whole image. An image which has regions with very different properties (e.g. the amount of sample structure) should be evaluated for every region separately.

2.4. Computed tomography

2.4.1. Measurement technique

This chapter gives a very short introduction into the measurement technique computed tomography (CT), for details refer to [20] or any other CT imaging textbook.

The principle of the CT is based on a mathematical principle first discovered by Radon. Its states that the gray values in a plane section of a volume image can be reconstructed from a set of line integrals, where all directions passing through the plane are included in the set. The line integrals are given by the intensity in a projection image according to eq. (2.2). Note that all line integrals through the sample for the whole width of the sample need to be know from every direction. This condition is violated e.g. if beam and plane are not perpendicular (cone beam artifacts) or if the sample is larger than the field of view (local tomography).

In practice, a CT measurement consists of acquiring many projection images from different view directions. The curve that the view directions describe in space is the shape of the scan path, the simplest shape is a circle. This circle is acquired either by rotating the sample in a stationary x-ray beam or by rotating the beam around the sample. The former is a typical laboratory CT setup while the latter is typical for medical CT.

The number of views K_{CT} required is determined by the desired angular resolution. A rough estimate is given by the achievable spatial resolution (limited by setup MTF) r in the CT image and the width of the field of view d_{FOV}, also in the CT volume. The value is given by the angle spun by the spatial resolution distance at the outer edge of the FOV (for a circular scan path):

$$K_{\mathrm{CT}} \overset{!}{>} \frac{\pi d_{\mathrm{FOV}}}{r} \tag{2.53}$$

In practice, the spatial resolution is often worse by at least at factor of π than the voxel size, so that the number of projections is chosen to be equal or smaller than the number of horizontal detector pixels.[4] Within the context of this work, the achievable spatial resolution should be interpreted as derived from the Wiener filter and the SNR spectrum (see previous section).

To achieve a specific image quality, the number of detected x-ray photons which have interacted with a specific sample volume is decisive. This number is proportional to the product of K_{CT} with the measurement time t per projections, it is the measurement time of the whole CT. If the image quality should be kept constant, e.g. reducing K_{CT} therefore implies increasing t proportionally.

A CT volume image can be reconstructed from a set of projections. Different reconstruction algorithms exist, the commonly used deterministic algorithm for CT reconstruction is the filtered backprojection (FBP). For cone geometries, the Feldkamp-Davis-Kress (FDK) algorithm [21] can be used, which is based on the FBP.

The noise of a CT reconstructed image is transformed by the following MTF through a FBP reconstruction algorithm [22]:

$$\mathbf{h}_{\mathrm{CT\,noise}}(u_x, u_y, u_z) = \tag{2.54}$$

$$\sqrt[4]{u_x^2 + u_y^2}\ \mathrm{sinc}(u_x)^2 \mathrm{sinc}(u_y)^2 \mathrm{sinc}(u_z)^2 \tag{2.55}$$

[4] Considering eq. (2.30), the theoretically required K_{CT} is higher by a factor of $\sqrt{2}$ than indicated by eq. (2.53) (applies to the diagonal views).

The highpass filter part $\sqrt{u}$ results from a combination of the ramp filter and the density of the projection points in Fourier space. The blur part $\mathrm{sinc}(u_x)^2$ results from the linear interpolation which is part of the backprojection.

The transfer functions for radially averaged volume power spectra can be approximated in the following form:

$$\mathbf{h}^2_{\mathrm{CT\,noise}}(u) \approx u\,\mathrm{sinc}(u)^{3.4} \tag{2.56}$$

$$\mathbf{h}^2_{\mathrm{CT\,signal}}(u) \approx \mathrm{sinc}(u)^{3.4} \tag{2.57}$$

While the radial averaging of the x-y-ramp simply results in a radial ramp (with a different slope), it does affect the sinc part. The values were found by performing a CT FBP reconstruction (using pyXIT) on noise images and fitting a model to the resulting power spectra. If arbitrary blur filters are part of the reconstruction (e.g. Shepp-Logan filter), these would also appear here.

Signal transfer does not include the ramp, but does include the interpolation blur. The ramp filter inverts the (statistical) blurring caused by projecting a 3D image onto a 2D projection The signal power spectrum of the original object is restored by a CT reconstruction image—except for algorithm-specific parts like an interpolation used.

What follows are some topics which stand isolated from the rest of this work. They are original ideas by the author of this work and are of interest within the context of CT.

2.4.2. Optimal number of reference images

A CT measurement consists of a series of projections that all use the same reference image, see eq. (2.1). This reference image is usually computed as an average from a number K_{ref} reference images to reduce the effect of noise in the reference image. The number K_{ref} is usually chosen by a rough human estimate, as there appear to be no known formulas for computing an estimate.

Under some specific assumptions, it is possible to derive the optimal K_{ref} from a standpoint of reducing noise in the CT. Noise in the reference image actually does not produce (normal) noise in the CT image due to the fact that this noise is identical for all projections; it instead produces random ring artifacts. A simple solution can be derived if we ignore this aspect and

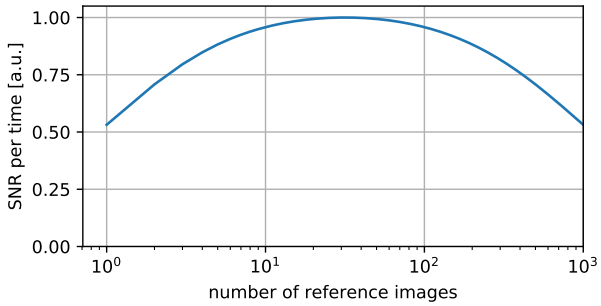

Figure 2.3.: SNR per measurement time curve used to determine an estimate for the optimal number of reference images with $K_{CT} = 2000$, $T = 0.5$ and $K_{ref,\,opt} = 32$. The square root in eq. (2.62) means that the maximum in a x-log plot is in the middle between 1 and $TK_{CT} = 1000$. Here, K_{ref} between 10 and 100 are a good choice.

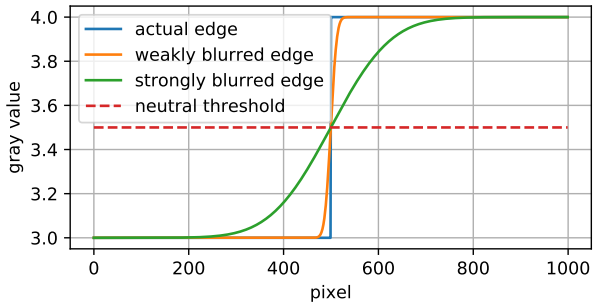

Figure 2.4.: Schematic plot showing a neutral threshold (= 3.5) for the actual edge (theoretical truth) and two blurred edges (realistic data). The neutral threshold applies the same segmentation independent from the amount of blur (border at x = 500 in this example). In higher dimensions, blur leads to a loss of detail in the segmented image.

choose K_{ref} such that the noise in the single projection is minimized.

The noise in a single referenced projection is given by error propagation on a linearization of eq. (2.1). With N_{image} the noise[5] of the projection, N_{ref} the noise of the ref image, T being the sample transparency and I, I_{ref} being the corresponding intensities ($I = TI_{ref}$) we get for the noise N of a referenced image:

$$N \propto \frac{N_{image}}{I^2} + \frac{N_{ref}}{I_{ref}^2 K_{ref}} \tag{2.58}$$

$$\left(\text{use } I = TI_{ref} \text{ and } N_{image} = TN_{ref}\right)$$

$$N \propto \frac{1}{T} + \frac{1}{K_{ref}} \tag{2.59}$$

If K_{CT} is the number of projections in the CT, then the measurement time t of the whole CT is proportional to $(K_{CT} + K_{ref})$. The optimal number of reference images is then given by the maximum of SNR per measurement time:

$$\frac{SNR}{t} \propto \frac{1}{Nt} \propto \frac{1}{(\frac{1}{T} + \frac{1}{K_{ref}})(K_{CT} + K_{ref})} \tag{2.60}$$

$$K_{ref,\,opt}(K_{CT}) = \text{argmax}\left(\frac{SNR}{t}\right) \tag{2.61}$$

$$= \sqrt{TK_{CT}} \tag{2.62}$$

An example for the SNR/t curve is shown in fig. 2.3. For a CT with 2000 projections and $T = 0.5$, we would thus get a value of $K_{ref,\,opt} = 32$. Typical values currently used are between 50 and 100.

[5] "Noise" could here either mean the variance or the noise power spectrum.

2.4.3. Neutral image segmentation

Image segmentation is in general a processing step which divides an image into distinct classes of areas ("segments"). The most common case is a segmentation into different material areas. There exist different methods to derive an optimal threshold, see e.g. [23]. A simple approach to defining a neutral threshold d_t for segmenting two materials with gray values d_A and d_B is:

$$d_t = \frac{d_A + d_B}{2} \tag{2.63}$$

This is demonstrated in fig. 2.4. Using the neutral threshold has the effect that the volume fractions do not get a systematic bias from the threshold. Setting an arbitrary threshold which "looks good" to the user will usually result in such a bias. Independently, structural details below the spatial resolution of the measurement cannot be segmented and may produce a systematic error in the segmented areas and the volume fractions.

The neutral threshold is much easier to apply because the threshold no longer needs to be adjusted manually. This manual adjustment can also introduce systematic errors into an evaluation. Segmentation procedures using derivatives (e.g. maximum of the absolute of the first derivative) can also yield a neutral image segmentation.

Image segmentation usually benefits from a noise suppression, see section 2.3.3, because noise can lead to segmentation errors. A weak blurring on the other hand does not produce segmentation errors when the threshold was correctly chosen. If the parameters are

chosen correctly, then the noise suppression only blurs the image insofar as the image features removed by the filter would be artificial (noise) anyway.

2.4.4. CT reconstruction: pyXIT

pyXIT is the Python X-ray Imaging Tool and was developed by the author of this work as a side project. It is a software with a graphical user interface. Its main purpose is to do image processing in 2D and 3D, including CT reconstruction. pyXIT was designed to be scientific software with the corresponding features:

- Using Python as the programming language means that how the software works can be investigated and changed by any user. As an interpreted language, the development and execution environment are identical–if the software can be executed, it can also be changed. For scientific use this is important because how the software works is not a secret (and it should not be).
- All image processing algorithms are implemented as plugins and writing a plugin is easy. Existing Python code used in scientific investigations can easily be integrated.
- A fast preview of results enables to manually adjust parameters, which has three applications: (1) It allows the user to try out different parameters and learn how an algorithm works (2) Optimizing algorithm parameters, as automatic parameter determination may either not be available or unrealistic for experimental algorithms (3) During software development, the algorithm can be adjusted until the result is good.
- Many input and output file formats are supported.
- GPU computing via OpenCl is implemented to make specific algorithms fast (e.g. CT reconstruction, median filter). An own implementation of a Python interface to OpenCl is included, it is easy to use.

pyXIT was presented at the DIR-CT 2019 conference, the poster is shown in appendix A.3 on page 88. For further information, refer there.

2.4.5. Registration on noisy images

X-ray images are usually very noisy, and the image registration of noisy images then poses an additional problem for which a solution is presented here. From a theoretical standpoint, this solution is interesting because it is an application of probability theory to imaging.

Image registration is in general an algorithm which finds a coordinate transform between two images of the same object sampled in different coordinates. The simplest case are two images that are shifted with respect to each other, e.g. because the imaged sample moved between the acquisitions. Of practical importance are also magnification differences and rotations. In CT imaging, registration algorithms have many use cases.

The implementation is often done with a Fourier filter, but on current computing hardware (GPU), real space difference algorithms are sufficiently fast. This is due to the fact that these computing devices typically implement linear interpolation in hardware and have a very high memory bandwidth.[6] The latter is used in pyXIT because they have have several advantages:

- Arbitrary coordinate transforms can be implemented, not just shift.
- Pixel defects can be excluded by the algorithm.
- Higher precision can be achieved with a fast local search.
- Arbitrary functions for computing a difference can be used (e.g. linear or square difference).

The problem which appears for noisy images is that a (linear) interpolation between pixel values reduces the average noisiness for the interpolated value. A lower average noisiness has the effect that two images with different noise realizations match better. Therefore, a registration algorithm which uses interpolation to produce subpixel precision tends to find a result for which this noise reduction is maximal. As can be seen in fig. 2.5 the registration result will then always be shifted towards a N.5 result.

Usually, a registration algorithm doing a real space matching will read the first image on the original pixel sampling positions $r = (x, y)$ and the second shifted by a value $s = (s_x, s_y)$. In two dimensions, a registration algorithm for two shifted images d_1 and d_2 can be written as:

$$\Delta = \sum_r \left[d_1(r) - d_2(r+s)\right]^2 \tag{2.64}$$

$$s_{\text{shift}} = \operatorname{argmin}\left[\Delta(s)\right] \tag{2.65}$$

[6] Effective cached memory bandwidths of more than 1 TB/s can be observed on a high-end graphics card bought in 2016.

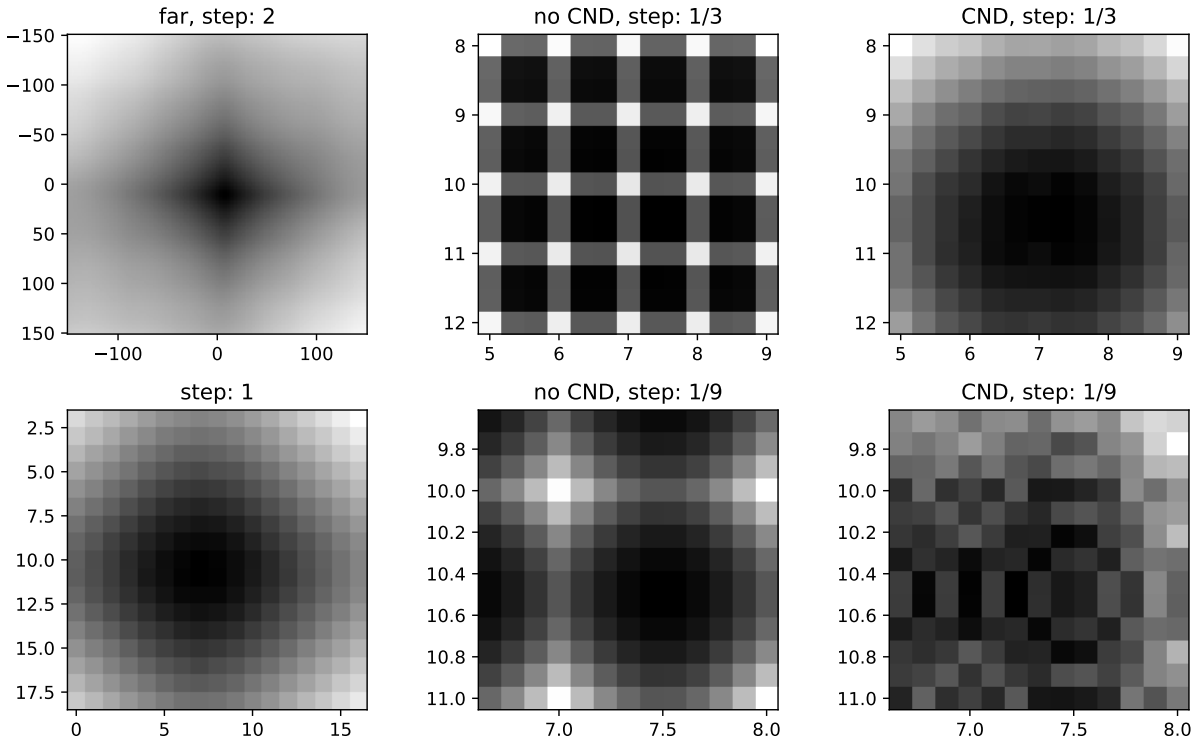

Figure 2.5.: Computed square difference examples for simulated images with a known shift of (7.07, 10.65). The images have different noise and an identical but shifted signal. Shift values are given by the axes labels and darker values correspond to a lower difference; the found shift of an algorithm is the darkest pixel. This implementation starts at a registration precision of 2 pixels and has three local searches around the prior result with a higher precision. The "no CND" images are from a standard real space registration algorithm and their minima are always falsely shifted towards .5 values, the CND algorithm registers close to the real shift. For the strong noise chosen, the difference images of the "no CND" algorithm are dominated by the noise difference pattern. Note that the CND algorithm shows a weaker artificial pattern for the smallest step, the origin of which is unknown.

To analyze the noise difference, it is sufficient to consider a single element of the sum above. As a further simplification, noise is assumed to be identical in the two images and the four neighboring pixels each. A two-dimensional linear interpolation applies the following weights to individual pixels:

$$w_{00} = \tilde{s}_x\tilde{s}_y \qquad w_{01} = \tilde{s}_x(1-\tilde{s}_y)$$
$$w_{10} = (1-\tilde{s}_x)\tilde{s}_y \qquad w_{11} = (1-\tilde{s}_x)(1-\tilde{s}_y) \tag{2.66}$$

where $\tilde{s}_x = s_x\%1$ is the integer rest of the shift. The scaling factor f for image difference noise (variance) which is produced by these weights is:

$$f^2 = \tilde{s}_x^2 s_y^2 + \tilde{s}_x^2(1-\tilde{s}_y)^2 \tag{2.67}$$
$$+ (1-\tilde{s}_x)^2 s_y^2 + (1-\tilde{s}_x)^2(1-\tilde{s}_y)^2 \tag{2.68}$$

This factor is minimal for $\tilde{s}_x = \tilde{s}_y = 0.5$.

The proposed algorithm instead additionally shifts the sampling positions of both images by a value $a = (a_x, a_y)$. This value is chosen in such a way that the average noise difference between two images with a different shift vector is constant, it is here called the the "constant noise difference" (CND) algorithm. The algorithm is then modified to:

$$\Delta = \sum\nolimits_r \left[d_1(r+a) - d_2(r+s+a)\right]^2 \tag{2.69}$$

If both images are shifted, the variance factors of both linear interpolations are added up. The sum then needs to be constant with respect to different s:

$$f_1^2(s,a) + f_2^2(s,a) = \text{const}(s) \tag{2.70}$$

This can be achieved by different choices of a, which are not uniquely determined by the requirements. The first choice done here is to set:

$$f_1^2 + f_2^2 = 1 \tag{2.71}$$

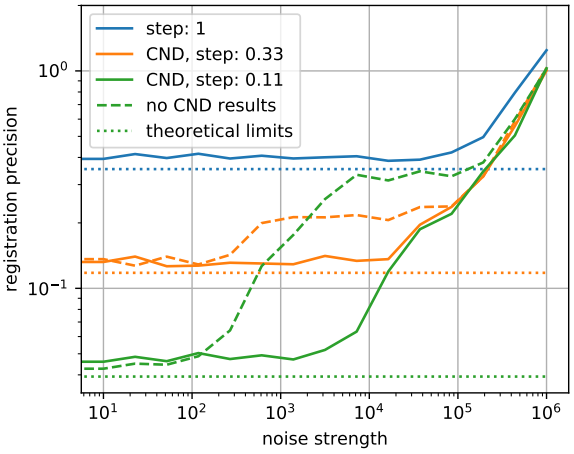

Figure 2.6.: Registration precision for the CND algorithm (solid lines) compared to the standard algorithm (dashed lines), computed for different noise strengths (scaling factor for the variance) and step sizes. Precision values are given by the euclidean distance between actual shift and true shift. To reduce noise in the curves, median values over a set of 300 registered images with random shift were taken each. The theoretical limits are given by step$\cdot 2^{-1.5}$ (step distance rounding error) and are plotted as dotted lines.

The second choice is a branching condition in the algorithm, because the additional shift needs only to be applied to one coordinate:

$$\begin{cases} a_x = 0 & \text{if } \min(s_x, 1-s_x) > \min(s_y, 1-s_y) \\ a_y = 0 & \text{else} \end{cases} \tag{2.72}$$

We can assume the first case without loss of generality and thus get:

$$\Delta = \sum_r \left[d_1 \begin{pmatrix} r_x \\ r_y + a_y \end{pmatrix} d_2 \begin{pmatrix} r_x + s_x \\ r_y + s_y + a_y \end{pmatrix} \right]^2 \tag{2.73}$$

If we define:

$$X = \tilde{s}_x^2 + (1-\tilde{s}_x)^2 \quad Y = \tilde{s}_y^2 + (1-\tilde{s}_y)^2 \tag{2.74}$$

$$b = 1 + |1 - 2\tilde{s}_y| X \tag{2.75}$$

$$\alpha = \frac{b - \sqrt{b - 2(1+X)XY}}{2(1+X)} \tag{2.76}$$

then

$$a_y = \begin{cases} \alpha & \text{if } \tilde{s}_y < 0.5 \\ 1-\alpha & \text{else} \end{cases} \tag{2.77}$$

solves the requirements from above. In the other case, the coordinate axes are simply switched. This algorithm is implemented in pyXIT. It was tested against an algorithm using a simple linear interpolation on one image and integer coordinates on the other image. The corresponding precision gain of the CND is shown in fig. 2.6. The noise strength used here is a scaling factor for the noise variance. Both algorithms perform equally good for low noise images and the CND algorithm performs much better for intermediate noise strengths. For very strong noise, subpixel precision is impossible, so both algorithms again perform similar. The CND algorithm loses precision at a noise strength which is a factor of 30 higher than the standard algorithm.

Note that for the standard algorithm, the choice of the step size influences the precision—0.33 is good while 0.5 would be bad. This is why a step 0.11 can be worse than 0.33, the first selects between 0.44 and 0.55 while the second between 0.33 and 0.67. The latter is then on average closer to the actual value. Interpolating algorithms perform better towards high noise ($> 10^5$ in the example), this may be caused by the fact that the interpolation has a noise suppressing effect.

The performance impact of computing the additional shift is the only computation step which could be seen as a disadvantage of the algorithm. To test if this computation decreases the speed of the algorithm, run times of the CND algorithm and a variant with addition shift set to zero were compared. There is no measurable difference in the speed between the two algorithms. This is probably because the computation can be done while the compute units wait on the memory access, and the latter is the limiting factor.

The source code written in Python/OpenCl is available as part of pyXIT (see appendix A.2 on page 87).

Lens distortion registration

A real space registration algorithm can also be used to register the image distortion caused by a lens distortion which occurs in lens-based x-ray detectors. Measuring two images with a shifted sample can be registered to each other. Using a simple model for the lens shift, the parameter(s) for the lens shift can be found by such a registration. The lens distortion is thereby treated as a coordinate transform and the registration finds this coordinate transform—similar to e.g. a rotation. The coordinate transform is: undistortion→shift→distortion.

3. Theory of x-ray image quality

Overview

This chapter discusses the theoretical aspects of describing the phenomenon of image quality with a physical quantity ("measure"). In the first three sections, prior work on image quality is summarized and the requirements for a good image quality measure are determined. This includes a thorough description and visualizations of the main aspects which determine image quality. In section 3.4, an extension/generalization of existing theoretical models of image quality is derived. Here, the main goal is to uncover cases for which prior theoretical descriptions fail, and predicting the actual physical relationships. The derived model is also a necessary preparation step for the measurement technique using the $DE(u)$. Sections 3.5 and 3.6 present predictions about important physical effects for which there appears to be no clear description in the literature. The last section of this chapter (3.7) discusses indirect detection noise – the relationship to the prior sections is given by the fact that the most common technical implementation of an x-ray detector is the indirect detector and that it has unusual noise properties.

Chronologically, the measurement method for SNR spectra was developed before the theoretical models – paper [1] was published before [2].

3.1. Fundamental Aspects

Optimizing image quality first requires that a quantitative description (model) is found. This model defines a physical quantity whose maximum yields the optimal image quality. Of interest for the optimization are the physical or device parameters that are optimal. Then, a measurement method is required to apply this model to different experimental setups. This chapter develops an image quality model, the next chapter is about measurements.

Image quality models exist for applications in x-ray medical imaging (MI) and nondestructive testing (NDT). These are mainly meant to be used in the standardization of devices, not in optimization. Performance optimization in high resolution x-ray imaging is different from these applications in the following ways:

- Energy-dependencies in the signal strength play an important role, either because they vary strongly over the x-ray spectrum or because a high signal strength is required for a good image quality. Different contrast mechanisms also have different energy-dependencies of the signal strength.
  See fig. 3.1 and fig. 3.2.
- Different contrast mechanisms are used. In addition to absorption contrast, inline or grating phase contrast and x-ray optics based imaging is possible.
  See fig. 3.3 and fig. 3.4.
- Accuracy and completeness are more important for optimization while standardization requires comparability and ease of interpretation. There is also a difference between standardizing specific parts/properties of a device and optimizing the performance that results from the complete x-ray imaging device. Optimization can include performance differences resulting from the measured sample, while device standardization cannot.

The methods used to describe, measure and optimize image quality in MI and NDT assume absorption contrast only and assume the signal strength to be energy-independent. Figure 3.2 shows the energy-dependency of attenuation contrast for some materials. While the energy-independent approximation used in MI can be used there, high resolution imaging uses lower energy x-rays where the signal strength is strongly energy-dependent.

Note that SNR spectra are a quadratic quantity, while temporal SNR is a linear quantity, which means that with respect to e.g. intensity, the scaling is:

$$SNR(u) \propto {SNR_t}^2 \tag{3.1}$$

SNR spectra are commonly used as a quantitative measure to describe image quality. The definition of

the SNR spectrum in the medical imaging literature is [24]:

$$SNR_{\mathrm{MI}}(u) = \frac{I^2\mathbf{h}(u)^2}{N(u)} \tag{3.2}$$

where I is the detected intensity, $\mathbf{h}$ is the MTF and $N(u)$ is the image noise power spectrum. Note that in MI, the use of the Detective Quantum Efficiency ($DQE(u)$) is more common [25, 26], which is a quantity derived from $SNR_{\mathrm{MI}}(u)$ (see section 3.3.2). All these quantities are independent of the contrast mechanism and sample influences.

The definition that will be used in this work is instead:

$$SNR(u) = \frac{S(u)}{N(u)} \tag{3.3}$$

Here, $I\mathbf{h}^2$ is replaced by the image signal power spectrum $S(u)$. This fraction of power spectra is the more fundamental definition of SNR spectra. $S(u)$ includes every possible contrast mechanism, because it represents the detected structure in the actual image. Signal and noise are defined as explained in section 2.3.2 on page 15, where noise is the measurement error and the signal is the measured quantity (truth, not data). In the following, SNR spectra or $SNR(u)$ always refers to the definition according to eq. (3.3).

In NDT, image quality is usually evaluated by determining the MTF $\mathbf{h}(u)$ (spatial resolution) and the (temporal) contrast to noise ratio [27]:

$$CNR_t = \frac{\text{contrast}}{\text{pixel noise}} \tag{3.4}$$

Here, contrast is the gray value difference between different materials. Extensions have been proposed [28], where the MTF and noise power spectrum are included in the CNR:

$$\begin{aligned} CNR_{\mathrm{NDT}}(u) &= \frac{\text{contrast}^2 I^2\mathbf{h}(u)^2}{N(u)} \\ &= \text{contrast}^2 SNR_{\mathrm{MI}}(u) \end{aligned} \tag{3.5}$$

Publication [24] is a good summary of the current state of knowledge, except for two aspects: (1) Energy weighting, see [29]. (2) Contrast, as is it established in NDT imaging.

While the energy-dependency of the signal is represented with the contrast, different contrast mechanisms can not be integrated well. For example for inline phase contrast, the MTF depends both on the sample and the measurement geometry. We will also later see that using temporal quantities (pixel properties) in imaging produces errors (section 3.3.3 and section 3.6). These stem mainly from the fact that most of the imaging physics happens on continuous image spaces and implicitly referencing a discrete element in equations requires a careful consideration of unintended side effects.

Simulations demonstrating on a fundamental level how the (physical) properties of an image affect image quality are shown in figures 3.1 to 3.6. The different figures show different aspects of image quality which are explained later in the text. An advantage of the simulation is that it is possible to display signal, noise and data as separate curves. For the same reason, line plots are here used to represent sections of 2D or 3D images. Measurements on real samples can only show the data. There, signal and noise are unknown quantities—one cannot know exactly what part of the image is signal and what is noise.

The Wiener filter, section 2.3.3, can be used to compute best reconstructions for signal and also noise. These reconstructions effectively separate signal and noise, within the limits given by the knowledge of the measurement process. The SNR spectra measurement method in chapter 4 works by separating signal and noise, but this is only possible for the respective power spectra. Power spectra describe the properties of signal and noise, not the actual values. In the figures, signal is simulated at a higher resolution (12x) than noise/data to approximate a continuous signal. For the simulation code, see appendix A.2.

Figure 3.1 shows line plots of simulated images with a randomly generated signal containing different size scales. Five different regions are shown where noise and signal strength vary. The temporal signal and noise strengths are shown with the bar symbols for each region, computed from the generating physical processes. $S(u)$ and $N(u)$ can be computed from the signal (blue) and noise (orange) within one region. This simulation has identical modulation transfer for all regions; the signal is randomly generated. The regions shown roughly correspond to a real measurement from a step wedge, with structure added. To the left (high image quality), the data closely represents the signal while on the right (low image quality) it does not. Additionally, image features not present in the signal appear in the data to the right. For the lower image quality, it is not possible to determine the actual shape of the signal. The loss of detail resolution is always stronger for smaller spatial features, which is an effect modeled by SNR spectra and explained in section 3.3.5 on page 38.

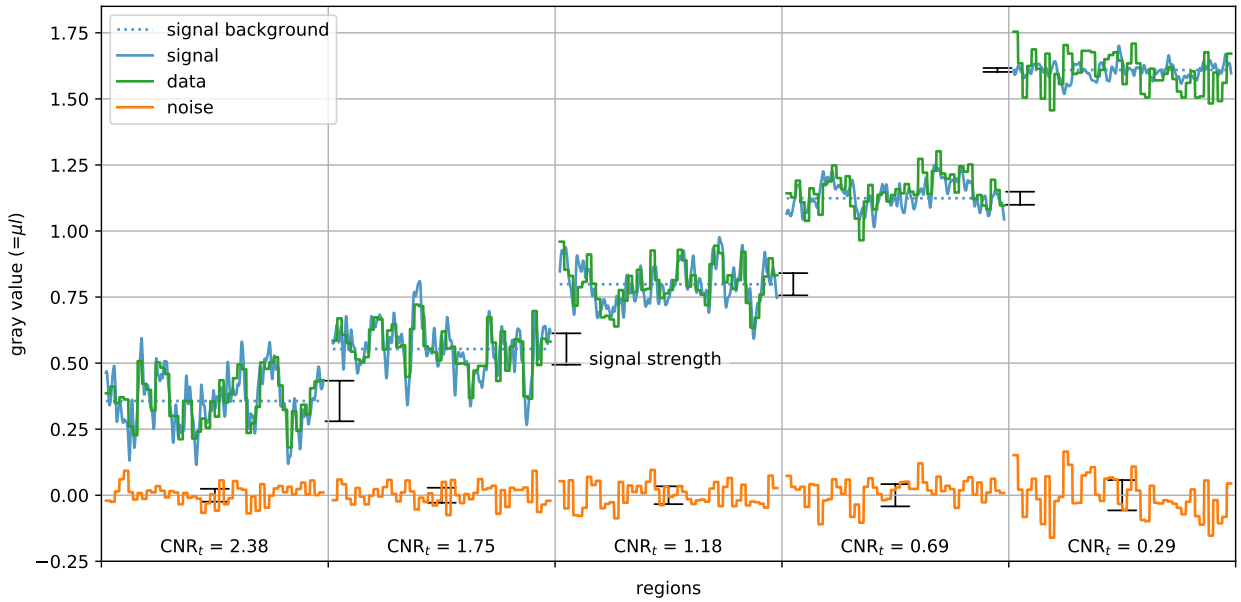

Figure 3.1.: Simulated examples for signal and noise with the image quality decreasing to the right. See eq. (3.4) for CNR_t and section 2.3.2 for data/signal/noise. The main aspect which this figure demonstrates is that signal and noise are principally indistinguishable and only a high SNR/CNR allows reliable measurements. Refer to the text for further explanation.

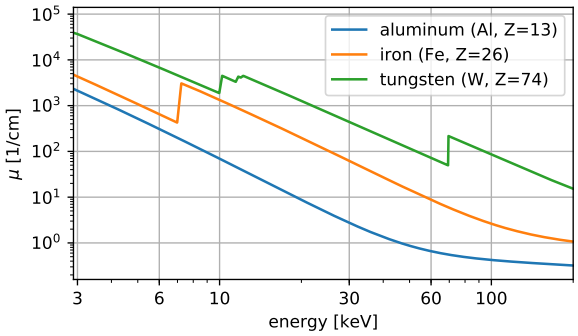

Figure 3.2.: Examples for the signal strength, here given by absorption coefficients μ. For the energy range where photoabsorption is the strongest interaction (e.g. Al below 60 keV), there is a strong energy-dependency. Compton scattering (energy range above) only has a weak energy dependency.

The separation of signal and noise is an important concept in this work, as the fraction of both gives the signal to noise ratio. (Note that the NDT definition of contrast is identical to how signal is here defined.) Both for simulations and for measurements, the separation and evaluation of signal and noise is a fundamental requirement if image quality needs to be analyzed.

Note that the SNR is equivalent to a relative measurement error. Correspondingly, the SNR does not model systematic measurement errors, only random ones. Signal deterioration (e.g. MTF) are systematic errors that also affect the importance of random errors. The systematic blur can be corrected via deconvolution, but the information loss from blur reduces image quality even then.

3.1.1. Image signal power spectra

The main difference between MI and NDT models and the model which is proposed here is the use of the image signal power spectrum $S(u)$ in the numerator of the SNR spectrum fraction. The signal s (and its power spectrum) can have two different meanings:

- The actual shape (density distribution) of the measured sample. This is the sample information which the measurement should determine.
  Data model (κ = signal strength):
  $$d = \kappa h * s + n \tag{3.6}$$
- The static part of the data, generated by the sample. This is the definition used in fig. 3.1 to 3.6 and the rest of the work. Defined this way, deterministic effects on image quality are included in the signal and random effects in the noise.
  Data model:
  $$d = s + n \tag{3.7}$$

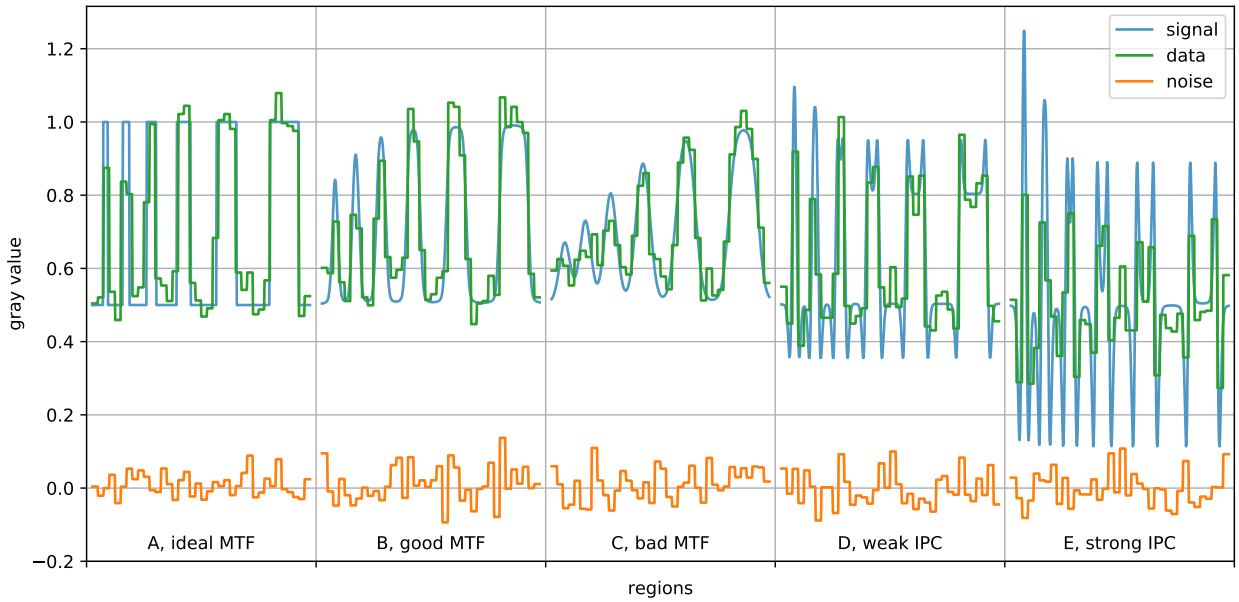

Figure 3.3.: Simulated examples for signal and noise CT images for different signal power spectra. Different modulation transfer scales the amplitude of objects of the corresponding size and is thus an important aspect of SNR evaluations. For inline phase contrast (IPC), modulation transfer is > 1 and therefore improves image quality.

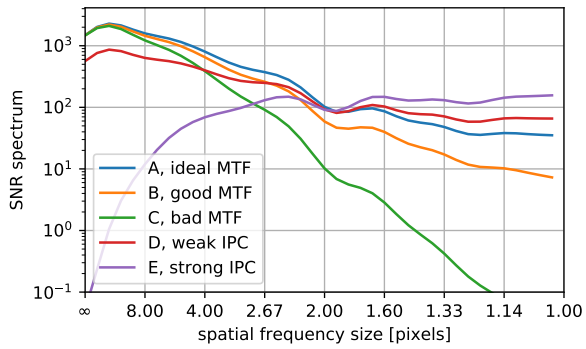

Figure 3.4.: SNR spectra corresponding to fig. 3.3, computed according to eq. (3.3). For interpreting SNR spectra, comparisons are only meaningful at the same spatial frequency size, because all SNR spectra curves include the object spectrum (blue curve). The object spectrum here is given by a superposition of $\mathrm{sinc}(ud)^2$ with different d, which produces the oscillations. The increase of the SNR for E to smaller details is unrealistic for measurements on real systems, it stems from the fact that the simulation is in 1D.

If the SNR spectrum is meant to describe image quality, only the latter of these definitions makes sense. The signal strength and modulation transfer do affect image quality and both depend on the experimental setup. In eq. (3.7), both effects are included in s and therefore do not appear explicitly.

Using the signal power spectrum in the SNR spectrum has the following advantages:

- $S(u)$ represents different contrast mechanisms. Any process which transforms the sample structure into a static signal on the detector is modeled, even a superposition of different contrast mechanisms, see fig. 3.3.
- $S(u)$ can be seen as a complete model. Everything which affects the image can be modeled, as long as it also influences the image power spectrum.
- Measuring $S(u)$ is possible for real applications, see chapter 4. This measurement is much simpler than e.g. a separate measurement of CNR_t and MTF. The relative importance of CNR_t and MTF is correctly represented in $S(u)$. $S(u)$ and $N(u)$ can be determined at once for the same sample region.
- The SNR spectrum defined as the fraction of two power spectra is a unit-free quantity. This reduces the possibility of errors that originate from the

unit scale. See section 3.6 for an example for an error of this type.

- As we will see later (e.g. eq. (3.27)), polychromatic superposition of intensities can be modeled very well using $S(u)$. This fact allows predicting image quality from the properties of the experimental setup.
- $S(u)$ is a good starting point for simplifications, see e.g. eq. (3.31). In general, $S(u)$ can be written as a product of influencing factors and a simplification is done by dividing $S(u)$ by the specific influence (normalization). This approach has two advantages:
  - Experimentally, the quantity that $S(u)$ should be divided by can be determined, see section 4.1.5 on page 59.
  - It is clear what approximations a simplification implies and in which cases it is accurate enough.

The main disadvantage of using the signal power spectrum is that it may represent too many effects. While the object power spectrum shape (see section 3.3.5) is a real effect and does describe image quality, it does not describe imaging performance. The latter is a property of the experimental setup while the former differs in that all sample influences need to be represented. This is further discussed in section 3.4.2 on page 39.

The SNR spectra model based on the image signal power spectrum used here is a more general image quality model than those currently in use for MI and NDT. Its broader range of applications and physical situations is required both for optimization and for high-resolution x-ray imaging individually, and especially for the combination of the two.

Additionally, an effect like a sample-dependent MTF is modeled by $S(u)$. This is caused by an MTF which is energy-dependent and a sample whose signal strength and transmitted intensity are energy-dependent also, see eq. (3.30). The energy-dependency in both couples MTF and sample. MTF measurement procedures typically assume that the MTF does not differ for different samples, as the MTF is seen as a device parameter. That this device parameter can be influenced by the used sample is counter-intuitive when analyzing MTF, but an integral part of the SNR spectra analysis. When using SNR spectra, the MTF is part of the physical model for SNR spectra. The sample-dependent MTF can also include (inline) phase contrast.

Figure 3.3 shows simulations for CT images with line plots of rectangular objects of different feature widths. Shown are five different regions with different signal power spectra shapes, caused by different modulation transfer (A-C) or a different contrast mechanism (D+E). The inline phase contrast (IPC) is modeled according to eq. (3.13) and has an effect similar to a spatial high-pass filter. The attenuation strength in the IPC examples is adjusted down to simulate weakly absorbing materials. See fig. 3.4 for the corresponding SNR spectra. Examples D and E include modulation transfer (blur) identical to example B. The rectangular structures are not aligned with the pixels, but they are identical for all regions. Cases B, D and E may result from the same experimental setup but sample materials with different atomic numbers.

3.1.2. Image noise power spectra

The noise power spectrum is the denominator of the SNR spectrum (both definitions) and the $CNR_{\mathrm{NDT}}(u)$. Increased noise at a specific spatial frequency range means that structures of this size are more difficult to detect. Higher noise amplitude at a spatial frequency means a higher probability that a structure of the corresponding size is generated by noise. This probability is equivalent to the probability that image structure in a measurement was produced by noise instead of sample structure (signal). Human vision is used to white noise, where the noise power is independent of the spatial frequency.

In fig. 3.5, signal and noise simulations for white noise and two strengths of color noise are shown. (Color noise here generally means non-white noise.) The widths of the signal image features in pixels are [1.0, 1.8, 3.1, 5.4]. Corresponding SNR spectra and noise power spectra (NPS) are shown in fig. 3.6. The noise power spectra are simulated according to eq. (3.92) on page 53, where the ”weak color noise” is roughly equivalent to a lens-based indirect detector (c = 3) and the ”strong color noise” to a flatpanel indirect detector (c = 100). Noise strengths are adjusted in such a way that the temporal standard deviation in the regions is the same. Strongly colored noise here means that the coarser structure sizes have a relatively lower SNR. In the line plots, strongly colored noise produces more artificial structures of coarse sizes, but less at fine structure sizes.

Due to the fact that the structures generated by

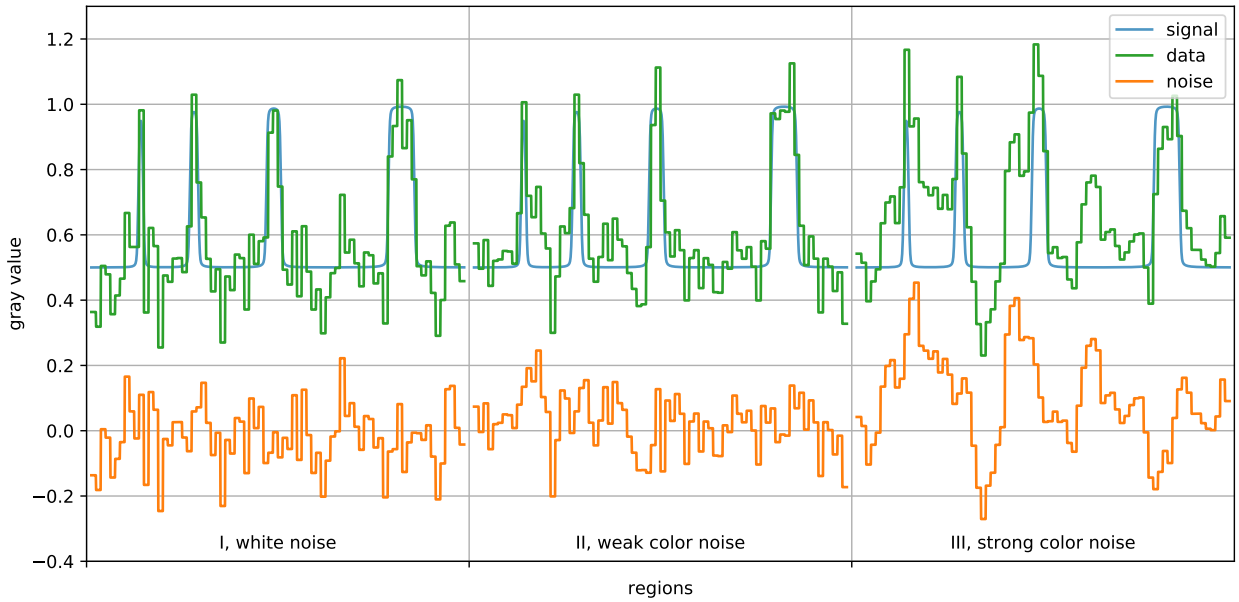

Figure 3.5.: Simulated examples for signal and different types of noise, $CNR_t = 1.25$. Reliable detection requires that objects of a similar shape as the signal are only infrequently produced by noise. Therefore, the shape of the objects generated by noise is important for an evaluation of image quality.

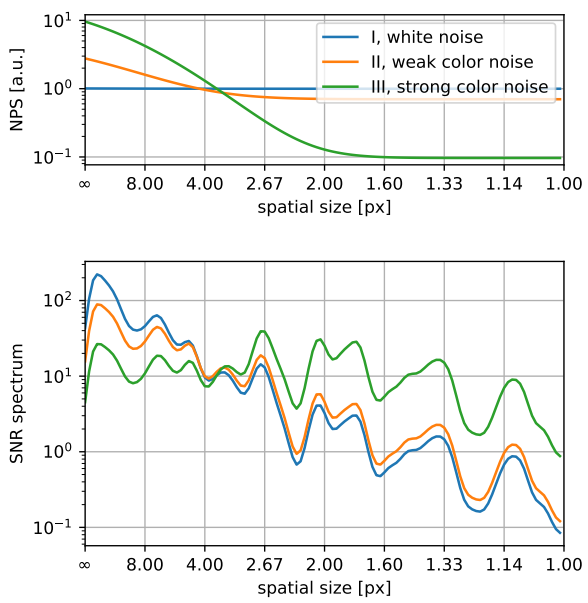

Figure 3.6.: NPS (top) and SNR spectra (bottom) corresponding to fig. 3.5, computed according to eq. (3.3).

noise typically have a different shape than real structures, the actual effect on image quality is difficult to determine. A smart observer expects specific shapes as sample structure and uses this knowledge to better differentiate signal and noise.

Larger image features are generated more often by color noise than by white noise. Successful detection requires that not only image features present in the signal are detected correctly, but also that only the real signal is detected as such. This aspect is a standard problem in decision theory, see table 3.1. Image quality is low if the observer is unable to reliably decide what the actual structure of the measured sample is. This work focuses on optimizing the information content of a measurement and enable the observer to make sound decisions. Optimizing how the observer makes use of the information in the data is not considered in this work.

feature	does exist	does not exist
detected	correct positive	false positive
not detected	false negative	correct negative

Table 3.1.: Decision error matrix, adapted for detection. Detected or not is an observer decision. False positive and false negative are the possible errors and both need to be avoided, the relative importance depends on the base rate of features and the application (cost of each error). If for example there are only very little features in the data, avoiding false positives is more important.

Comparing fig. 3.4 and fig. 3.6, differences in signal or noise power spectra may produce similar SNR spectra shapes—less signal or more noise is equivalent for

image quality. Applying a deconvolution to produce the same signal shape also acts on the noise and can be seen to produce an effective noise power spectrum. Phase retrieval [11] is a type of deconvolution, and a phase retrieved image may show significant color noise. In general, color noise can be simulated by applying a Fourier filter to white noise. The random signal in fig. 3.1 is also simulated this way.

3.1.3. Evaluation types

Different types of optimizations and evaluations require different approaches. Finding a good physical model for image quality depends on what the purpose of an evaluation is, and the importance of certain disadvantages and advantages of a model may differ.

To decide which type of evaluation is useful, I differentiate between four types of performance evaluation problems. Higher types are generally farther from the actual physical situation but easier to interpret. The evaluation types are:

(I) Optimization: Of interest is the combination of parameters which lead to the optimal performance for a specific measurement. While it is of critical importance that the performance measure quantitatively represents all influencing effects, an absolute scale is not necessary.
Example: $SNR(u)$ with specific sample.

(II) Comparison: Of interest is a comparison of the performance of different imaging devices. The comparison must thus be done for example with a defined test phantom. There are practical problems, for example the optimal detector performance for one application may require different x-ray spectra.[1]
Example: $SNR(u)$ with defined test phantom.

(III) Absolute measure: Of interest is how good the performance is on an absolute scale. Differently from type (II), the definition of the quantity cannot include a specific test phantom shape. It must still include the test phantom thickness (in the beam direction), as this influences the detected x-ray spectrum.
Example: $DE(u)$ (see section 3.4.2), ($CNR_{\mathrm{NDT}}(u)$).

(IV) Standardization: Quantities which describe device performance and are comparable between different devices. Different from type (I) to (III), the focus of standardization is on the x-ray imaging device, not the application or an optimization. Efficiencies are typical examples of such quantities.
Example: $DQE(u)$ (see section 3.3.2), QE

SNR spectra are a powerful tool for type (I) problems and can be used in almost any experimental condition without specific adaption. For type (II) problems, SNR spectra can be used if a defined sample ("test phantom") is used. Later in this work, the SNR spectra will be extended to cover type (III). For optimization problems, type (IV) evaluations generally give only partial answers and may be inaccurate.

For simulations meant to find an optimum, there is no difference between the types—the optimum is always identical. On the other hand, higher types may be required to enable comparability between measurement results. Higher types are therefore a practical solution to challenges of the measurement processes. The higher the type, the higher the possibility that the evaluation is too far removed from the specific application. In that case, accuracy is low.

Designing a good physical model is made easier if the problem is fundamentally analyzed. The criteria formulated in the following help to decide if a specific model for x-ray image quality is suited for its task. A simplification of a model is appropriate if necessary effects are still represented correctly by the simplified model. The simplification levels used here are shown in fig. 3.7.

The different evaluation types use quantities that are either defined on a relative or absolute scale. For a quantity on an absolute scale, the absolute value has a defined meaning. Quantities on a relative scale may include arbitrary scaling factors, for example $P(u)$ in eq. (3.30). A relative scale therefore only has meaning when measurements are compared with each other. The scaling factor needs to be kept constant between measurements to enable comparability.

3.2. Model design criteria

3.2.1. To include

To design a good model, one needs to first consider what the fundamental problem is and what the effects

[1] The x-ray detection efficiency spectra for different detectors may e.g. be responsible for detectors being differently tolerant of high degrees of polychromaticity. This is shown in fig. 3.14.

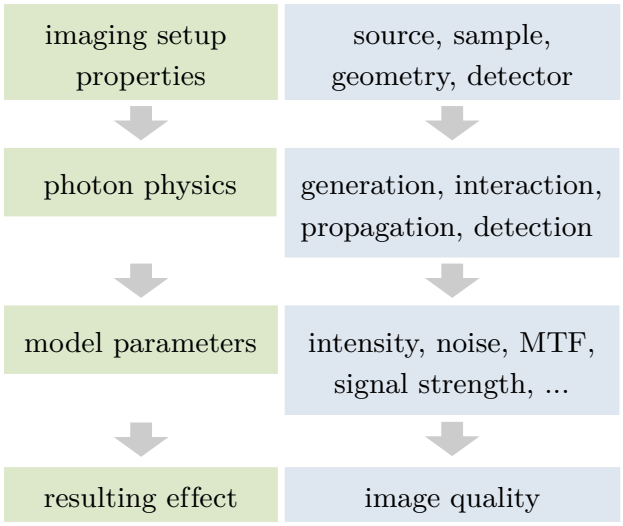

Figure 3.7.: Hierarchical representation of a possible simplification path for a physical model of image quality. The levels from top to bottom represent an increasing level of abstraction and simplification. Each step includes approximations. The first level is the physical reality, the fourth level the purpose of the measurement. The category of description is on the left and that which is described on the right. The main focus of this chapter is on the lower two levels.

that need to be included in the model are. Generally, all factors which either influence the magnitude of the signal or the noise need to be included. In x-ray imaging, the following effects need to be considered:

(A) Noisiness (intensity/poisson noise and other)
(B) Modulation transfer (MTF)
(C) Signal strength (attenuation, phase contrast or other)
(D) Superposition of different x-ray photons (e.g. Polychromaticity)
(E) Presence of artifacts ($\approx$ noise)

Effects (A) and (C) are demonstrated in fig. 3.1 and 3.5 and effects (B) and (C) in fig. 3.3 on page 26. The signal power spectrum includes effects (B)—(D) and the noise power spectrum (A) and (D).

(A) Noisiness

Noisiness describes the effect that if a data feature cannot be reliably identified as originating from the sample, detection is impossible. Strong noise means that the noise may generate data features that are identical in shape to real object structure. Then reliable detection is impossible, because a data feature that is present in a measurement may have resulted either from noise or from the sample.

Here, I define noisiness as the absolute strength of the noise. The relative strength is given in combination with effects (B) and (C).

In an imaging process using quanta (e.g. photons) as information carriers, the measurement uncertainty is given by the Poisson distribution for the detected photons. This means that for a given average intensity I, the probability to detect k photons is given by:

$$p(k|s) = e^{-I}\frac{I^k}{k!} \tag{3.8}$$

Using the linear noise model, eq. (2.33) (here: $k = I + n$), we can rewrite this to:

$$p(n|I) = e^{-I}\frac{I^{I+n}}{(I+n)!} \tag{3.9}$$

The variance describes the noisiness and is given by:

$$\mathrm{Var}\{k\} = \mathrm{Var}\{n\} = I \tag{3.10}$$

With the normalization, eq. (2.1), we can derive

$$p(d|I) = p\left(\frac{I+n}{I}|I\right) \tag{3.11}$$

which means for the noisiness of the normalized x-ray image:

$$\mathrm{Var}\{d\} = \frac{1}{I} \tag{3.12}$$

As expected, a higher average number of photons means a lower noisiness. For indirect detectors see section 3.7. Signal and noise scaling with intensity depends on if the images under consideration are normalized or not. For normalized images, signal does not depend on intensity while for non-normalized the image gray values are scaled by the intensity. The relative noisiness is the same.

(B) Modulation transfer

A measurement apparatus with a bad MTF suppresses the amplitude of smaller signal features. This lower amplitude may then be too low compared to noise and reliable detection becomes impossible. See section 2.2.1 on page 11 for a theoretical description.

An example which is of practical importance for lens-based x-ray detectors [30] is the diffraction limit and the corresponding MTF that results from a superpostition of defect of focus [31]. Modulation transfer can also be understood as a influencing factor for the

signal strength, depending on the structure size. As the physical processes generating modulation transfer and signal strength are different, a separate evaluation allows a clearer representation of effects.

(C) Signal strength

The signal strength is given by the amplitude of the signal, in some contexts this quantity is identical with the contrast. A higher signal amplitude means that the signal is easier to differentiate from noise. From a simplified point of view, signal strength is only of interest relative to noisiness. The physical process by which signal strength is generated is completely separate from the noise processes, so these effect should be considered separately. Superposition (D) also works very different for noise and signal. This separation is therefore particularly necessary for polychromatic imaging.

Inline phase contrast signal strength can be modeled as a modulation transfer effect of the following form [11]:

$$\mathbf{h}_{\mathrm{IPC}}(u, E) = 1 + p(E)^2 u^2 \tag{3.13}$$

where $p(E)$ is the relative signal strength of phase contrast to attenuation contrast. The effect of on an image is demonstrated later in fig. 3.9. $\mathbf{h}_{\mathrm{IPC}}(u, E)$ has an effect similar to a highpass filter, see fig. 3.3 on page 26 for examples. This MTF is defined as one acting on the attenuation image. IPC is weak at lower spatial frequencies, therefore the lower spatial frequency information is always given by the attenuation contrast. An IPC measurement produces its image quality therefore always from a mix of attenuation and phase contrast. The parameter p is given by [11]

$$p^2 = \frac{z\delta}{\mu_{\mathrm{abs}}} \tag{3.14}$$

where δ is the real increment for the diffraction index given by:

$$n = 1 - \delta + i\beta \tag{3.15}$$

and z is the effective phase contrast propagation length given by [32]:

$$z = \frac{l_{\mathrm{SDD}}}{M} \tag{3.16}$$

Here, M is the x-ray magnification in cone geometry ($= 1$ in parallel beam) and l_{SDD} is the distance between sample and detector. The energy dependency of IPC is given by $\delta(E) \propto E^{-2}$ [8] in the range of energies used for x-ray imaging. Typically, inline phase contrast is visible if the spatial resolution of the imaging setup is better than the fringe spacing $\sqrt{z\lambda}$ [33] (λ: x-ray wavelength).

(D) Intensity superpositon/Polychromaticity

Superposition of the different x-ray photons is what happens when a polychromatic x-ray image is detected. A model for image quality needs to correctly describe what effects the superposition of photons with different properties has.

(E) Image artifacts

Image artifacts are mentioned here for completeness, they may significantly deteriorate image quality. Although a quantitative analysis of image artifacts is not done in this work, a short summary of the most important image artifacts in polychromatic x-ray imaging and CT is given in the following.

- Detector pixel defects. Single pixels in a detector pixel matrix may have different deviations from the typical physical behavior of the other pixels. They may e.g. have a significantly higher dark current (hot pixel), stop working altogether or have a significantly different gray value response on incident intensity.
  - Can be corrected by a interpolating the affected pixels from neighbouring pixels (bad pixel map) and by a multigain correction method.
  - Affect the higher spatial frequencies.
- Ring artifacts, visible as rings in the CT image (centered on the rotation axis of the sample). Is typically caused by some types of detector pixel defects, but especially by local detector area having a different gray value response. They are therefore typically worse for samples having high transparency difference in a CT scan. Phase contrast measurements also show more pronounced ring artifacts after phase retrieval.
  - Can be corrected by ring filters, if the sample structure is not too ring-like. Very narrow rings can usually be corrected well. Ring filtering can add artifacts if applied wrong.
  - Affect low to medium spatial frequencies after application of an effective ring filter.

- Beam hardening. Caused by preferential absorption of x-rays with higher interaction cross sections. In a CT, this leads to higher gray values of areas with lower material thicknesses and streak artifacts originating from views with locally very high attenuation thickness.
  - Can be corrected by using a polychromatic look-up table for intensity → thickness.
  - Affect lower spatial frequencies.

- Insufficient volume sampling. Is caused by having too few projections in a CT scan reconstructed via FBP. More severe for local tomography scans due to the fact that these artifacts can also be produced by sample structure outside of the field of view.
  - Can be corrected using a sufficient number of projections. Can be alleviated by continuously rotating the sample during image acquisitions.[2]
  - Affect medium spatial frequencies.

- Local tomography artifacts. Are caused by the sample being larger than the field of view, so that a tomographic reconstruction can no longer be exact (see section 2.4 on page 17). The effect is spatially distributed according to the PSF of the ramp filter, so that high frequency errors appear only on the outer edge of the FOV and the whole CT volume can have an absolute gray value shift error.
  - Can be corrected by good filter padding or by estimating the shape of the object.
  - Affect mainly low spatial frequencies.

- Cone beam CT artifacts, see 2.4. Caused by a CT scan path which yields incomplete information.

- Wrong CT geometry. Can be caused either by the assumed static geometry of the scan being wrong or by dynamic changes in the CT geometry which were not included (e.g. sample drift). Depending on the geometry parameter being wrong, the effects are different kinds ob blur in different volume regions. In high-resolution imaging, these kinds of artifacts are much more common due to the required mechanical precision being higher.
  - Can be corrected by determining and using the correct CT geometry (calibration).
  - Affect high and medium spatial frequencies.

Note that pyXIT (see section 2.4.4) has algorithms to correct these artifacts insofar as they can be corrected through image processing.

3.2.2. To exclude

There are also effects that do not influence what is modeled and therefore should not influence the model. If they erroneously do influence the model quantity, it is an error of the model. Considering (polychromatic) x-ray image quality, the following aspects exist and the image quality measure must be designed in such a way that they do not influence it:

(I) Discrete sampling of a continuous signal

(II) Digital blur filters applied to the data

(III) Gray scale changes

(IV) Data presentation and observer performance

(I) Discrete sampling

The signal is a continuous function, but the measurement process by necessity samples this function at discrete points. Nonetheless, if this sampling does not deteriorate image quality, then the properties of the sampling must not influence an image quality measure. A deterioration of the image quality happens when the pixel size is larger than the features that should be resolved. Note that the feature size may also be given by the required precision for the surface of a larger object.

(II) Digital blur

Applying a digital blur to an image after the measurement changes how an observer may interpret an image, but the information content is unchanged (the filter is fully reversible). An image quality measure from the standpoint of optimization should therefore work this way: It should quantify the information gathered by a measurement, not what an observer can interpret in a specific representation of the data. Note that an ideal representation makes use of all the information in a measurement, so then both concepts are identical.

[2] The continuous rotation blurs the edges from the outer objects. It is also a closer approximation of the continuous sinogram integral, because it only has geometrical inaccuracies.

If the digital blur is a deconvolution, then this deconvolution may increase the usefulness of the data for an observer. This would be the reconstruction of the signal from the data, which generates comparable representations of the data. Using an image quality measure which is not influenced by digital blur gives a large degree of independence of the analysis from the data representation. See section 2.3.3 for a discussion on signal reconstruction.

(III) Gray scale changes

Multiplying the gray values of an image with a factor does not change the information content or the image quality of an image. Both the definitions of temporal SNR eq. (3.17) and SNR spectra eq. (3.18) are such that scaling both signal and noise does not change SNR. Any quantity describing image quality should be invariant under gray value scaling.

Beam beam hardening correction (BHC) multiplies the gray value of the projections with scaling factors (typically > 1) to correct beam hardening artifacts. If for a BHC-corrected image, the noise is estimated from the background intensity, then a derived image quality measure will appear to increase due to the BHC increasing the signal strength. This is not an effect which is caused by a real increase in image quality, but instead shows that an error was made. Noise determined from the actual image area will scale identically and e.g. the SNR spectrum measurement (see chapter 4) is unaffected. Beam hardening correction does increase image quality by reducing a systematic error, but SNR is unaffected per definition. This increase in image quality appears only for large structure sizes, as the visibility of fine detail is unaffected by BHC.

(IV) Data presentation and observer performance

Of specific importance for visual evaluation/comparison of images acquired under different configurations is the data presentation. This describes how the measured values (image pixel gray values) are translated to the display (e.g. screen pixel brightness and color). Display devices may have a limited brightness range (contrast) and it is then only possible to resolve a narrow gray range in the data as presented.[3] It may therefore be necessary to view a x-ray image at different gray ranges to get all the information. Visual estimation of image quality is unreliable in general and should be avoided for quantitative work, but it may be useful as a safety measure for the quantitative analysis—to find errors in the evaluation done.

If one does a visual presentation of data, care must be taken for the following aspects:

- Gray scale: How the physical image gray values are translated to displayed brightness or color. If e.g. the signal strength is different, the gray scale needs to be adjusted for each image relative to the signal strength.
- Blur: If images with different blur are shown, this should be the only difference. The exact evaluation if e.g. a lower noisiness compensates a higher blur should be left to a quantitative analysis. Note that the amount of blur may be influenced by changes in the experimental setup, and in that case visual comparison is difficult.
- Interpolation: As a general rule, data presentation of image data should avoid interpolation whenever possible, because interpolation introduces blur. Zoom should then be implemented in integer steps (..., 50 %, 100 %, 200 %, ...), where lower zooms are generated by binning of pixels and higher zooms by filling a (n·n) pattern of pixel with one gray value. See e.g. the implementation of the image viewer in pyXIT. It is possible to avoid interpolation by sampling the image to a higher resolution before displaying (as above), even if the interpolation cannot be switched off in the way an image is displayed.

It could be argued that the actual usefulness of a measurement is given by the amount of information a human or machine observer can extract. The performance of an observer is such a complex phenomenon that including this effect into an image quality optimization leads to difficulties. I propose the following approach: Image quality is defined as the amount of information present in an image. If this quantity is determined, evaluating the observer performance is a useful next step. This evaluation needs to take the effect of data presentation very carefully into account.

A higher information content in an image should always result in a better observer performance, otherwise data presentation or training are not optimal. It is then of course much simpler to optimize the former instead of the latter, which is the approach chosen in this work. Both have the same optima after all.

[3] There exist special computer monitors for radiography, which have a higher contrast and thus show more information at once.

Optimizing the data presentation to make full use of the information in different measurements would complement such an image quality optimization.

While this approach may appear impractical, technological improvement should not be limited to the practical performance achievable today. Instead, the performance achievable in the future needs to be considered, where changes in the design and use of a technology are possible.

3.2.3. Visual demonstration

To demonstrate the different physical phenomena that appear when evaluating x-ray image quality, different cases are shown visually in fig. 3.8 and fig. 3.9 with the randomly placed ball patterns. These images are constructed in such a way that the detection of an image feature (here: balls) is physically as close to the real situation as possible. Detection in this case means that an observer can reliably determine if a feature is present at a specific position. This simulation complements the ones in figures 3.1 to 3.5 in that it is closer to an observer doing measurements but does not show both signal and noise. Some less obvious properties that need to be represented are:

- The position of an image feature must be random to avoid detection from prior knowledge. If the observer already knows that features can only be at specific positions, detection is made artificially easy by making false positives impossible.
- Partial pixel area effects and sub-pixel object placement must be simulated e.g. by oversampling the original simulation and then binning down.
- Different object sizes must be simulated, different object shapes may be useful.
- The material density of the smaller features needs to be increased so that the gray scale of the features is identical. This is done to have comparability of different feature sizes in the data presentation. Note that if we do a simulation on CT images, using an identical density instead would be required.

The simulation is done in the following steps: (1) compute the average intensity at a much higher pixel sampling (2) downsample to the actual resolution (3) simulate Poisson noise. The first step may include a blurring (here: Gaussian MTF) and defines the shape and signal strength of the image features. The intensity (noisiness) is also set in the first step.

The difference to similar simulations e.g. in [24] is that here the placement of the features is random.

This demonstration can show in general what affects image quality, but it also becomes obvious that the precision of a human estimate is not sufficient. In the second line of images d)–f), we see that changing the intensity by a factor of 3 makes an obvious difference. Much smaller differences could not be evaluated correctly by a human observer.

The resulting effect on image quality is the same for noisiness or blur: Smaller image features can or cannot be detected. As both effects affect the same result, an image quality measure should also represent these effects.

In the digital version of this document, the code used for the simulation can be downloaded in appendix A.2 on page 87.

3.3. Model comparison

3.3.1. Signal to noise ratio

The signal to noise ratio gives the strength of the signal in relation to the strength of the noise. It can be understood as an (inverse) relative measurement error. This concept is based on the fact that signal can only be reliably detected if it is stronger than the noise (relative error $\ll 1$). While it is clear that higher SNR is better, defining a sufficiently high SNR depends on the application. The definitions of the temporal SNR_t and the SNR spectrum are:

$$SNR_t = \frac{\text{pixel mean signal}}{\text{pixel standard deviation}} \left(= CNR_t \right) \tag{3.17}$$

$$SNR(u) = \frac{\text{image signal power spectrum}}{\text{image noise power spectrum}} \tag{3.18}$$

u is the spatial frequency and $SNR(u)$ is the SNR spectrum. By "signal", sample structure is meant, not the image gray value itself. Here, SNR_t is defined identical to a contrast to noise ratio (CNR_t)—the contrast *is* the signal. This difference becomes important when different material interfaces produce the sample structure of interest. CNR_t is a quantity typically used in NDT applications. The definition of SNR_t here is consistent with how $SNR(u)$ is defined. Signal is here describes the information that is meant to be found by the measurement.

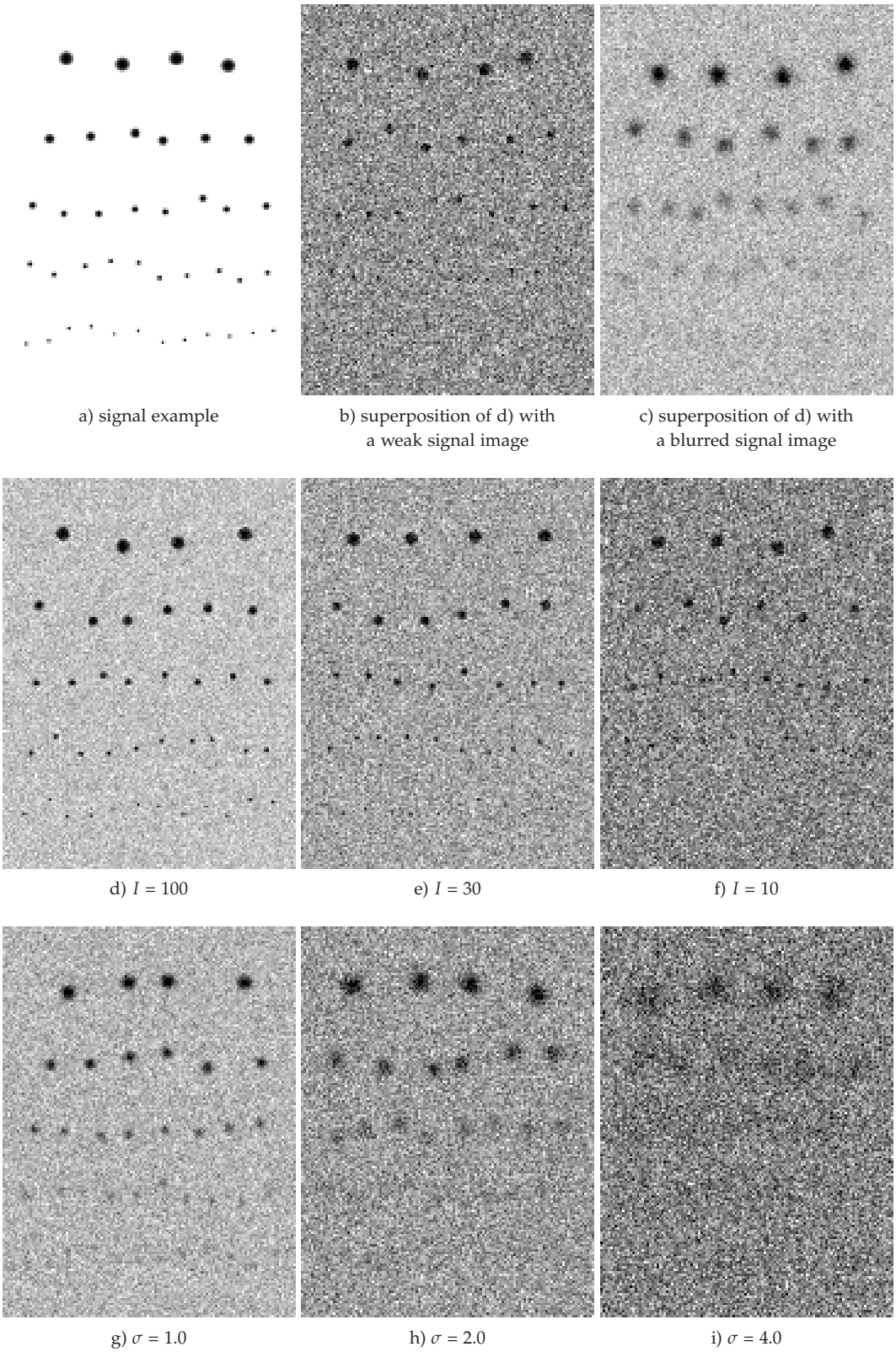

a) signal example

b) superposition of d) with a weak signal image

c) superposition of d) with a blurred signal image

d) $I = 100$

e) $I = 30$

f) $I = 10$

g) $\sigma = 1.0$

h) $\sigma = 2.0$

i) $\sigma = 4.0$

Figure 3.8.: Simulated x-ray projection images of randomly placed balls of different sizes (diameters: 6.0, 4.2, 3.0, 2.1, 1.5); the number of balls for each size is identical (number: 4, 6, 8, 10, 12). A higher image quality means that smaller image features can be detected reliably. Images b) and c) are generated by adding another image to d); in both cases this reduces the image quality because the added image has a lower image quality than d). For d)–f), I scales the intensity (noise), a higher intensity corresponds to a higher image quality. For g)–i), σ is the standard deviation of a Gaussian MTF, a higher blur corresponds to a lower image quality.

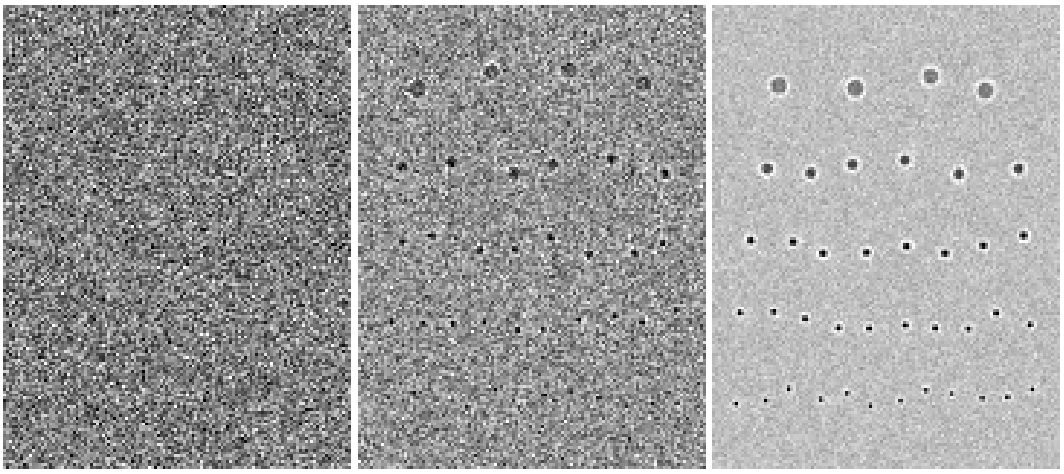

a) no phase contrast b) weak phase contrast ($p = 20$) c) strong phase contrast ($p = 40$)

Figure 3.9.: Simulated x-ray projection images for inline phase contrast as given by eq. (3.13). Blur and intensity are identical for the above three images, the (attenuation) signal strength is low. A higher phase contrast strength corresponds to a higher image quality. Due to the higher SNR gain at higher spatial frequencies, phase contrast increases image quality more for smaller features.

SNR_t is a linear quantity while $SNR(u)$ is a squared quantity. The former is proportional to the signal amplitude while the latter is proportional to measurement integration time.

As discussed in section 3.1, the SNR spectrum includes all important effects on image quality but may also include additional (unwanted) effects. Simplified definitions of the $SNR(u)$, for example eq. (3.2) and eq. (3.5), do not include these unwanted effects. Depending on how the simplification was done, additional problems may appear if the simplification excludes significant effects.

3.3.2. Detective quantum efficiency

A *DQE* is defined as a *SNR* transfer function to describe and optimize one part of the imaging device. Usually it is applied to describe the x-ray detector in medical imaging applications. It is generally calculated in the form

$$DQE = \frac{SNR_{\text{out}}}{SNR_{\text{in}}} = \frac{SNR_{\text{detected}}}{SNR_{\text{ideal}}} \in [0, 1[\qquad (3.19)$$

Note that the definition of the *SNR* used here is eq. (3.2) and not eq. (3.3). This is intended to give an absolute optimum if $DQE = 1$. There exist many derived expressions for certain applications (simulation [24, 25] or measurement [26, 34]). The common simplified expression for the *DQE* of an indirect detector is:

$$DQE(u) = \frac{a}{1 + c^{-1} H_v(u, E)^{-2}} \qquad (3.20)$$

where a, c and $H_v(u, E)$ are the spectrally averaged x-ray absorption efficiency, x-ray photon conversion factor and optical (scattering) MTF. We can see by comparing to eq. (3.30) that using this spectral average is possibly incorrect. Effects from different samples or source/detector interactions are excluded by design in such a simplification, as the *DQE* is meant to describe the detector only.

SNR_{ideal} and SNR_{detected} depend on the sample, which has a x-ray energy dependent transmission. This effective x-ray spectrum would need to be considered to correctly compute a polychromatic *DQE* and can be strongly sample-dependent.

Using a monochromatic *DQE* at different energies does not pose such problems. This is the standard approach for characterizing detectors for optical light (CMOS/CCD) [35], in which a similar quantity is called quantum efficiency (QE). It is the only application of the *DQE* concept in a polychromatic context which is accurate.

In 1985, a paper was published [29] about how to apply the DQE concept to polychromatic x-ray imaging. The authors found that energy weighting (see section 3.4.6) needs to be considered to correctly compute the DQE. Later works [24, 25] did not take these conclusions into account and therefore DQE (as generally accepted) has become a model which can only be used within the narrow range of approximately monochromatic applications. See eq. (3.54) for the approximation which defines the possible range of

applications.

Around the year 2000, energy resolving detectors were analyzed theoretically, and the concept of energy weighting was again considered in its consequences for DQE [36, 37].

3.3.3. Indirect detection

Generally, two types of x-ray imaging detectors can be differentiated:

- Direct detectors: These detectors count single x-ray photon detection events. They are principally able to determine the x-ray energy of a detected photon. They are also called (photon) counting detectors.
- Indirect detectors: These detectors first convert x-ray photons into visible light which is then detected. They usually integrate all events in a certain time frame, weighted by the energy of the x-ray photon. They are also called (energy) integrating detectors.

Due to the fact that indirect detectors are currently much cheaper to produce, most x-ray imaging setups use this kind of detector.

For indirect detection, the noise power spectrum $N(u)$ is not a white spectrum, but is instead influenced by the detector MTF in the following way ([38] or eq. (3.92) on page 53):

$$N(u,E) = I(E)\left[c(E)^2 H_v(u,E)^2 + c(E)\right] \tag{3.21}$$

where E is the x-ray energy, $I(E)$ is the detected x-ray intensity and $c(E)$ the conversion factor from x-ray photons to visible light photons. This equation is only valid for monochromatic x-rays and for a simplified imaging setup, but the general shape of $N(u)$ is identical for polychromatic spectra on real setups. In a CT measurement, the reconstruction algorithm will also influence volume image noise.

The pixel noise σ_t (temporal standard deviation) for a noise power spectrum $N(u)$ of a projection is given by Parseval's relation [12]:

$$\sigma_t^2 = \frac{1}{A}\sum_{x,y} N(u_{x,y}) \tag{3.22}$$

where $N(u_{x,y})$ is one discrete Fourier coefficient and A is the number of these coefficients. Computing or measuring a σ_t for an indirect detector does not give useful results even for noisiness effects, because noise at all frequencies is averaged, although it may not decrease image quality at the structure size that is of interest. See also fig. 3.5.

If the image quality is reduced by decreasing $H_v(u,E)$, both SNR_t and DQE_t will increase due to a decreasing σ_t. Changing $H_v(u,E) = 1$ to $H_v(u,E) = 0$ decreases σ_t by a factor of $\sqrt{c+1}$. If technically feasible, $c > 100$ is achieved in detectors built today. This effect can therefore be large. In other words, sharper indirect detectors are also temporally noisier. The *SNR* spectrum instead indicates that they have relatively weaker noise, which is correct.

The above stated effect has the following technical application for lens-based indirect x-ray detectors: Lens-based high-resolution x-ray detectors often require active focusing of the optics (focus plane) on the scintillator sheet. From the equations above we can derive that the point of maximal sharpness is the point at which the temporal noise of the image is maximal (using arbitrary x-ray light). This allows to build a reliable auto-focus mechanism that works without an object in the beam. Note that the focus planes of signal and noise may be slightly different due to the different superposition of signal and noise.

Similar effects are produced by artifacts. Beam hardening artifacts or ring artifacts may e.g. decrease the $SNR(u)$ at lower frequencies but fine detail can still be detected well. A temporal *SNR* cannot differentiate between low-frequency and high-frequency noise.

3.3.4. Modulation transfer function

The modulation transfer function (MTF, see also section 2.2.1) is typically measured via a tilted edge test phantom. This is then combined with the NPS and intensity or a temporal measure (e.g. SNR_t) when analyzing image quality (see eq. (3.2) and eq. (3.5)). If the MTF is energy-dependent, then not only this combination fails but also the MTF that acts depends on the sample. Due to beam hardening, different sample thicknesses produce different detected x-ray spectra in the corresponding detector region. The energy-dependent MTF is therefore weighted differently in different regions to produce different MTF curves. Modulation transfer properties can thus depend on the sample.

The definition of the MTF used here is the quantity which acts on the actual image, see also eq. (3.32). Measuring the MTF for an arbitrary test object does not always accurately determine the MTF curve acting on a different object.

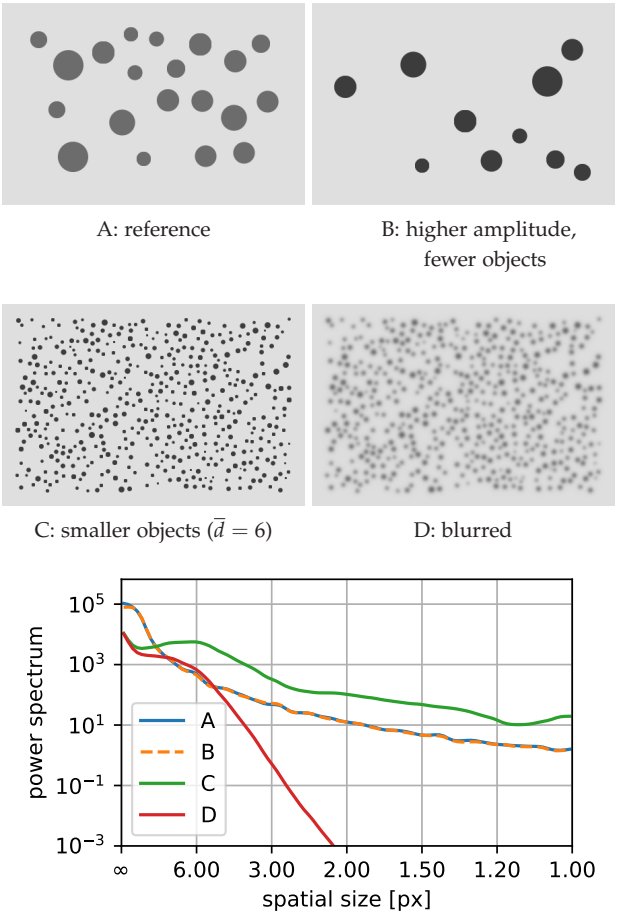

Figure 3.10.: Images (top) and corresponding power spectra (bottom) for different images. Cases A and B have the same (signal) power spectra, but B has a higher amplitude ($\cdot\sqrt{2}$) and fewer objects (half as many). Case C has smaller objects than A, which results in a power spectrum with a comparatively higher amount of signal in the higher spatial frequencies. Case D has been blurred, with a corresponding decrease of the power spectrum towards higher spatial frequencies.

Using MTF as a sample-independent quantity requires that an evaluation of the sample influence on the MTF curve is done. If this evaluation shows that there is no influence, then a sample-independent MTF is appropriate.

3.3.5. SNR spectra

The SNR spectrum is here defined as the fraction of the image signal power spectrum $S(u)$ to the image noise power spectrum $N(u)$, eq. (3.3). See section 3.1 for explanations on signal and noise power spectra. Due to the fact that it is based on power spectra, a SNR spectrum describes a kind of relative measurement error for structures of the size corresponding to u. The signal power spectrum is proportional to the square of the amplitude, and the noise power spectrum is equivalent to a variance (square of the standard deviation). This makes the SNR spectrum linear with respect to the detected intensity I:

$$SNR(u) \propto I \tag{3.23}$$

This linearity is a desirable property because it makes the SNR of measurements additive: Adding up K identically generated images results in a SNR spectrum which is a factor of K higher.

The aspect which produces the most difficulties in practice is the fact that the absolute scale of the SNR spectrum is given by both the amount of structure in an image and the amplitude scale, see fig. 3.10 for a visualization. As can be seen in the images A and B, the amplitude and number of objects are interchangeable influences. When a signal power spectrum or SNR spectrum of different objects and different measurement setups is compared, differences can therefore not be clearly attributed to one of the effects. Power spectra generally describe the statistics of the signal or noise: They are an average of the object shapes present in the image, but they reveal little about one individual shape.

SNR spectra of real images thus are mostly only useful on a relative scale. For comparisons between different circumstances, the same measured sample must be used to get accurate results. The absolute scale must be treated as somewhat arbitrary—it is not completely meaningless, but analyzing the absolute value should be avoided. If for example the test phantom shape contains very little structure, the SNR spectrum is artificially low. On the other hand, little signal means that the probability of false positive errors is much higher; a lower SNR spectrum may therefore also be a realistic description of the image quality.

In theoretical considerations, this is not an actual difficulty. A relative scale is completely sufficient there, because comparability can simply be achieved through the construction of the problem. Practical solutions for this problem are considered later, but often the aim of a SNR evaluation is to find an optimum. For this task, a relative scale is sufficient.

In any comparisons of SNR spectra of different measurement circumstances, one should therefore compare values at a specific spatial frequency (or range).

In this way, comparability is given, even if the absolute scale may be meaningless. When searching for an optimum, the sufficient information is the relative difference between different conditions.

This fact is the main reason why I propose to use SNR spectra in x-ray imaging: The relative difference derived from SNR spectra is a much more reliable indicator of image quality differences than e.g. DQE, CNR_{NDT} or a combination of SNR_t and MTF. While the fact that SNR spectra are a relative measure does pose the above mentioned difficulties, the relative differences have a high reliability.

In typical applications, image power spectra have certain shapes and some general rules can be derived. The most important is that signal power spectra of images are typically decreasing to higher spatial frequencies [39]. This is caused by two different effects: First, power spectra of image features larger than one pixel decrease towards higher frequencies, this can be seen from their Fourier transform. This decrease is faster the larger the object is. Second, the modulation transfer of the imaging setup (see section 2.2.1) typically causes a decrease of the signal amplitude towards higher frequencies.

Therefore, decreasing the whole SNR spectrum has the effect that the same SNR value is reached only for a coarser structure size u. Such a decrease may e.g. be caused by a reduction of the measurement time. Thus, a lower image quality or a shortened integration time usually has the consequence that the effective resolution for which reliable detection is possible becomes lower. If there is no coarse structure to be detected in an image, the fine structure there is simply can no longer be detected.

3.4. Image quality model

Deriving mathematical equations for SNR spectra allows to simulate and predict the influence of specific device parameters on the image quality. A better understanding of how different physical processes result in a specific image quality can be gained this way.

3.4.1. Photon classes

To simplify modeling (polychromatic) image superposition, I will first introduce a concept which reduces the complexity of the problem. Instead of superimposing every individual x-ray photon, some basic element is superimposed. I will call this basic element a "photon class", which is defined as the detected photons which have (approximately) the same properties relevant for image quality. Because some properties are irrelevant for image quality, the complexity of the model is reduced. A photon class has an intensity and this intensity needs to be considered for superposition (as a weight), but the individual photons need not be differentiated.

The definition of a photon class depends on the model used and its approximations. Here, I will use the following defining properties for a photon class, these are called "model parameters" in the following:

- Intensity $I(E)$
- Noise power spectrum $N(u, E)$
- Modulation transfer $\mathbf{h}(u, E)$ (MTF)
- Signal strength $\kappa(E)$ ($\kappa \propto$ contrast)

These depend on the following variables:

- Energy of the detected x-ray photon E
- Spatial frequency u
- Position z of the absorption event within the x-ray absorbing volume of the detector (along the beam)

Various underlying physical phenomena contribute to the actual values of the model parameters for a photon class. To compute these properties, one can use a monochromatic thin-screen model, where monochromatic x-rays and an arbitrarily thin x-ray absorbing screen (scintillator) in the detector are used. In general, computing the image quality for a photon class is easy, due to the fact that all photons have the same model parameters. The superposition of photon classes then yields the actual image and its image quality.

3.4.2. Local area approximation

The fundamental properties of an x-ray image vary over the sample area due to the fact that different x-ray spectra are transmitted through different sample thicknesses. To be able to model an actual value for the image quality measure, we therefore need to consider this problem locally: At a given sample thickness, what is the image quality? Because the sample thickness can vary spatially, an approximately constant sample thickness implies restricting the considered image area to a small area. I will call this the "local area approximation", because it considers the image quality in a local area of the image. The local area

therefore is an area that contains sample structure but where the weights (intensity) for the different photon classes are constant. Increasing the sample thickness preferentially absorbs specific photon classes and changes these weights. Examples for how this affects image quality were shown in fig. 3.1 on page 25.

As an additional simplification, I will consider only the single material case (κ independent of x). Considering multi material cases would not give new effects, but complicates the equations needlessly. In fact, an image quality evaluation will generally show different results and optima for different materials or contrasts if the energy-dependency curves are different.

To compute SNR spectra, signal and noise power spectra need to be derived. Splitting the signal into contributing factors is somewhat arbitrary, here the aim is that each factor represents an independent physical effect. For a local area, we can write for the (non-normalized) signal image $s(x,E)$ and the signal power spectrum of a photon class:

$$s(x,E) = I(E)\left[\kappa(E)\rho(x)\right] * h(x,E) \tag{3.24}$$

$$S(u,E) = P(u)\left[I(E)\kappa(E)\mathbf{h}(u,E)\right]^2 \tag{3.25}$$

These equations allow an analytical understanding of how a specific SNR spectrum/image quality emerges from the model parameters, if combined with a noise model. Note that in the second equation, **h** is assumed to be real positive.

Normally, ρ would be defined as the matter density of the sample. Here I define ρ as a normalized quantity ($\rho \in [0,1]$) which describes the fraction of material present in one voxel ("object shape"). The actual value is given by the local relative density of material, possibly averaged over a voxel. κ then gives the scale of the image. The material density is therefore part of the signal strength κ. With this definition, $P(u)$ is a quantity which only describes the shape of the object, I will call this quantity the "object spectrum".

The physical units of the quantities considered are not of importance for a theoretical consideration, especially as the SNR is a unit-free quantity. This is why simulated curves showing $SNR(u)$ in this work are usually given in arbitrary units—physical units were never considered in the simulation and the absolute scale is typically arbitrarily defined. When working with real measured data, considering the physical units is of course required.

Superposition of different photon classes in image space is a simple sum:

$$s(x) = \sum_E s(x,E) \tag{3.26}$$

where in this simple case, photon classes are only differentiated by x-ray energy. Because $\rho(x)$ and $P(u)$ are independent of the photon class, the corresponding signal power spectrum sum can be simplified to:

$$S(u) = \sum_E S(u,E) = P(u)\left|\sum_E I(E)\kappa(E)\mathbf{h}(u,E)\right|^2 \tag{3.27}$$

The square of the absolute value can usually be simplified to a square, when all terms in the sum are real-valued. $\kappa(E)$ can become negative for some specific material interfaces (e.g. Al-Si). The linear sum there can be interpreted as a spectral average of the signal strength multiplied by the MTF.

The noise power spectrum of a superposition can be written according to eq. (2.23) as:

$$N(u) = N_0(u) + \sum_E N(u,E) \tag{3.28}$$

where $N_0(u)$ gives contributions to image noise which are independent of detected x-ray photons. This is typically the detector readout noise and dark current noise. Note that dark current noise is proportional to the exposure time and therefore is normalized correctly when using a measurement time cost function. Significantly high readout noise will need to be considered when normalizing to exposure time. Scattered x-rays need to be included in $N(u,E)$, although they are not included in $S(u,E)$. Ideal detectors have only Poisson noise and

$$N_{\text{ideal}}(u,E) = I(E) \tag{3.29}$$

For indirect detectors see eq. (3.92).

The SNR spectrum of a photon class superposition is then:

$$SNR(u) = P(u)\frac{\left[\sum_E I(E)\kappa(E)\mathbf{h}(u,E)\right]^2}{N_0(u) + \sum_E N(u,E)} \tag{3.30}$$

3.4.3. Detection effectiveness

The object spectrum $P(u)$ is a global scaling factor for the SNR spectrum in the above equation, while the other variables are all physical properties of the imaging setup. $P(u)$ is the main factor that makes handling SNR spectra difficult in practice, because it is given by the object shape and strongly varies with u. Variations over several orders of magnitude are common. Here, object shape is meant to describe the structures

within an object. While the object shape is an important aspect for evaluating the detection properties of this specific object, the properties of the imaging device are independent of it. The object thickness does influence $I(E)$ and therefore the image quality.

We can differentiate two kinds of sample properties:

- Those which influence the model parameters and therefore also influence the properties of the imaging setup. The parameters they influence are the sample-dependent properties of the imaging setup.
- Those which neither influence the model parameters, nor the properties of the imaging setup. These are here called the properties of the sample itself.

The latter is completely modeled by the object shape/spectrum and all other model parameters are in the former category. If the signal strength is approximately independent of the x-ray energy, the influence of the sample on the sample-dependent properties is negligible.

For evaluating the performance of an imaging device, it is then useful to remove the object shape influence by normalizing SNR spectra with respect to the object spectrum. I will call this quantity the "detection effectiveness" $DE(u)$:

$$DE(u) = \frac{SNR(u)}{P(u)\eta} = \frac{\left[\sum_E I(E)\kappa(E)\mathbf{h}(u,E)\right]^2}{\left[N_0(u) + \sum_E N(u,E)\right]\eta} \quad (3.31)$$

The cost function η can be used to make measurements comparable. It can e.g. be defined as η = measurement time or η = dose. Note that the former must always be used if SNR measurements with different exposure times are compared. The $DE(u)$ is similar to the $CNR_{\mathrm{NDT}}(u)$ eq. (3.5), except where $DE(u)$ models polychromaticity (and other photon classes) fundamentally, $CNR_{\mathrm{NDT}}(u)$ only does so approximately (and implicitly). Also, the measurement procedures are completely different (see section 4.1.5).

The name part "effectiveness" in the $DE(u)$ is chosen to emphasize that this quantity is different from e.g. the DQE (detective quantum *efficiency*) in that it evaluates the actual overall performance. While an efficiency only describes one single influencing factor on the performance, an effectiveness describes the performance itself. Efficiencies are typically used in device standardization. It is always more reliable to optimize an effectiveness instead of an efficiency—optimizing one part of the setup may reduce the overall performance in complex (physical) situations.

3.4.4. Effective model parameters

Averaged model parameters as they act on the measured image are here called *effective* model parameters. Due to the fact that signal and noise have different superposition rules, the corresponding effective parameters are different. Here, only signal effective model parameters are considered. Ideal noise according to eq. (3.29) does not have model parameters, as its polychromatic sum is simply a sum over the intensity. For indirect detector noise (e.g. eq. (3.92)), effective model parameters can be derived. The values of the noise effective model parameters are then different from the signal effective parameters (e.g. for c).

For the signal, effective parameters can be computed by normalizing the sum in eq. (3.27) by the sum over the weight that acts on the quantity of interest:

$$\mathbf{h}_{\mathrm{eff,S}}(u) = \frac{\sum_E I(E)\kappa(E)\mathbf{h}(u,E)}{\sum_E I(E)\kappa(E)} \quad (3.32)$$

$$\kappa_{\mathrm{eff,S}}(u) = \frac{\sum_E I(E)\kappa(E)\mathbf{h}(u,E)}{\sum_E I(E)\mathbf{h}(u,E)} \quad (3.33)$$

For the intensity, no effective quantity exists, as the intensity is the weight function. The normalization required to derive an effective intensity is impossible as $\sum_E \kappa(E)\mathbf{h}(u,E)$ is arbitrarily large.

The dependency of $\kappa_{\mathrm{eff,S}}$ on the spatial frequency is caused by the energy-dependency in both the MTF and $\kappa_{\mathrm{eff,S}}$ or I. If e.g. the MTF is much better at higher x-ray energies, κ for fine details will be produced preferentially by higher-energy x-rays. For coarser details, lower energy x-rays then play a more important role. As there is no effective intensity, a product of effective quantities does not give $S(u)$. Instead we get:

$$S(u) = P(u)\mathbf{h}_{\mathrm{eff,S}}(u,I,\kappa)\sum_E I(E)\kappa(E) \quad (3.34)$$

$$S(u) = P(u)\kappa_{\mathrm{eff,S}}(u,I,\mathbf{h})\sum_E I(E)\mathbf{h}(u,E) \quad (3.35)$$

Here, the functional dependencies of the effective quantities are stated explicitly. Even though here the different photon classes are mainly used to describe polychromatic effects, they can in principle be used in any case where x-ray photons have different properties. For example extending the model to include the parameter z can be done by extending eq. (3.31). (z is the position within the absorbing screen along the beam direction.)

For this example, a point source is assumed ($\mathbf{h}_{\text{source}} = 1$), which means that only the detector MTF is considered. For an indirect detector, $\mathbf{h}$ is not energy-dependent itself, because the blurring affects the secondary photons (see section 3.7). The strength of this blurring depends on the distance to the focus plane (defect of focus) for lens-based detectors and on the distance to the fiber plate for flat-panel detectors. Both distances are determined uniquely by z. The x-ray intensity detected within a screen volume per energy is given by the Lambert-Beer law eq. (2.3): $I(E,z) \propto e^{-\mu(E)z}$. Note that here, z is not the thickness of the screen which the x-rays passed through. Instead, it is a variable with a constant offset to the latter value. Therefore we get:

$$DE(u) = \frac{\left[\sum_E \sum_z I(E,z)\kappa(E)\mathbf{h}(u,z)\right]^2}{\left[N_0(u) + \sum_E \sum_z N(u,E,z)\right]\eta} \tag{3.36}$$

We can compute an effective MTF that is independent of z as:

$$\mathbf{h}_{\text{eff},S\backslash z}(u,E) = \frac{\sum_z I(E,z)\mathbf{h}(u,z)}{\sum_z I(E,z)} \tag{3.37}$$

Because both intensity and MTF depend on z, the effective MTF is energy-dependent even if the MTF for a single photon class is not. Consequently, the MTF is then also sample-dependent. Generally, dependencies of effective model parameters on variables may not only result from a direct dependence. They may also result from a common dependency on another model parameter (here: z).

An objects' signal strength $\kappa(E)$ and its influence (via transparency) on $I(E)$ weights the device properties and determines the effective device properties. The effective quantities are therefore always application-specific while the device properties for a single photon class are not. In some cases, the effective quantities may be approximately application-independent. But in general, fundamental device properties can only be defined for a given photon class. Examples:

1. MTF, the property of the device is the set of MTF curves $\mathbf{h}_{\text{eff},S\backslash z}(u,E)$.
2. Absorption efficiency of the detector a, the device property is $a(E)$ ($I(E) \propto a(E)$).

For the latter, an effective quantity can be defined by separating the intensity as $I(E,z) = a(E)I_{\backslash a}(E,z)$ as:

$$a(u) = \frac{\sum_E \sum_z a(E)I_{\backslash a}(E,z)\kappa(E)\mathbf{h}(u,z)}{\sum_E \sum_z I_{\backslash a}(E,z)\kappa(E)\mathbf{h}(u,z)} \tag{3.38}$$

3.4.5. SNR spectra of superpositions

By using the local area model for image quality, eq. (3.30), we can analyze how the superposition of different photon classes affects the resulting SNR. For this consideration, the measured x-ray image is conceptually separated into individual images with different photon classes. In general, superimposing two images results in an SNR which is less or equal to the sum of the individual SNR contributions. The simplest case is the superposition of two images (image 1 and 2). Due to the fact that the numerator of the SNR contains a square norm, see eq. (3.30), the following triangle inequality holds:

$$SNR_{1+2}(u) \leq SNR_1(u) + SNR_2(u) \tag{3.39}$$

This equation does allow $SNR_{1+2}(u) < SNR_1(u)$ to be the case. That would mean that the additional photons (image 2) which are added to the reference situation (image 1) reduce the overall SNR. Preventing this requires that the following condition is met:

$$SNR_{1+2}(u) > SNR_1(u) \tag{3.40}$$

$$\Leftrightarrow \frac{\left[I_1\kappa_1\mathbf{h}_1 + I_2\kappa_2\mathbf{h}_2\right]^2}{N_0 + N_1 + N_2} > \frac{\left[I_1\kappa_1\mathbf{h}_1\right]^2}{N_0 + N_1} \tag{3.41}$$

$$\Leftrightarrow \frac{I_1\kappa_1\mathbf{h}_1 + I_2\kappa_2\mathbf{h}_2}{I_1\kappa_1\mathbf{h}_1} > \sqrt{\frac{N_0 + N_1 + N_2}{N_0 + N_1}} \tag{3.42}$$

$$\Leftrightarrow \frac{I_2\kappa_2\mathbf{h}_2}{I_1\kappa_1\mathbf{h}_1} > \sqrt{1 + \frac{N_2}{N_0 + N_1}} - 1 \tag{3.43}$$

Therefore, while the absolute signal strengths are not important for an SNR optimization, the relative strengths are.

For an $N_2 \ll N_1$ (infinitely small addition), we can approximate the square root above:

$$\frac{I_2\kappa_2\mathbf{h}_2}{N_2} > \frac{1}{2}\frac{I_1\kappa_1\mathbf{h}_1}{N_1 + N_0} \tag{3.44}$$

This is an interesting limit case, but it has no practical applications. The quantity on the left is called "signal detection strength" (SDS) in the following:

$$SDS(u,E) = \frac{I(E)\kappa(E)\mathbf{h}(u,E)}{N(u,E)} \tag{3.45}$$

This quantity be calculated either for a single photon class or for a set of photon classes $\{E\}$:

$$SDS(u,\{E\}) = \frac{\sum_{\{E\}} I(E)\kappa(E)\mathbf{h}(u,E)}{\sum_{\{E\}} N(u,E)} \tag{3.46}$$

For $N_0 \ll N_1$ we can rewrite eq. (3.44) to:

$$SDS_2(u,E) > \frac{1}{2}SDS_1(u,E) \tag{3.47}$$

Thus, a small intensity addition requires at least half the *SDS* of the existing image to contribute positively. This is an upper bound for this minimum, larger intensity additions always require less than half the *SDS*. For a large intensity addition ($I_2 \gg I_1$), $SNR_{1+2} > SNR_1$ is always true. If N, $\mathbf{h}$ and I are equal for both images, the condition becomes $\kappa_2 > 0.41\kappa_1$. Note that for dose-limited imaging, the prior derivation would need to be done on a $DE(u)$ with $\eta =$ dose, with different results.

The *SDS* for an ideal detector can be simplified using eq. (3.29) to:

$$SDS_{\text{ideal}}(u,E) = \kappa(E)\mathbf{h}(u,E) \tag{3.48}$$

3.4.6. Energy weighting

The effect that the image quality can be increased by weighting an image with an energy-dependent factor has first been proposed by [29] and a more recent application is e.g. [40]. I will differentiate two variants of this effect. The physical origins of both are fundamentally different, but they have similar effects:

- Application of an energy-dependent weighting after the detection of the x-ray photons. This is what was proposed in [29] and this is usually discussed as energy weighting. Because sufficiently good energy-resolving 2D imaging detectors are currently not technically feasible, this is mostly a theoretical concept.
  I will call this effect "computational energy weighting" (CEW).
  A CEW weight w scales *SDS* with $1/w$.
- Implicit weighting by the detected intensities $I(E)$ (effective x-ray spectrum). This is influenced by the generated, transmitted and detected x-ray photon spectra. Can be changed by purposefully decreasing the detected intensity in specific energy ranges.
  I will call this effect "detection energy weighting" (DEW).

The fact that energy weighting as an effect exists and could be used in energy-resolving detectors (CEW) has been published [36, 37]. There appear to be no quantitative descriptions for DEW.

The energy weighting effect ($\propto E$) of an energy integrating detector has already been formulated in 1973 by Swank [41]. At that point in time, the noise properties of indirect detectors were not yet formulated quantitatively (see section 3.7 on page 51). The secondary photon noise, the interaction of secondary modulation transfer and conversion efficiency, and the fact that the SNR is influenced by the relative signal strength are missing from the equations. The derived formulae of this work are still used today as the "Swank factor" (see e.g. [42]), but their usefulness is limited. What that work does describe correctly is the fact that when superimposing noisy images with identical properties, weighting the contributions differently decreases the SNR.

Optimizing a weighting (CEW or DEW) can lead to an increase in *SNR*. The potential increases are between a few percent and factors > 10, depending on the experimental conditions. Applying an energy weighting can make broad x-ray spectra useful, and the larger effect sizes are for these spectra.

For the CEW, multiplying with a weight $w(u,E)$, results in:

$$SNR_{\text{CEW}}(u,w) = \mathrm{P(u)}\frac{\left[\sum w(u,E)I(E)\kappa(E)\mathbf{h}(u,E)\right]^2}{\sum w(u,E)^2 N(u,E)} \tag{3.49}$$

The optimal energy weighting function $w_{\text{opt.}}$ for CEW can be determined by finding the maximum of the *SNR* spectrum depending on $w(u,E)$:

$$\frac{\mathrm{d}SNR_{\text{CEW}}(u,w)}{\mathrm{d}w} \stackrel{!}{=} 0 \tag{3.50}$$

which is solved by any CEW weight proportional to

$$w_{\text{opt.}}(u,E) \propto \frac{I(E)\kappa(E)\mathbf{h}(u,E)}{N(u,E)} = SDS(u,E) \tag{3.51}$$

This result is an extension of the known result $w_{\text{opt.}}(u,E) \propto \kappa(E)$ [29]. In addition to κ, the MTF and the relative noisiness of the photon class are here included. Similar to eq. (3.36), $w_{\text{opt.}}$ can in theory be extended to $w_{\text{opt.}}(u,E,z)$. For a detector with a limited energy resolution, eq. (3.46) can be used. In that case, the thresholds between energy bins need to be chosen carefully, especially if only two or three energy bins are available.

The inclusion of the MTF in the energy weighting equation means that this method would also introduce something which could be called frequency weighting. As a purely theoretical consideration, a lens-based detector using ideal frequency weighting could use an arbitrarily thick screen without decreasing its effective MTF. The additional blurred intensity of the scintillator volume farther from the focus plane would simply be frequency weighted, and it would therefore

no longer decrease the effective resolution. It would still increase the SNR for coarser structures, resulting in a detector whose optimal resolution range is very broad.

Note that the *SNR* spectrum is not changed when a Fourier filter is applied, but the image may be easier or more difficult to interpret. To avoid artificial image blurring while applying a CEW, it is therefore sufficient to only apply a relative blurring factor in this way:

$$w_{\text{opt.}}(u,E) = \frac{I(E)\kappa(E)\mathbf{h}(u,E)}{N(u,E)\mathbf{h}_0(u)} \tag{3.52}$$

where $\mathbf{h}_0(u)$ can e.g. be the energy-averaged MTF.

After application of the optimal CEW, the signal detection strength *SDS* is constant with respect to E:

$$SDS_{\text{opt. CEW}}(u,E) = \text{const}(E) \tag{3.53}$$

The special case of a task-independent (t.i.) measurement case is defined as a case with energy independent signal detection strength (without weighting):

$$SDS_{\text{t.i.}}(u,E) \approx \text{const}(E) \tag{3.54}$$

$$\Rightarrow w_{\text{opt|t.i.}}(u,E) \approx \text{const}(E) \tag{3.55}$$

$$\Rightarrow SNR_{\Sigma|\text{t.i.}}(u) \approx \sum_E SNR_{\text{t.i.}}(u,E) \tag{3.56}$$

Task-independency is often (implicitly) assumed when x-ray image quality is optimized. Many intuitive assumptions about this topic are therefore based on this simple case and are wrong for more complex cases. In some special cases, e.g. monochromatic imaging, task-independency is a correct assumption. For x-ray imaging where Compton scattering is the main interaction (e.g. Al above 60 keV), task-independency can be approximately correct.

By comparing eq. (3.53) and eq. (3.54), we see that applying an optimal CEW has the effect that the result appears to be task-independent ($SDS = \text{const}(E)$). The CEW itself is of course task-dependent. This also means that task-independency is the case in which there is an optimal superposition of the *SNR* contributions (SNR is additive).

The optimal DEW appears to have no analytical expression. It is thus the case with the maximal *SNR*. Equation (3.43) can be used to find changes in the experimental setup which may increase *SNR*. In general, if the x-ray photons at a specific energy range decrease *SNR*, a reduction of the corresponding intensity increases *SNR*.

An example for the different energy weightings is shown in fig. 3.11, with attenuation in Al as the signal

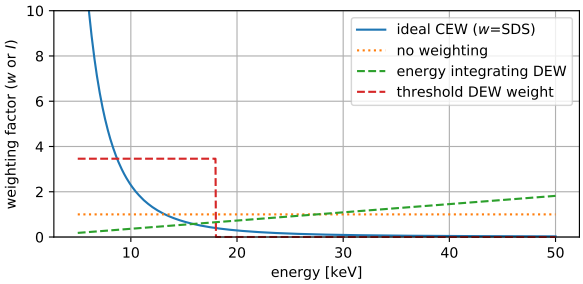

Figure 3.11.: Different energy weigth functions for attenuation in Al. The ideal CEW curve is $\approx E^{-3}$ for the energy range shown.

generating effect. It can be seen that here the optimal weightings all prefer the part of the x-ray spectrum where κ is higher (here: lower energies).

Considering the DEW threshold gives an interesting insight into which x-ray photons are actually contributing to the image. Only the photons below the DEW threshold contribute positively to the image quality and thus only these photons matter for the signal properties of the image. Thus, for example MTF and signal strength really only matter in this energy range. For the noise properties, the whole detected spectrum is relevant.

3.4.7. Monochromatic scaling laws

Based on the analytical expression for the SNR spectrum in eq. (3.30), the scaling laws for image quality can be derived. Simple relationships can be derived only for monochromatic x-ray spectra, although splitting model parameters into an energy-dependency and an energy-independent scaling factor can also show how energy-independent changes affect polychromatic imaging. For example for the intensity, we can arbitrarily define:

$$I(E) = I_C I_E(E) \tag{3.57}$$

For monochromatic imaging, we would simply set $I_E(E) = 1 \Rightarrow I(E) = I_C$. This split therefore automatically also gives the relationships for monochromatic imaging. Additionally, we need to assume that $N(E) \propto I_C$, which means that N_0 needs to be small. The other forms of noise are typically proportional to the intensity (Poisson noise). Then

$$SNR(u) \propto I_C \tag{3.58}$$

Similarly

$$\kappa(E) = \kappa_C \kappa_E(E) \tag{3.59}$$
$$\Rightarrow SNR(u) \propto \kappa_C^2 \tag{3.60}$$

And for the MTF

$$\mathbf{h}(u, E) = \mathbf{h}_C(u)\mathbf{h}_E(u, E) \tag{3.61}$$
$$\Rightarrow SNR(u) \propto \mathbf{h}_C(u)^2 \tag{3.62}$$

For direct detectors, noise is simple ($N = I$) and therefore no additional monochromatic scaling laws apply. For indirect detectors, part of the MTF also affects noise, so both noise and detector MTF have a complicated relationship to SNR.

The most important aspect of these equations is that SNR scales linearly with intensity but squarely with signal strength or MTF. When using temporal SNR, linearly/squarely translate to square root/linearly; the difference is the same. This fact needs to be taken into account when optimizing an x-ray imaging device—improving the MTF by a factor of 2 is equivalent to improving the intensity by a factor of 4.

3.5. Analytical simulations

3.5.1. Simple models

As a basis for the analytical simulations, I will introduce some simple models for x-ray source, sample and detector. They are here used to demonstrate in general which physical effects are possible and roughly approximate real applications. This approach was chosen because (1) these simulations are easy to interpret and causal relationships can be clearly identified (2) real applications are too diverse so there is not really something like a "representative case".

X-Ray source

The simplest possible x-ray source for approximating laboratory applications is one emitting only bremsstrahlung, which is here used as a general polychromatic source. Such a spectrum has the following intensity for a given acceleration voltage U_t of the x-ray tube:

$$I(E) \begin{cases} = bC_t(E - U_t) & \text{for } 0 < E < U_t \\ = 0 & \text{else} \end{cases} \tag{3.63}$$

where C_t is the tube current (target current) and b is an arbitrary scaling factor that needs to be kept constant within one set of compared simulations. Real x-ray tubes can only deliver a limited tube current, which may depend on the tube voltage. If the generator for the tube voltage is able to supply arbitrary high currents, the heat load of the target becomes limiting, in which case $C_t \propto 1/U_t$.

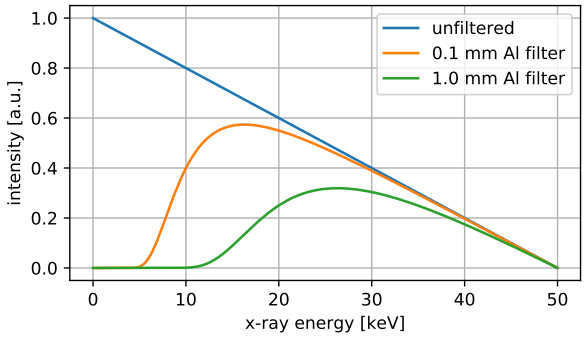

Figure 3.12.: Computed bremsstrahlung spectra without filters (unrealistic source) and with attenuation in matter (filter or sample). Except for emission lines, such spectra are good approximations for generalized real spectra. The tube voltage is here 50 keV.

Due to the fact that the lower x-ray energies are absorbed by various objects in the beam, the pure bremsstrahlung spectrum is unrealistic at this energy ranges. If the sample is a much stronger absorber than the sum of the other absorbers (target, tube window, air, ...), then simulating the sample attenuation is sufficient to get a realistic x-ray spectrum. A simple x-ray spectrum is shown in fig. 3.12, where the unrealistic bremsstrahlung spectrum and more realistic spectra after transmission through a sample are shown.

Emission lines can easily be simulated, but the energy and intensity of these depends on the target material. A realistic source would consist of a sum of such simple sources, because different emission points for the x-rays have different attenuation geometries.

Sample

The sample has two effects on the x-ray image quality: First, the sample reduces the detected intensity I due to the energy-dependent transparency. Second, the signal strength κ of the image generating effect is also given by the sample properties.

The sample transparency T for a given attenuation cross section μ_{abs} and a sample thickness t is given by

the Lambert-Beer law:

$$T(E) = \exp(-t\mu_{\text{abs}}(E)) \tag{3.64}$$

For a given sample thickness, higher attenuation cross section thus lead to a lower detected intensity. Therefore, the energy-dependency in the x-ray intensity depends on the energy-dependent attenuation properties of the sample. This fact also results in an effect called "beam hardening", where a lower cross section at higher x-ray energies means that the sample is more transparent for higher energies. The detected x-ray spectrum therefore depends on the sample thickness and the SNR of thicker samples is typically (much) lower. See section 4.2.5 for corresponding SNR measurements.

X-ray filters act on the SNR as an additional sample thickness. If they are of the same material, they thus always reduce SNR. Using an x-ray filter whose absorption edges match with energy ranges where a lower DEW weight would be beneficial can increase SNR. For computing the sample transparency, absorbing matter must be differentiated into sample and filter. Otherwise, filter and sample need not be differentiated for a SNR optimization.

The signal strength κ may either be identical with the attenuation cross section (attenuation imaging), or depends on the sample phase shift for phase imaging.

Detector

Simple models for x-ray detectors need to differentiate between direct and indirect detectors (see section 3.3.3). Both types of detector behave similar with respect to the effect of x-ray attenuation: The detection of a x-ray photon is only possible if it somehow interacts with the detector materials. This effect is modeled by the attenuation efficiency, and for simplicity attenuation efficiency is here approximated by the photo-absorption cross-section. Detector absorber materials usually have a high atomic number, so this approximation is good for x-ray energies typically below 150 keV (dependent on detector material, see fig. 3.2). Effects from absorption edges are not modeled here.

The absorption efficiency $a(E)$ is also given by the Lambert-Beer law, except that not the transmitted but the absorbed photons are of interest:

$$a(E) = 1 - \exp(-t\mu_{\text{abs}}(E)) \tag{3.65}$$

For simplicity, and to not be dependent on the absorption edges of a specific detector material, the photoabsorption cross section is approximated as $\propto E^{-3}$. This allows the following approximation:

$$a(E) \approx 1 - \exp(-t_{\text{abs}}E^{-3}) \tag{3.66}$$

where t_{abs} is an attenuation thickness which includes material properties, but is independent of the x-ray energy. Typical detector materials have absorption edges in the energy range used for imaging, so in a specific case such an edge may have a significant influence on the image quality optimization.

The idealized detectors thus decrease the detected intensity. In the case of the idealized direct detector, this is all that is done to simulate such a detector – which assumes a detection process that does not add noise. Direct detectors with significant charge sharing violate this assumption, see e.g. [43]. For the indirect detector the additional noise according to eq. (3.92) needs to be considered. To simplify the simulation, $c \gg 1$ (efficient conversion) is assumed, otherwise the detector MTF would need to be known even for a simulation where modulation transfer effects are not modeled.

Modulation transfer

The modulation transfer that affects the image quality is the system MTF, where the different influences of source, detector and geometry are combined (all within the LTI approximation).

A good simple model for various MTFs in x-ray imaging is the Voigt profile, which stems from the combination of a Gaussian and a Lorentz PSF. The corresponding Voigt MTF is the product of the two corresponding MTFs (see table 2.1)

$$\begin{aligned}\mathbf{h}(u) &= \exp\left(-2\pi u^2\sigma^2\right)\exp\left(-2\pi u\mu\right) &(3.67)\\ &= \exp\left(-2\pi\left[u^2\sigma^2 + u\mu\right]\right) &(3.68)\end{aligned}$$

A source MTF $\mathbf{h}_{\text{src}}$ and a detector MTF $\mathbf{h}_{\text{det}}$ combine to a system MTF $\mathbf{h}$ on a setup with a x-ray magnification M. The Voigt MTF is often ab bad fit for real MTFs on the lower spatial frequencies, if e.g. the detector has long-range blurring.

By scaling the spatial frequency coordinates (u in sample space/voxel coordinates), we can compute the system MTF as:

$$\mathbf{h}(u) = \mathbf{h}_{\text{src}}\left(u\frac{M-1}{M}\right)\mathbf{h}_{\text{det}}\left(u\frac{1}{M}\right) \tag{3.69}$$

Note that if a scaling factor becomes smaller, the influence of the corresponding MTF on the system

MTF becomes weaker. This is due to the fact that at lower u, the MTF is typically larger and $\mathbf{h}(u) \to 1$ for $u \to 0$. Therefore, for $M \to 1$ (sample near detector) the source MTF becomes unimportant and for $M \to \infty$ (sample near source) the detector MTF becomes unimportant.

The following simulations always (implicitly) consider the SNR for a specific spatial frequency, as this is how it would need to be done on real measurements. Additionally, plotting SNR spectra at constant u makes the SNR curves much easier to read and interpret. This simplification appears to neglect modulation transfer, but that is not the case. For real applications, modulation transfer needs to be included, as one can not simply set the MTF to be constant for different conditions.

Neglected aspects

In a real setup, several other influences may appear. These are not modeled in the simple analytical simulations. Some examples for such effects are:

- Detector noise: Thermal noise (dark current) and readout noise are produced in the detector electronics. The former is Poisson noise and its NPS is proportional to the exposure time, while the latter is independent of it. Scientific cameras use cooling and high quality readout electronics to reduce this noise to small values. Flat panel detectors not damaged by radiation typically also have low detector noise.
  Effect: Additional noise to N_0.
- X-ray scattering: Scattered radiation either from the sample or detector or from some material in the vicinity of the x-ray source (e.g. radiation shielding, granite base) may be detected.
  Effect: Additional noise to $N(u, E)$.

3.5.2. Different energy weightings

To demonstrate how the energy weighting effects actually work, very simple examples with different (non-)optimal energy weightings are computed. Due to the simplicity of the example, the basic principles of the energy weightings can be understood.

As the simplest possible example for *SNR* spectra of an image superposition, two monochromatic images are added:

$$d_{1+2}(E) = d_1\delta(E - E_1) + d_2\delta(E - E_2) \tag{3.70}$$

description	κ_2	SNR_2	SNR_{1+2}
a) photoabsorption	0.14	0.020	0.65
b) phase contrast	0.25	0.063	0.78
c) no gain, eq. (3.43)	0.41	0.17	1
d) task-independent	1	1	2
e) optimal CEW for a)	0.14	1	1.02
f) optimal DEW for a)	0.14	1	1

Table 3.2.: Examples for the $SNR(u_a)$ of image sums for different physical effects represented by κ with κ_1 = 1 and SNR_1 = 1. Cases a) and b) are e.g. iron for 30 keV and 60 keV. Note that for a) to d), the fraction of detected photons ($\propto$ polychromatic *DQE*) is twice as high for the sum image, but for a) and b) the image quality is lower. See section 3.4.6 for cases e)+f).

The following conditions are assumed:

$$P(u_a)H_1(u_a)^2 = P(u_a)H_2(u_a)^2 = 1; \tag{3.71}$$

$$I_1 = I_2 = 1; \quad E_1/E_2 = 0.5 \tag{3.72}$$

for a structure size of u_a. This effectively excludes modulation transfer effects from our examples—this can be done in a theoretic model without loss of generality,[4] but would be almost useless for a real application. Additionally, an ideal photon counting detector ($N_k = I_k$) is assumed.

This is a realistically polychromatic case whose effect sizes approximate real cases. Inserting all these values into equations (2.23) and (3.27) yields:

$$N_1(u_a) = I_1; \quad N_2(u_a) = I_2 \tag{3.73}$$

$$S_1(u_a) = (I_1\kappa_1)^2; \quad S_2(u_a) = (I_2\kappa_2)^2 \tag{3.74}$$

$$N_{1+2}(u_a) = I_1 + I_2 \tag{3.75}$$

$$S_{1+2}(u_a) = (I_1\kappa_1 + I_2\kappa_2)^2 \tag{3.76}$$

Using the specific values listed above gives for the SNR:

$$SNR_1 = SNR_1(u_a) = 1 \tag{3.77}$$

$$SNR_2 = {\kappa_2}^2 \tag{3.78}$$

$$SNR_{1+2} = \frac{(1+\kappa_2)^2}{2} \tag{3.79}$$

Some examples of the *SNR* values for different κ_2 are computed in table 3.2. From these examples we can see that the additionally detected intensity I_2 may reduce the overall image quality significantly if the SNR_2 of this additional intensity is low compared to

[4] Including $H(u_a)$ as a factor in κ restores the full properties.

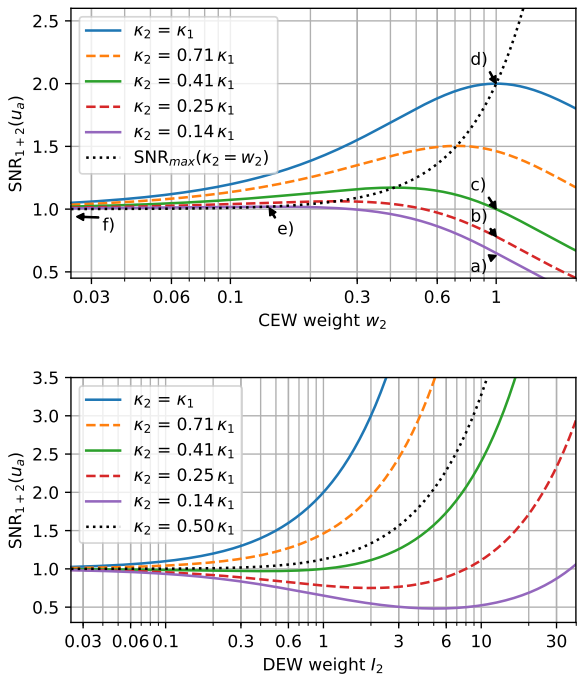

Figure 3.13.: Examples for the dependency of the *SNR* on the weighting factor for CEW (top) and DEW (bottom). The weighting factor factor of image 2 is w_2. The annotations correspond to table 3.2. For DEW, the maximal *SNR* is either at $I_2 = 0$ or at finite I_2, depending on the maximal value of I_2. The edge case $\kappa_2 = 0.5\kappa_1$ is the lowest possible κ_2 where $SNR_{1+2} \geq SNR_1$ for all I_2.

the SNR_1 of I_1. In real examples, a difference in a MTF may also produce this effect.

The reason for this behavior is easily explained by the fact that if $\kappa_1^2 \gg \kappa_2^2$, I_2 contributes little signal but all of its noise to the image sum. A lower detected intensity at E_2 would decrease that noise.

Here, a high enough intensity can compensate for a low signal strength in the following way:

$$SNR_{1+2} \geq SNR_1 \Leftrightarrow I_2 \geq I_1 \frac{1 - 2\kappa_2}{{\kappa_2}^2} \tag{3.80}$$

This simple example allows us to evaluate the effect (non-optimal) energy weighting has on the *SNR*, which is shown in fig. 3.13 for CEW and DEW. The examples only qualitatively represent realistic cases, but demonstrate the effects which different energy weightings have on *SNR*.

We can see that for CEW, there is always a unique maximum at $w_2 = \kappa_2$. For DEW, there is a unique minimum, while one maximum is obtained for $I_2 \to \infty$. An additional local maximum exists at $I_2 = 0$ for $\kappa_2 < \kappa_1/2$. If we assume that a maximal value for I_2 is given by the physical circumstances (e.g. source spectrum), the optimal weighting is either to use this maximal value or use $I_2 = 0$ (depending on κ_2). The optimal DEW weight can thus be interpreted as a mask function that is either 0 or 1. For typical κ curves that decrease towards higher energies, it is usually a step function that is 1 at low energies and 0 above some threshold. While the corresponding values for real applications differs, the general laws stay the same.

3.5.3. Source spectrum influence

Results of *SNR* simulations for simple x-ray spectra are shown in fig. 3.14. They are generated by analytically computing $SNR(u)$, using eq. (3.30) and the models explained in section 3.5.1. Both examples use the same source spectra, detector and sample, but different energy-dependencies of the signal strength. These examples demonstrate the magnitude of the effect different energy weighting effects have on *SNR*, they are not meant to describe an actual setup. See fig. 3.2 for the attenuation coefficient for aluminium (Al), which gives the energy-dependent sample transparency (0.1 mm thickness) and the signal strength for the attenuation signal (approximately $\kappa(E) \propto E^{-3}$). The x-ray inline phase contrast signal strength is assumed to be $\kappa(E) \propto E^{-2}$ [8].

An ideally absorbing detector is used and the source is assumed to have constant target power (product of tube voltage and current is constant). Constant power means that the actual source would be limited by the thermal capacity of the target material, not by the maximum current of the generator for the tube voltage. Its spectrum is a bremsstrahlung spectrum given by Kramers' law, eq. (3.63), which is sufficient as a rough approximation. Higher tube voltages correspond to a higher degree of polychromaticity, because the sample is the same.

To produce plots that are easy to interpret, the *SNR* spectrum is again evaluated at a specific spatial frequency u_a and the MTF is assumed to be energy-independent. Applications in real world examples must avoid this kind of simplification.

The monochromatic *SNR* curve is from the optimal monochromatic x-ray spectrum (at 6.1 keV for attenuation and 7.0 keV for phase contrast) with the intensity given by the sum over the corresponding bremsstrahlung spectra. The optimal CEW curve uses the signal strength as the weight. The optimal DEW

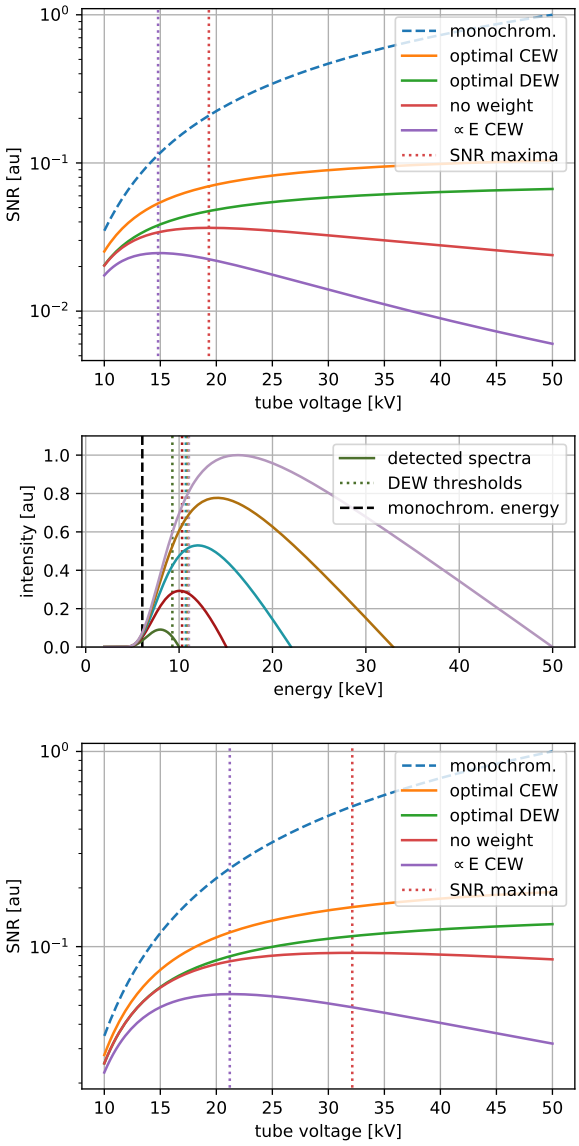

Figure 3.14.: Simulated (photo-)absorption $SNR(u_a)$ (top) and x-ray inline phase contrast $SNR(u_a)$ (bottom) curves for a bremsstrahlung source with constant source power. The corresponding detected x-ray spectra are shown in the middle, where the highest energy in a curve is the tube voltage.

curve only includes photons below the optimal threshold, shown as vertical dashed lines in fig. 3.14 (middle). The "$\propto E$ CEW" is the energy integrating indirect detector case ($w \propto E$) and assumes efficient conversion (see eq. (3.21), $c^2 H_v^2 \gg c$). Note that the curve for monochromatic SNR is not strictly comparable to the other because its intensity is somewhat arbitrarily defined. To get realistic monochromatic intensities, $\frac{1}{3}$ of the sample thickness is counted as a x-ray filter.

Both for photoabsorption and phase contrast signals, only the lower energy x-ray photons have a sufficiently high *SDS* to contribute positively to the *SNR*. This effect is weaker for phase contrast due to a weaker energy dependency. In this example, the *SNR* curves are always ordered: $\propto E$ CEW $<$ no weight $\leq$ optimal DEW $<$ optimal CEW $<$ monochromatic. The differences get larger for broader x-ray spectra.

Direct detectors ("no weight") here have an intrinsically higher image quality than indirect detectors ("$\propto E$ CEW") and this benefit is larger for higher degrees of polychromaticity. This difference is caused solely by the different energy weighting, as both detectors are otherwise assumed to be perfect absorbers and without additional noise.

It can be seen that weighting down (CEW) or not detecting (DEW) specific photons can increase *SNR* by large factors. Note that the monochromatic *SNR* is directly proportional to the cumulative intensity of the source spectrum.

The following simple rules for energy weighting can be seen in fig. 3.14: For optimal CEW, every additional photon increases *SNR*. For optimal DEW no additional photon decreases *SNR*. For all other weightings, additional photons can decrease or increase *SNR*.

If we use this example for a *SNR* optimization, we can see that very low tube voltages would be optimal if CEW or DEW cannot be implemented. For thicker samples, higher tube voltages would be optimal than for this example of a thin sample. See section 4.2.5 for corresponding measurements on a real setup.

We could use the optimal CEW case as SNR_{ideal} in eq. (3.19) and the $\propto E$ CEW as SNR_{detected} to compute an accurate polychromatic *DQE* for an indirect detector with ideal absorption and efficient conversion. It has $DQE \ll 1$ for broad spectra due to its energy weighting. Computing a polychromatically averaged *DQE* using eq. (3.20) without consideration of the signal strengths would give $DQE = 1$ due to the fact that an ideally absorbing detector was simulated.

In real applications, samples usually have varying thicknesses and a setup must be optimized to give high *SNR* at a combination of thicknesses.

3.5.4. Detector thickness influence

$SNR(u_a)$ curves for different thicknesses t of a x-ray absorbing screen (e.g. scintillator) are shown in fig. 3.15. The screen is approximated as an idealized photoabsorber with an attenuation constant $\propto E^{-3}$ (no absorption edges). All other properties and the sample

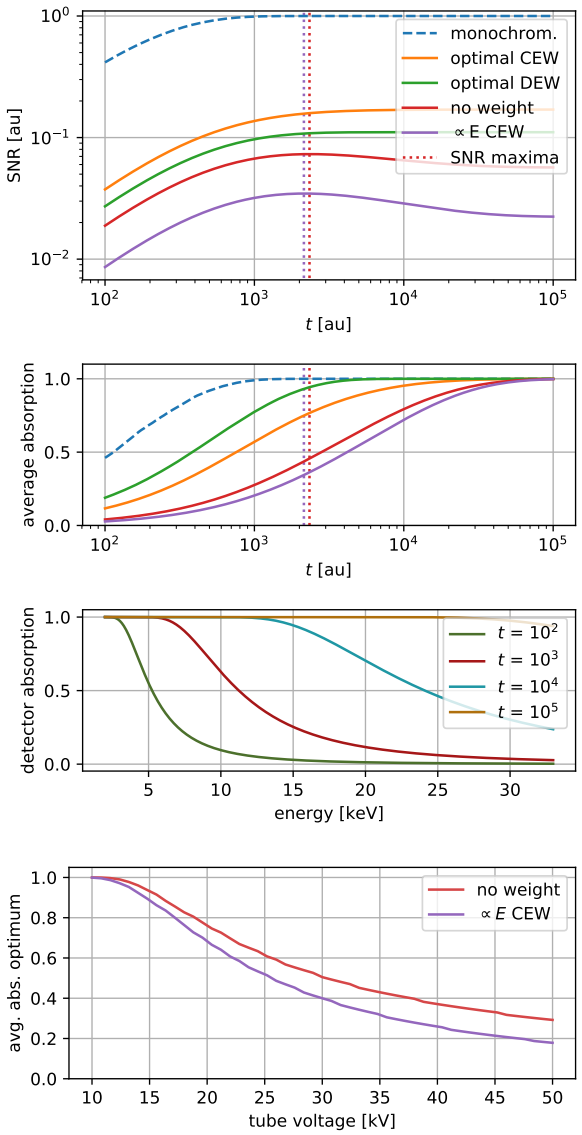

Figure 3.15.: Simulated (photo-)absorption $SNR(u_a)$ curves for different photoabsorber screen thicknesses t (top). Corresponding values for the weighted absorption average (upper middle) and energy-dependent absorption efficiency (lower middle). The average detector x-ray absorption for the t with the maximal SNR is shown for different tube voltages (bottom).

are the same as above and a source spectrum with a tube voltage of 33 kV is used in the three upper plots. The average absorption values are computed as the intensity average of the x-ray absorption efficiency of the detection screen. In real cases, the detector MTF depends on the x-ray detection position within the screen and the intensity distribution within the screen is energy-dependent.

We can see that for the "no weight" and the "$\propto$ E CEW" cases, there is an optimal screen thickness. Using a thicker screen reduces the SNR due to the lower SDS of the additionally detected higher energy photons. The "optimal CEW" and "optimal DEW" methods however prevent this effect. In addition, a thinner screen may have a better MTF (this effect is not simulated here).

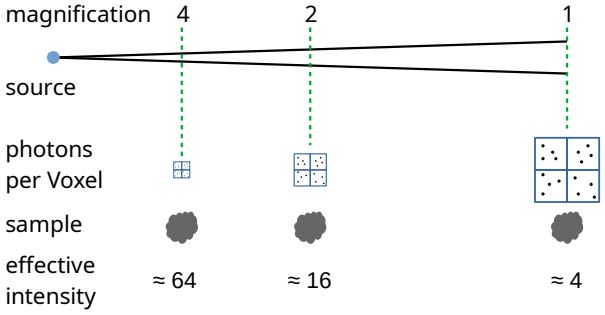

Figure 3.16.: Visualization of the effective intensity scaling with the x-ray magnification. The effective intensity per sample area becomes larger as the magnification increases.

In fig. 3.15 (bottom) the values of the average x-ray absorption of the detector for the t with the maximal SNR are shown. It can be seen that in the absence of optimal CEW or DEW, lower average absorption values are optimal for higher degrees of polychromaticity. This is an application of the DEW, as discussed before.

The average absorption for "no weight" is identical with a polychromatically averaged DQE, eq. (3.19). Thus the "no weight" and the "$\propto$ E CEW" cases have an optimal SNR at a specific value of the polychromatic DQE which is different from the maximal DQE. Raising the DQE usually has other costs (e.g. worse MTF), so that in this case, increasing the DQE beyond its optimum can have direct and indirect disadvantages. The "optimal CEW" and "optimal DEW" cases do not benefit significantly if the detector thickness is increased beyond this point.

3.6. Sampling magnification

The effect of the x-ray magnification is different from the effects discussed before in that it is much more fundamental. It stems from the fact that changing the x-ray magnification M changes the distance of the sampling points in the object space. Due to the fact that area sampling is used, the mapping from detector area to object area is then changed.

If we hold the distance between source and detector constant, then the number of detected photons per detector pixel area A_{det} stays constant. Changing M by moving the object influences the object pixel area A_{obj} in the following way:

$$A_{\text{obj}} = \frac{A_{\text{det}}}{M^2} \tag{3.81}$$

due to the fact that the pixel area is two-dimensional. See 3.16 for a sketch demonstrating this fact. This has the effect that in object space, the intensity per area (effective intensity I_{eff}) is scaled with respect to the source object distance l_{SOD} according to:

$$SNR(u) \propto I_{\text{eff}} \propto \frac{1}{l_{SOD}^2} \propto M^2 \tag{3.82}$$

Therefore, simply increasing the x-ray magnification increases the image quality, potentially by a large factor. This effect is independent of a change in MTF. The effective detector area (field of view) becomes proportionally smaller, so the amount of sample information gathered by the measurement stays constant. The number of x-ray photons passing through an object volume element is also proportional to the square of the x-ray magnification. For medical imaging, this means that the dose is increased accordingly. The image quality per dose is then independent of M, so this effect is not useful for dose-limited medical imaging.

I did not find this effect in the literature, so it appears to be a new discovery–even though it is a very fundamental effect. This effect was discovered when a $SNR(u)$ measurement showed results which were surprising at that point (see section 4.2.4). Because using eq. (3.3) means that the SNR spectrum is independent of how the power spectra are normalized, the effect could be observed even though it was not expected.

When temporal SNR or $CNR_{\text{NDT}}(u)$ is used to describe image quality, it is therefore necessary to normalize this quantity with respect to object pixel area. Otherwise, image quality appears to be independent of M, which would be misleading. This fact is another reason why temporal quantities should not be used in imaging—here, the imaging physics happens in continuous space. Using a quantity based on a variable spatial discretization poses severe difficulties.

From a different point of view, letting the x-ray intensity distribution after the sample propagate through space does not change its information content (SNR). The only change is that the same image is further magnified and larger or more detector pixels would be required to achieve the same field of view. Except of course for the x-rays absorbed in the additional propagation length e.g. in air. For phase contrast, propagation does change the SNR, so the above stated effect is (partially) canceled by the stronger phase contrast. What actually limits the x-ray image quality is the number of (later detected) x-ray photons interacting per sample volume, not the number of x-ray photons incident per detector area.

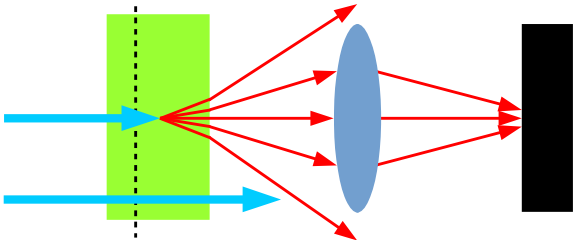

Figure 3.17.: The geometry of the indirect detection process for an lens coupled cristalline scintillation screen. Inside the volume of the scintillator screen (green), a fraction of the incident x-ray photons (light blue arrows) is converted to visible light photons (red arrows). A fraction of the many visible light photons from one x-ray photon are mapped to an area on the detector (black).

3.7. Noise properties of indirect detectors

The indirect detector (see section 3.3.3) is the most common technical implementation of a x-ray imaging detector. Its noise significantly differs from the typical white noise and this difference has a large influence on the image quality of this kind of detector. In the following, I will give a short description of the noise properties of indirect x-ray detectors. This derivation is both interesting from a theoretical standpoint and the result is very useful for a practical understanding of the image quality of an indirect detector.

3.7.1. Indirect detection process

The stages in a cascaded systems analysis [38] used to calculate a noise power spectrum (NPS) of indirect detectors can be simplified if we merge some stages into a single stage that approximately behaves like a Poisson process. The stage described here is identical to a combination of a stochastic amplification and a stochastic scattering stage as described in [24] and the result is fundamentally identical.

The derivation presented in the following is interesting in itself because of its simplicity. The difficulty is shifted to an advanced application of probability theory and logic, which uses temporal reordering of independent events to simplify the computation. Also, use is made of the particle/wave duality where average intensities are computed from wave propagation and noise from quantized detection.

A stochastic process is a Poisson process if (A) single events arrive with (B) a constant rate (mean counts per time or space) and (C) if the probability for a (future) event is independent of past/other events (Markov property) [17]. The sum of the events over a certain integration time/area is then Poisson-distributed. Poisson processes have the property that a sum of Poisson processes is again a Poisson process.

In general this means that if a Poisson process passes through a stage where a fraction of the quanta (e.g. photons) is transmitted/detected or one quantum is converted into (at most) exactly one other quantum (e.g. photon to electron), the resulting process is still a Poisson process, only with a different rate.

If a (primary) quantum is converted into more than one secondary quantum in a stage, then the secondary quanta from one primary quantum are correlated (temporally and spatially). The Markov property is not fulfilled and the resulting process is not a (simple) Poisson process. In the simplest case, it is then called a "compound poisson process". See e.g. [17] for a description of stochastic processes. The number of detected secondary quanta per primary quantum is usually Poisson-distributed per pixel, if the above conditions are fulfilled.[5]

In an indirect x-ray detector, the x-ray photons (primary quanta) are absorbed in a scintillation screen and generate visible light photons (secondary quanta). The visible light photons are then mapped to a CCD or CMOS camera and detected there. The whole two-step process is shown in fig. 3.17.

This mapping can be written as a convolution ($*$) with a point spread function (PSF) h_v (normalized to one). For optically coupled screens, the PSF includes effects from diffraction at the lens aperture and defect of focus [30]; for other screens the PSF is usually given by light spreading. This PSF is multiplied by the mean number c of detected visible light photons per x-ray photon (conversion factor) to calculate the average number of detected visible light photons. All the effects on the number of visible light photons detected up to and including the conversion of photons to electrons in the camera chip can be combined to one Poisson process and are included in this factor. We can thus write for the light conversion efficiency

$$c = \eta_{\text{scint.}} \frac{E_{\text{x-ray}}}{E_{\text{scint.}}} \eta_{\text{coll.}} \eta_{\text{transm.}} \eta_{\text{camera}} \tag{3.83}$$

where $\eta_{\text{scint.}}$ is the energy efficiency of the scintillation, $E_{\text{x-ray}}$ is the x-ray energy, $E_{\text{scint.}}$ is the energy of the scintillation light, η_{coll} and $\eta_{\text{transm.}}$ are the collection and transmission efficiency of the optics and η_{camera} is the quantum efficiency (detection probability) of the visible light camera. For all efficiencies (η), the possible range is between 0 and 1. Note that $\eta_{\text{scint.}}$ may depend on $E_{\text{x-ray}}$.

3.7.2. Indirect detection noise

The probability distribution for the data $d(x)$ (number of detected photons) is then a Poisson probability distribution $\mathcal{P}(d|s)$ for given mean signal $s(x)$:

$$\mathcal{P}(d|s) = \frac{s^d}{d!} e^{-d} \tag{3.84}$$

If we use eq. (2.33), we wan write the probability distribution p for Poisson noise (shot noise) as

$$p(n|s) = \mathcal{P}(s+n|s) = \frac{s^{(s+n)}}{(s+n)!} e^{-(s+n)} \tag{3.85}$$

In the following, I will omit spatial coordinates and the dependency on the x-ray energy for brevity of the notation; the index r is used for x-ray light effects and the index v for visual light effects. The absorbed fraction a describes the fraction of incident x-ray photons that are absorbed in the screen. The mean of the visible light photons s_v is derived from the number of detected x-ray photons d_r with eq. (2.33) as:

$$s_v = d_r * h_v c = s_r * h_v c + n_r * h_v c \tag{3.86}$$

From the perspective of the second Poisson process, the first Poisson process can be considered to have already happened, this can be seen as reordering all first stage detection events to happen before all second stage events. So d_r is a given set of x-ray detection events that happened within the detection time window. The number of visible light photons detected by the indirect detection process is then

$$d_{id} = s_v + n_v = s_r * h_v c + n_r * h_v c + n_v \tag{3.87}$$

[5] The Markov property for a spacial scattering process means that detection probability at one point in space is independent from that at other points in space which are on the detector.

The probability distributions for Poisson noise n_r and n_v are given by eq. (3.85).

The deterministic and random contributions can then be identified as the signal s_{id} and noise n_{id} of an indirect detection process:

$$s_{id} = s_r * h_v c \tag{3.88}$$

$$n_{id} = n_r * h_v c + n_v \tag{3.89}$$

The noise power spectrum N_{id} of an indirect detection process can be derived using eq. (2.23):

$$N_{id}(u) = N_r(u) c^2 H_v(u,E)^2 + N_v(u,E) \tag{3.90}$$

In the following, N_r and N_v are approximated as Gaussian white noise, such that

$$\begin{aligned} N_r(u) &\approx \mathrm{Var}\{\mathcal{P}(n_r|as_r)\} = as_r \\ N_v(u,E) &\approx s_v = acs_r \qquad (3.91) \\ \Rightarrow N_{id}(u) &\approx as_r \left[c^2 H_v(u,E)^2 + c\right] \qquad (3.92) \end{aligned}$$

$N_{id}(u) = N_{id}(u,E,z,...)$ is the noise power spectrum of a simplified indirect detector. It also depends at least on E and z in a broader context–the equation above is valid only for a single photon class. The influence of the MTF on the noise structure is also called "quantum mottle" in older literature [41].

In the presence of x-ray scattering in the detector plane, the detection process has three instead of two stages and an additional noise term appears. Also, the stages are then branching, which splits scattered and non-scattered radiation into different part images. These can then be superimposed to get the whole image. Splitting intensities before some processes and then superimposing them afterwards is a useful computational tool.

This computation technique can also be used in more complicated situations (e.g. x-ray fluorescence of the detector material). Combined with the superposition rules for signal and noise, the signal and noise properties for for arbitrary multistage and parallel photon paths can be computed.

3.7.3. Detector characterization by NPS

As we have seen, the shape of the noise power spectrum of an indirect detector is given by its visual light MTF and its light conversion efficiency. This makes it possible to determine these properties of the detector from a measured NPS if the number of detected visual light photons ($= as_r c$) can be determined. Alternatively, if $H_v(u_{ny})^2 \approx 0$ (= no aliasing criterion) one can use $as_r c \approx N_{id}(u_{ny})$ (u_{ny} is the nyquist frequency).

It follows then from eq. (3.92) that:

$$c \approx \frac{N_{id}(0) - as_r c}{as_r c} \tag{3.93}$$

$$H_v(u,E) \approx \sqrt{\frac{N_{id}(u) - as_r c}{as_r c^2}} \tag{3.94}$$

In practice, $N_{id}(0)$ should be determined through extrapolation from low spatial frequencies or a noise power spectrum fit, because the value of $N_{id}(0)$ has a large statistical error. Additionally, x-ray scattering in the detector can affect the low spatial frequencies of the noise power spectrum and may even make this type of evaluation impossible. The additional noise N_0 (see eq. (3.28)) must be subtracted from the noise power spectrum before doing the above evaluation.

For a polychromatic x-ray spectrum, the value given by eq. (3.93) is the spectral average of c^2 divided by the spectral average of c. It lies within the range of values of c for the x-ray spectrum. This method nevertheless allows an estimate of the effective c without the need for specialized equipment. Note that in practice, a comparatively higher value of c may also be the result of a comparatively higher-energy x-ray spectrum (e.g. caused by a thicker scintillator).

The MTF H_v determined by eq. (3.94) describes the spreading/blur of the visible light photons in the detector. For polychromatic x-ray light, the value is the noise-effective MTF, because the superposition laws are different for noise and signal. In general, the signal-effective MTF is different from the noise-effective MTF, see 3.4.4 for the signal-effective parameters.

3.7.4. Quantum efficiency spectra for an indirect detector

From the noise power spectrum for indirect detection, we can derive the Quantum Efficiency spectrum $\mathrm{QE}(u,E)$ for a photon class. As discussed before, a SNR spectrum $\mathrm{SNR}(u)$ is not proportional to the $\mathrm{QE}(u,E)$ (or an average of thereof) while the class SNR spectrum $\mathrm{SNR}(u,E)$ is. The QE can be understood as a strictly monochromatic quantity that is otherwise defined identically to the DQE.

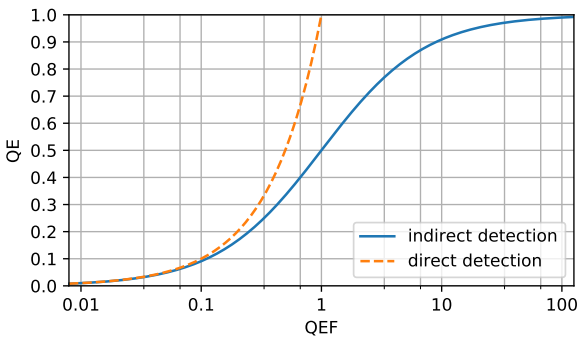

Figure 3.18.: The dependence of the Quantum Efficiency on the QEF of indirect detection (blue) and direct detection (orange dashed) based on equations eq. (3.102) and 3.103). For indirect detection, a significant gain in image quality is produced by increasing the QEF roughly to a factor of 10.

The ideal and indirect detection SNR can be computed using eq. (3.30) for monochromatic x-rays:

$$\mathrm{SNR}_{\mathrm{ideal}}(u,E) = \mathrm{P}\frac{I^2 a^{-1}\kappa^2 \mathbf{h}^2}{I} \tag{3.95}$$

$$\mathrm{SNR}_{\mathrm{idd}}(u,E) = \mathrm{P}\frac{I^2\kappa^2\mathbf{h}^2\ c^2\mathbf{h}_v^2}{I(c^2\mathbf{h}_v^2 + c)} \tag{3.96}$$

The QE at energy E is then:

$$\mathrm{QE}(u,E) = \frac{\mathrm{SNR}_{\mathrm{idd}}(u,E)}{\mathrm{SNR}_{\mathrm{ideal}}(u,E)} \tag{3.97}$$

$$= \frac{a(E)}{1 + c(E)^{-1}\mathbf{h}_v(u,E)^{-2}} \tag{3.98}$$

As this equation describes an energy-dependent device property curve, $\mathrm{QE}(u,E)$ is independent of the sample. The corresponding effective property $\mathrm{QE}(u)$ also depends on the sample, through its x-ray transparency.

Two quantum efficiency factors (QEF) for x-ray and visual light processes can be defined as

$$\mathrm{QEF}_r(u) = a \tag{3.99}$$

$$\mathrm{QEF}_v(u,E) = c\mathbf{h}_v(u,E)^2 \tag{3.100}$$

The zero-frequency QEFs are the absorbed fraction a and the conversion factor c, respectively. We can now write $\mathrm{QE}(u)$ only dependent from these QEFs:

$$\mathrm{QE}(u) = \mathrm{QEF}_r(u)\frac{1}{1 + \mathrm{QEF}_v(u,E)^{-1}} \tag{3.101}$$

This QE can be split into indirect and direct detection QEs:

$$\mathrm{QE}_{\mathrm{dir.}}(u) = \mathrm{QEF}_r(u);\ \ 0 < \ \mathrm{QEF}_r < 1 \tag{3.102}$$

$$\mathrm{QE}_{\mathrm{ind.}}(u) = \frac{1}{1 + \mathrm{QEF}_v(u,E)^{-1}};\ \ 0 < \ \mathrm{QEF}_v \tag{3.103}$$

In fig. 3.18, the dependencies of the direct and indirect detection QEs on their QEFs are shown. We can see that values of $c \gg 1$ can be useful if the imaging performance at $\mathbf{h}_v(u,E) \ll 1$ is of interest. For example at $\mathbf{h}_v(u,E) = 10\,\%$, the scale for c is shifted by two orders of magnitude, such that $c = 100$ results in $QE(u,E) = 0.5$. Even at $\mathbf{h}_v(u,E) \approx 1$, there is a significant benefit found by increasing c to roughly 10. If this increase comes at the cost of some other parameter (e.g. a), the optimum depends on the quantitative behavior.

For $c \to 0$, the properties of the indirect detector become identical with a direct detector: Its power spectrum is then white. This can be understood if we note that for $c \ll 1$, every primary photon produces at most one secondary photon, so that no correlations between secondary photons are possible. For $c \gg 1$, the noise of an indirect detector is so much different from white noise that the intuitive experience human observers have when interpreting noise largely fails. Comparing the image quality of images from detectors with very different c must thus always be done quantitatively, e.g. by comparing SNR spectra. Fundamentally, the blur caused by the detector MTF can be compensated for by a large c. After application of a signal reconstruction (e.g. Wiener deconvolution, see section 2.3.3), images become more comparable.

There are two interesting limiting cases for the indirect detection QE:

(a) Ideal detector limit: $\mathrm{QEF}_{\mathrm{ind.}} \gg 1 \Rightarrow \mathrm{QE}_{\mathrm{ind.}}(u) \approx 1$. This limit does not require $\mathbf{h}_v(u,E) \approx 1$ if c is large enough. A high conversion may thus completely compensate detector blur. Note that this fact alone makes a separate evaluation of noisiness and blur produce misleading results. The nominal and effective blur of such a detector are completely different, as noise is also blurred.

(b) Inefficient detection limit: $\mathrm{QEF}_{\mathrm{ind.}} \ll 1$. We can then approximate:

$$\mathrm{QE}(u)\Big|_{c\mathbf{h}_v(u,E)^2 \ll 1} \approx ac\mathbf{h}_v(u,E)^2 \tag{3.104}$$

An important fact is that SNR is not additive and that there is no concept of a polychromatic QE (or DQE) which reliably or accurately describes image quality influence independently of the sample.

4. Measuring x-ray image quality

Overview

The prior chapter discussed the theoretical aspects and predictions of x-ray image quality. This chapter complements this discussion by introducing measurement methods for the central quantities used in the prior chapter: SNR(u) and DE(u). In a sense, the usefulness of these quantities requires the measurement methods described in the following, as a scientific evaluation requires testing a theory through experiments.

Measuring image quality requires that some quantity is defined which we assume to describe image quality. The quantity used here is the SNR spectrum as defined in eq. (3.3) (fraction of signal/noise power spectra). The advantages of using this quantity for an imaging performance optimization were discussed in chapter 3.

Measurement methods for image quality used in MI [24, 34] and NDT [27, 28] all work by combining different quantities to an image quality measure. The method described in this chapter is different in the following way:

- There is no mixture of quantities determined from different physical situations (e.g. MTF from edge, NPS in empty region, contrast from sample). Combining measurements from potentially different image quality regions into one image quality measure can lead to systematic errors.
- The measurement setup is identical to the imaging setup—a real sample can be used when determining imaging performance. A defined test phantom can be used for comparable measurements or to improve the measurement accuracy.

The first point is significant because the NPS, MTF and other model parameters can change significantly depending on the sample placed in the beam, due to the sample changing the detected x-ray spectrum. Also, the effective MTF is weighted by the energy-dependent signal strength of the sample—different samples may have different MTFs (see eq. (3.32)). The latter is especially important for inline phase contrast. Commonly used measured properties like a polychromatically summed intensity have no clear relationship to image quality, as a higher intensity may both increase and decrease image quality (see section 3.4.5).

The SNR spectra measurement method presented in this chapter does not suffer from similar problems. It is also ideally suited to (automatically) optimize the imaging setup parameters (e.g. tube voltage) for a specific application or sample.

4.1. Theory

The SNR spectra measurement method presented here is not a complex method in the end, but the derivation of the main evaluation equation requires some thought. The derivation presented here has originally been published in [1]. For x-ray imaging, this method is not a completely new concept, similar approaches can be found for example in [44]. In the latter, noise power spectra are computed from the difference of two CT scans. Here, a more general formula using an arbitrary number of CT scans is derived. In addition, the signal power spectrum can be derived simultaneously.

What is also new is the systematic approach and the scope of the theory: I consider SNR spectra measurements the reference benchmark, other studies need to be confirmed by SNR spectra measurements to be considered correct. This is also one of the main use cases for this method: It can confirm or refute certain simplifications. SNR measurements have proven to be a useful tool in showing the limitations of simplified image quality evaluations.

The basic idea for the measurement method is based on the concepts introduced in section 2.3: The deterministic part (signal) of an image remains constant when a measurement is repeated, but the random part (noise) is different. This fact enables a separation of signal and noise by their physical properties.

The SNR measurement method presented here uses a series of images of the same object, measured consecutively. If we compute the average image of such a series, the SNR is higher, which means that noise becomes relatively weaker while the signal stays the same. Since the exact law of this behavior is known

(compare eq. (2.23) with eq. (2.24)), comparing single images with the average image can be used to separate signal and noise in the data.

4.1.1. Temporal noise

If we measure a series of images on an x-ray imaging setup, this series can be written as:

$$\{d_j(x)\}_j = \left\{ \frac{I_j(x) - I_\mathrm{d}(x)}{I_\mathrm{f}(x) - I_\mathrm{d}(x)} \right\}_j \tag{4.1}$$

where $j \in [1, K]$ and K is the number of images measured. Then the noise standard deviation can reliably determined by the variance of the intensity in each pixel along the time axis (different images):

$$\mathrm{std}_j\{d_j\} = \sqrt{\frac{1}{K}\sum_{j=1}^{K}\left(d_j - \mathrm{mean}_j\{d_j\}\right)^2} \tag{4.2}$$

An important requirement for the method to work is that the measured image series always has the same signal (sample). If the signal itself were to vary over time, the temporal standard deviation would include this variation in addition to the noise. There is no requirement that the the image has a constant gray value spatially—this method determines the noise for every individual pixel. To determine SNR, contrast or signal needs to be determined separately, but this method yields a very reliable measurement of the noise. Alternatively, noise can be estimated from the standard deviation of different pixels, if the mean intensity of the pixels is equal, which would be less reliable.

4.1.2. Measuring SNR spectra

For determining SNR spectra, the method described above is extended. First, we define the average image as:

$$\begin{aligned} d_\mathrm{avg}(x) &= \frac{1}{K}\sum_{j=1}^{K} d_j(x) \\ &= \frac{1}{K}\sum_{j=1}^{K}\left(s_j(x) + n_j(x)\right) \end{aligned} \tag{4.3}$$

To simplify the power spectra of the single image and the average image we can use the fact that noise is uncorrelated with any other noise or signal, see section 2.2.3. This corresponds to the fact that the noise in each single image is uncorrelated with the noise in another image, while the signal is fully correlated for two images. We can therefore derive for the power spectrum $D(u)$ of an image:

$$D(u) = S(u) + N(u) \tag{4.4}$$

$$\begin{aligned} D_\mathrm{avg}(u) &= S_\mathrm{avg}(u) + \frac{1}{K^2}\sum_{j=1}^{K} N(u) \\ &= S(u) + \frac{1}{K}N(u) \end{aligned} \tag{4.5}$$

In the last step, the linear noise power spectra sum leads to the fact that the noise fraction in the averaged image is inversely proportional to K. These two equations can be seen as a system of equations with the two variables $N(u)$ and $S(u)$ and the constants K, $D(u)$ and $D_\mathrm{avg}(u)$. Solving for the variables gives:

$$S(u) = \frac{D_\mathrm{avg}(u) - K^{-1}D(u)}{(1 - K^{-1})} \tag{4.6}$$

$$N(u) = \frac{D(u) - D_\mathrm{avg}(u)}{(1 - K^{-1})} \tag{4.7}$$

These two quantities are often of interest themselves. They can be used to evaluate the signal or noise properties of an imaging setup. The noise power spectrum measured this way is that of the x-rays transmitted through the sample, which means that it is the NPS which actually stems from the image.

From signal and noise power spectra we can compute the SNR spectrum as:

$$\mathrm{SNR}(u) = \frac{S(u)}{N(u)} = \frac{D_\mathrm{avg}(u) - K^{-1}D(u)}{D(u) - D_\mathrm{avg}(u)} \tag{4.8}$$

This is the fundamental equation for the SNR spectra measurement method, it can be used to determine the image quality of a measurement setup from a series of images. Due to how the derivation is done, the SNR derived is the value for the exposure time of a single image. The method separates signal and noise by their physical properties, so any part of the image that has the corresponding properties will be interpreted as signal or noise. Noise is correctly identified in most cases, but image artifacts are often falsely identified as signal (see next section).

Any image series that behaves like eq. (4.4) and (4.5) can be used for a SNR spectra measurements. This is especially important if the images are not direct measurements, but were transformed by an arbitrary transform $T\{d\}$. The transform need not be linear, but should not introduce strong assumptions into the data. Also, noise must be transferred through this transform. An example of a transform that would result in a broken SNR evaluation is the segmentation

of an image. It is important that the transform is applied to the single images and the averaging is done after the transform, in case the transform is not linear.

Examples for such transforms are the radiography referencing, eq. (2.1), or CT reconstruction. In the latter case, several CT images are used to compute the SNR spectrum of the volume image.

Interpreting SNR spectra has been discussed in section 3.1, see also figures 3.4 and 3.6. The most important aspects to keep in mind are that the SNR spectrum includes the object spectrum $P(u)$. Comparison between experimental configurations should therefore be done at a specific structure size. Then $P(u)$ is constant and does not influence the differences. Absolute evaluations of the imaging performance should use the quantity $DE(u)$ instead of $SNR(u)$, see eq. (3.31) and section 4.1.5.

4.1.3. Systematic errors

The systematic errors for the SNR spectra measurement can be split into noise artifacts and signal artifacts. The general rule is that noise artifacts only appear if the measurement was done wrong and that signal artifacts may not be avoidable for a specific setup but may be (partially) corrected.

Both types of errors are real measurement errors, which means they result from the measurement procedure. Errors resulting from wrong assumptions about the sample cannot occur with this method, since no such assumptions are made.

Noise artifacts

Noise artifacts appear when the following requirement (already stated above) is violated: The only difference between images in the series must be the noise realization. An example case for this is signal movement: The sample or source moves during the measurement. The difference between consecutive images then contains a sample shift. This will typically result in a peak in the computed noise power spectrum, which corresponds to the shift.

For the case of signal movement, the shape of the noise artifact can be computed when some simplifications are used. If we assume a movement in the y-direction with a constant speed during the acquisition of the image series, a rectangular PSF and a sinc-MTF (see section 2.2) is applied to the signal. The width d of the PSF is given by the movement distance during the acquisition time τ for one image. The corresponding MTF for a single image is correctly interpreted as a signal MTF, because the signal is actually blurred and a sample movement decreases the image quality. Note that sample movement changes the laws of how a change in exposure time affects image quality.

The MTF effect of signal movement is then the difference between the movement MTFs of the average image and the single image:

$$\mathbf{h}_{\mathrm{mov}}(u_y) = \frac{\mathrm{sinc}(Kdu_y)}{\mathrm{sinc}(du_y)} \tag{4.9}$$

$$N_{\mathrm{mov}}(u_y) = \frac{D(u_y) - S(u)\mathbf{h}_{\mathrm{mov}}(u_y)^2 - \frac{1}{K}N(u)}{(1 - K^{-1})} \tag{4.10}$$

A noise power spectrum affected by a signal movement artifact thus has peaks where $\mathbf{h}_{\mathrm{mov}}(u_y)$ has its roots. Correcting these noise artifacts by backshifting the images does not work, due to the fact that subpixel shifts would require interpolation and this interpolation would distort the evaluation.

Reducing the signal movement artifact by a significant amount without knowing the shift can be done in the following way: Choose all sets of two consecutive images, apply eq. (4.8) to each, and then average the results. The disadvantage of this method is that the random errors become more severe.

Signal artifacts

Signal artifacts result from any static part of the image which was not generated by the signal. This is the main weakness of the SNR spectra measurement method, as any part of the data which behaves like a signal is interpreted as such. In practice, one must carefully investigate if the signal result may have been produced for example by image artifacts. Most signal artifacts appear as additive (white) noise. Typical image signal power spectra decrease towards smaller structures due to the MTF of the experimental setup and the intrinsic object spectrum (see also fig. 3.10). In that case, signal artifacts appear as an artificial lower limit to the signal power spectrum. Even signal artifacts caused by color noise (see 3.6) usually have a very different power spectrum shape than the real signal.

The simplest kind of signal artifacts are permanently bright/dark pixels in the detector (”bad pixels”). Due to the abrupt transition in gray value from the surrounding pixels, this kind of artifact has a high fraction of high frequency components (its spectrum is

white). An artificially high SNR spectrum at high frequencies is the resulting error. This artifact can be removed by filtering the defective pixels and replacing the gray value with the median or average of the surrounding pixels. Such a signal artifact can typically be recognized by a measured signal power spectrum which (artificially) converges to a constant value towards higher spatial frequencies.

If an image is referenced using eq. (2.1), any noise in the (averaged) flat or dark image will produce signal artifacts. The shape of this signal artifacts is identical to the shape of the corresponding noise power spectra. Typically, flat and dark images are acquired as the average of an image series, in this case eq. (4.7) can be used to estimate the corresponding signal artifacts. The simplest method to compute the propagation through eq. (2.1) is by computing the series of images that were normalized with the individual noisy flat images:

$$\left\{ d_{\text{flat, j}}(x) \right\}_{\text{j}} = \left\{ \frac{I_{\text{avg}}(x) - I_{\text{d}}(x)}{I_{\text{flat, j}}(x) - I_{\text{d}}(x)} \right\}_{\text{j}} \tag{4.11}$$

Such a series can then simply be evaluated according to eq. (4.7), where we must keep in mind that the referencing uses not a single image but the average:

$$S_{\text{artifact flat}}(u) = \frac{N_{\text{flat}}(u)}{K_{\text{flat}}} \tag{4.12}$$

$$= \frac{1}{K_{\text{flat}}} \frac{D_{\text{flat}}(u) - D_{\text{avg, flat}}(u)}{\left(1 - K_{\text{flat}}^{-1}\right)} \tag{4.13}$$

Due to the fact that this signal power spectrum contribution is uncorrelated with the image signal itself, it can be subtracted in the SNR spectrum evaluation from the signal power spectrum computed with eq. (4.6).

Signal artifacts typically appear if the signal becomes very weak due to the MTF becoming very small (e.g. < 0.01). The corresponding frequency range is then not of interest, because for realistic exposure times the SNR spectrum is too low for detection. This frequency range where the SNR measurement fails is typically at $SNR(u) < 10^{-2}$ for x-ray detectors without a high amount of pixel defects.

Computation precision

Computing power spectra from images generally requires applying a window function to the image [45, 46] before the Fourier transform. A window function avoids introducing frequency errors due to the fact that power spectra are computed from a limited area of an extended signal while using a FFT (fast Fourier transform) algorithm. The FFT algorithm assumes periodic boundary conditions, which means that left/right and bottom/up image edges are implicitly connected. Discontinuities between opposite edges thus lead to computation artifacts for power spectra.

Power spectra in imaging are typically smooth (no peaks), as images usually have no long range periodic structures. Therefore, frequency precision requirements are low. Reducing noise in the computed power spectrum is more important for SNR spectra measurements. Window functions amplify noise if they weight image pixels differently. In imaging, large window sizes of more than 500x500 pixels can often be used, which reduces the computation errors. In higher dimensions, the window noise amplifications gets worse—effectively using only the center 50 % in length of a cube is only 1/8 of its volume and amplifies noise (variance) by a factor of 8.

The window functions used here are chosen as the convolution of a rectangular region offset by m pixels from the image edge with a Gaussian with a standard deviation of $m/4$ (default $m = 16$). This window function has a very low noise amplification even in higher dimensions. Example: Hanning window in 3D has a noise amplification of 3.40, the Gaussian convolution window 1.18 (512^3 volume). The former has significantly less error at small frequency shifts, but both perform well for large frequency shifts. Additionally, care must be taken to compute power spectra with a 64 bit float FFT, as using 32 bit float can lead to significant computation errors.

4.1.4. Choice of the test phantom

Choosing a good test phantom for SNR spectra measurements allows for simple and reliable measurements. Thereby, the following aspects should be considered:

- Beam alignment errors need to be avoided by choosing an test phantom whose object spectrum does not change with slight tilts to the beam. This is required to get comparability between repeated measurements and also because in cone beam geometry, the angle of the beam varies over the object.
- Statistical measurement errors can be decreased by using an object with rich structural details. A

stronger signal means a smaller relative error, the absolute noise remains the same. As the absolute scale is irrelevant (or normalized for $DE(u)$), more structure does not affect the optimization. The size scale of the structure details should be similar to the size scales found in objects that are expected to be used on the setup.

- Object thicknesses and material should represent the application. See table 4.3 for an example of a range of application definitions. Using a range of thicknesses in different image regions allows to evaluate a range of use cases at once. The material needs to have an atomic number close to the material of the application. For example using Si ($Z = 14$) instead of Al ($Z = 13$) would yield similar results. Evaluating the image quality of a material interface (e.g. Al-Si) requires that the test phantom reproduces this interface.

Example setups for SNR measurements on projections and for CT are shown in figs. 4.1 and 4.2. They consist of two components: (1) a step wedge (2) an object to represent sample structure. For comparability between regions, the structure must be approximately identical everywhere (translationally invariant object spectrum). Examples for such structures are sandpaper (Z=14, 6) or paper (Z=6). Evaluating a specific material interface embedded or encased in a different material can be achieved by using respective materials for structure and step wedge. If only one sample thickness is considered, the step wedge can be omitted.

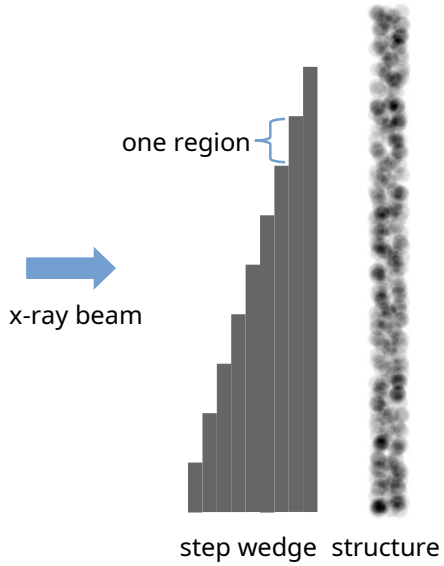

Figure 4.1.: Sketch for a 2D SNR spectra measurement test phantom example with different sample thicknesses in one measurement. The structure typically is a flat object, here seen from the side.

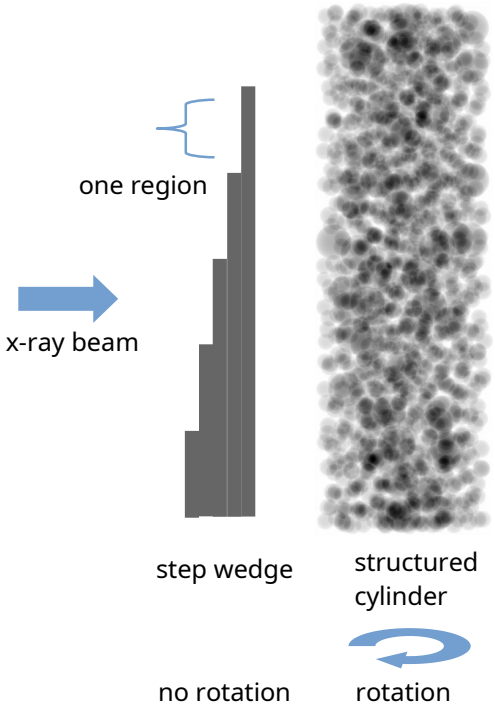

Figure 4.2.: Sketch for a 3D SNR spectra measurement test phantom example with different sample thicknesses in one measurement. SNR spectra are here evaluated on CT reconstructed images. For cone geometries, care must be taken to exclude the CT regions where different wedge thicknesses overlap during the rotation. The SNR is evaluated in the center of the cylinder so thickness differences from the cylinder are less.

4.1.5. Evaluating detection effectiveness

The detection effectiveness (see section 3.4.2 and eq. (3.31)) is a measure for image quality which is comparable between different test phantoms, as long as the material thicknesses are identical. While easy to define in theory, measuring a $DE(u)$ experimentally is more difficult than measuring $SNR(u)$. If the SNR spectrum and the object spectrum $P(u)$ are measured, the $DE(u)$ can be computed as:

$$DE(u) = \frac{SNR(u)}{P(u)} \tag{4.14}$$

Measuring the SNR spectrum has already been discussed, measuring the object spectrum is discussed in the following. The basic approach to determining the object spectrum is that the (true) object shape of the test phantom is determined from the measured data.

The object spectrum is then the power spectrum of the object shape.

In principle, a DE measurement could be performed both on projections and on CT measurements. There are two reasons why only use CT DE measurements were performed: (1) The actual application of the x-ray imaging is CT, image quality differences between CT and projections should be included by the measurement (2) Determining the object shape is more complicated in projections (especially for cone geometries). Real objects for a test phantom can be chosen to have smooth surfaces. Determining the object shape in a CT image is therefore easy, if morphologically simple objects are chosen for the test phantom.

The test phantom should satisfy the following criteria:

- The shape of the object should be as simple as possible to make the determination of the (true) shape reliable.
- There should be no image features below the resolution limit of the measurement, because their shape could not be determined.
- To avoid large statistical errors in the SNR measurement, the test phantom also needs to have a large amount of structure (= material edges).
- It must be possible to reproducibly manufacture the test phantom.

A test phantom which satisfies all these criteria is the ball heap phantom. It consists of some container (e.g. cylindrical glass) that is filled with balls. The size of the balls should always be chosen such that the diameter of a ball is at least several voxels – otherwise determining the correct center and diameter of a ball becomes difficult. Such a size would give a good compromise between the criteria above. To avoid long-range ordering of the balls, it is best to use different ball sizes.

If the ball size is known, the voxel size of the measurement can be calibrated exactly. Otherwise, this calibration needs to be done another way, as computing the $DE(u)$ accurately requires that the voxelsize is known. To compute $P(u)$, eq. (2.13) needs to be used where a is the voxelsize.

The distribution of the ball sizes may be e.g. a mixture of two sizes, which produces noticeable minima in the object spectrum. This makes it possible to clearly differentiate signal and noise power spectra (the latter does not have these minima). Alternatively, a broad distribution produces a smooth object spectrum, which avoids distortions in the measured $DE(u)$ caused by a slight mismatch of the minima from true and measured object spectra.

4.1.6. Ball phantom evaluation

The algorithm used to evaluate measurements from ball phantoms is described in the following. First, the (true) object shape needs to be computed from the measured data. This is done in the following steps:

1. Segment the measured CT image into the two segments air and material (balls).
2. Compute a (euclidean) distance transform d_{EDT} on the balls segment.
3. Determine the maxima of d_{EDT} such that every ball has exactly one maximum.
4. The lists of d_{EDT} values of the maxima and their coordinates are the radii and centers of the balls.
5. For every entry in these lists, one ball is placed in a virtual object image.

To speed up computations, the ball sizes are binned and the ideal ball image for one size bin is computed beforehand. This computation oversamples the ball to correctly reproduce partial voxel fill effects.[1] The placement is then done as the addition of the precomputed ball image of the approximate size, shifted by the center distance.

Computing the object spectrum is done by computing the power spectrum from the virtual object image. Then the SNR spectrum is determined as described before and DE is computed using eq. (4.14).

This algorithm is simple and reliable, but has the disadvantage that the ball centers are only determined to a precision of one voxel. An improved algorithm would determine the ball center position with a higher precision. For more complex test phantoms, an algorithm would need to determine the surfaces without assuming a specific shape of the object. For the purpose of studies where the individual parts of the test phantom have a shape close to a ball, the presented algorithm is sufficient.

[1] The effect of the voxel area on the MTF is thus not considered to affect image quality. Correspondingly, the gray value of a voxel is defined to represent the average of the continuous gray value inside its volume.

4.2. Applications in 2D

The main focus of the application examples lies in demonstrating the effectiveness of the SNR measurement method in investigating and optimizing image quality. Quantitative effects on real applications are highly application-specific and are therefore not covered in detail here. In this section, SNR measurements are performed on projections (2D), for applications on CT images see section 4.3 on page 73.

Image quality of projections directly propagates to the image quality of the CT image, except that an additional degradation is possible from certain CT artifacts. The required measurement times to achieve a good image quality are of course different for projections and CT images. Some possible artifacts are explained in section 3.2.1 on page 31. Object spectra in 2D and 3D are different for the same object. In 2D a superposition of object structure along the beam is measured, whereas in 3D the actual object structure is measured.

SNR measurements on projections (2D) require much less measurement time and are therefore to be preferred if measurements for many different setup parameters are needed. They may also be used as a preparation step for CT SNR measurements (3D): Optimal setup parameters are found in 2D for each imaging device, a comparable $DE(u)$ measurement is performed in 3D. The 3D measurements should thereby use the optimal parameters for the test phantom, which are generally different for different imaging devices (interactions of source and detector properties).

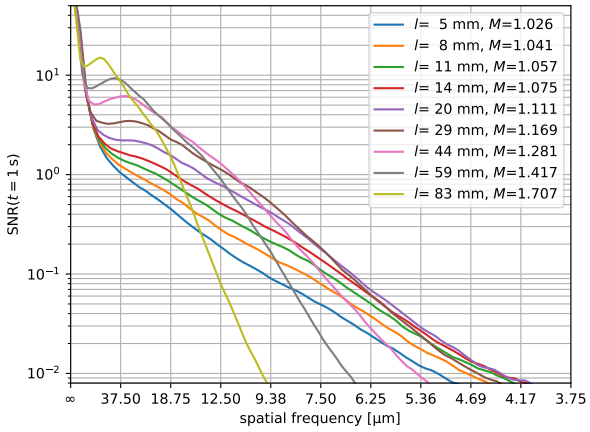

Figure 4.3.: Measurements of the SNR(t = 1 s) for the filter paper sample and the MR detector for different distances l from sample to detector with the x-ray magnifications M.

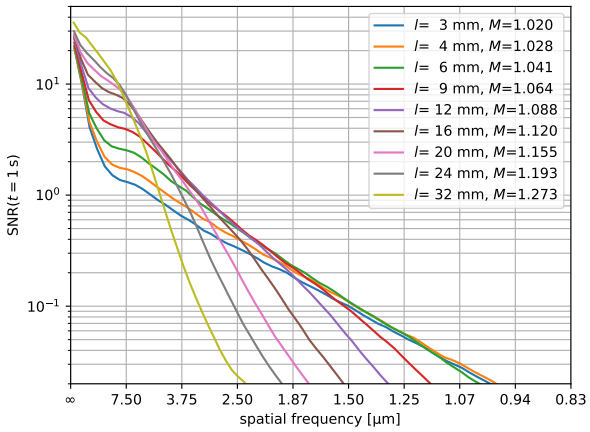

Figure 4.4.: Measurements of the SNR(t = 1 s) for the filter paper sample and the HR detector for different l.

4.2.1. Inline phase contrast magnification

This application example has been published in [1]. Prior work on the same topic is e.g. [47, 48, 49], but the SNR spectra measurement is uniquely able to quantify phase contrast image quality and extends the prior results.

The experimental setup [50] for the measurements is a laboratory x-ray computed tomography setup with micrometer resolution optimized for inline phase contrast imaging of weakly absorbing materials. The measurements were performed in cooperation with Andreas Balles and Christian Fella.

The setup is based on a liquid metal-jet source [51, 52], which has a strong x-ray emission line at 9.25 keV. It is operated at a source size of 14 µm and an acceleration voltage of 70 kV. Two different detectors

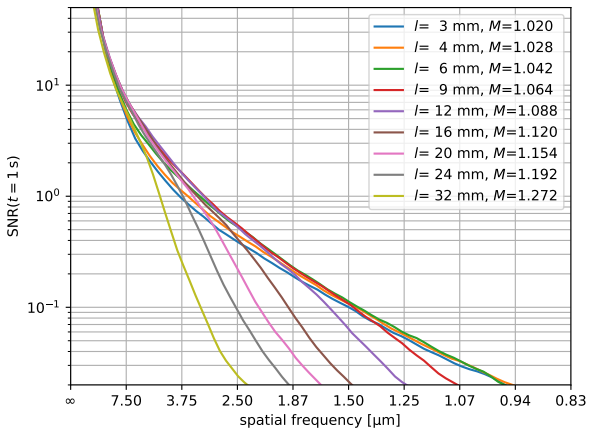

Figure 4.5.: Measurements of the SNR(t = 1 s) for the sandpaper sample and the HR detector for different l.

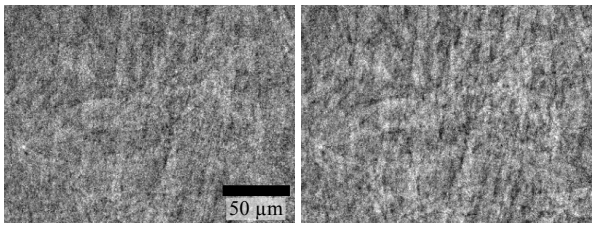

(a) l = 3 mm (b) l = 6 mm

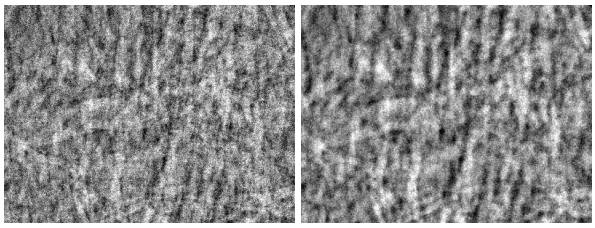

(c) l = 12 mm (d) l = 24 mm

Figure 4.6.: Measured images at distances l for the HR detector and the filter paper sample for t = 5 s. Images (b) to (d) are interpolated/cropped to the same sample region as (a). It can be seen that image (a) has insufficient phase contrast and appears noisy, while (d) has enough phase contrast but is too blurry (bad MTF). Image (b) or (c) is optimal.

were used: (1) A high resolution (HR) setup with a 5 µm thick LSO scintillation screen that is lens coupled [30, 53] to a cooled CMOS camera (NA = 0.75). (2) A medium resolution (MR) detector with a 50 µm thick LuAG screen [54]. Other properties of the measurements for the two detector setups are given in table table 4.1. Camera noise was determined from dark images at different integration times to a pixel median of $\approx (0.9\,\mathrm{e}^- + 0.2\,\mathrm{e}^-/\mathrm{s})$.

Power spectra for the SNR measurement were calculated from a 1400x1300 pixel region in the center of the detector and radially averaged/smoothed to generate one-dimensional spectra with approximately 50 bins. The measured images were corrected with dark and flat images, the static noise power from this process was estimated and subtracted from the calculated signal power spectrum. A negative logarithm was applied before calculating power spectra.

The cone beam propagation distance z that gives the strength of the phase contrast can be calculated from the sample-detector distance l_{SDD} and the x-ray magnification M, see eq. (3.16). The relative scale for the spatial frequency axes for the different sample positions was determined by registering the images for their relative magnifications with a precision of

detector	pixel size	d	intensity
MR	2.92 µm	200 mm	340 ± 32
HR	0.56 µm	150 mm	76 ± 9

Table 4.1.: Properties of the two detector setups used at the LMJ-CT; d is the distance from the source to the detector and the intensity is given in detected photons per pixel per second.

10^{-3}. The pixel sizes of both detectors were measured by taking several images with known horizontal shift and registering the images to a shift in pixels.

Measurements were performed for two different samples: (1) sandpaper, weak phase contrast (2) filter paper, strong phase contrast. For each sample, measurements were performed for different x-ray magnifications to determine the optimal value for this parameter.

The measured SNR spectra results are shown in figs. 4.3 to 4.5. They enable choosing the optimal magnification for a specific desired spatial resolution. The optimal magnification is the one with the highest SNR spectrum at a specific spatial frequency (structure size). Different structure sizes imply different optimal magnifications. As phase contrast becomes stronger for higher magnifications (for $M < 2$), lower spatial resolutions allow for more phase contrast and enable shorter exposure times. On the other hand, if the exposure time can be arbitrarily long, the additional SNR from phase contrast becomes irrelevant. In this case, very high resolutions are reached but phase contrast is negligible. Examples for images at different magnifications are shown in fig. 4.6.

4.2.2. Energy bandpass detection

In section 3.4.6 an effect was described which would increase the SNR of a x-ray image if the intensity of higher energy photons (lower signal strength) is reduced. Measurements to test this hypothesis were performed on the XRM-II x-ray microscope at the LRM in cooperation with Fabian Lutter. Its setup [55] consists of a 30 keV electron gun of a electron microscope which is targeted on a tungsten pin with a diameter of $\approx$ 50 nm. The whole setup is in vacuum and the x-rays are detected with a direct x-ray detector using CdTe as x-ray absorber.

The detector is known to have significant charge sharing [43, 56], which means that the energy determination of the thresholds which can be set is not very

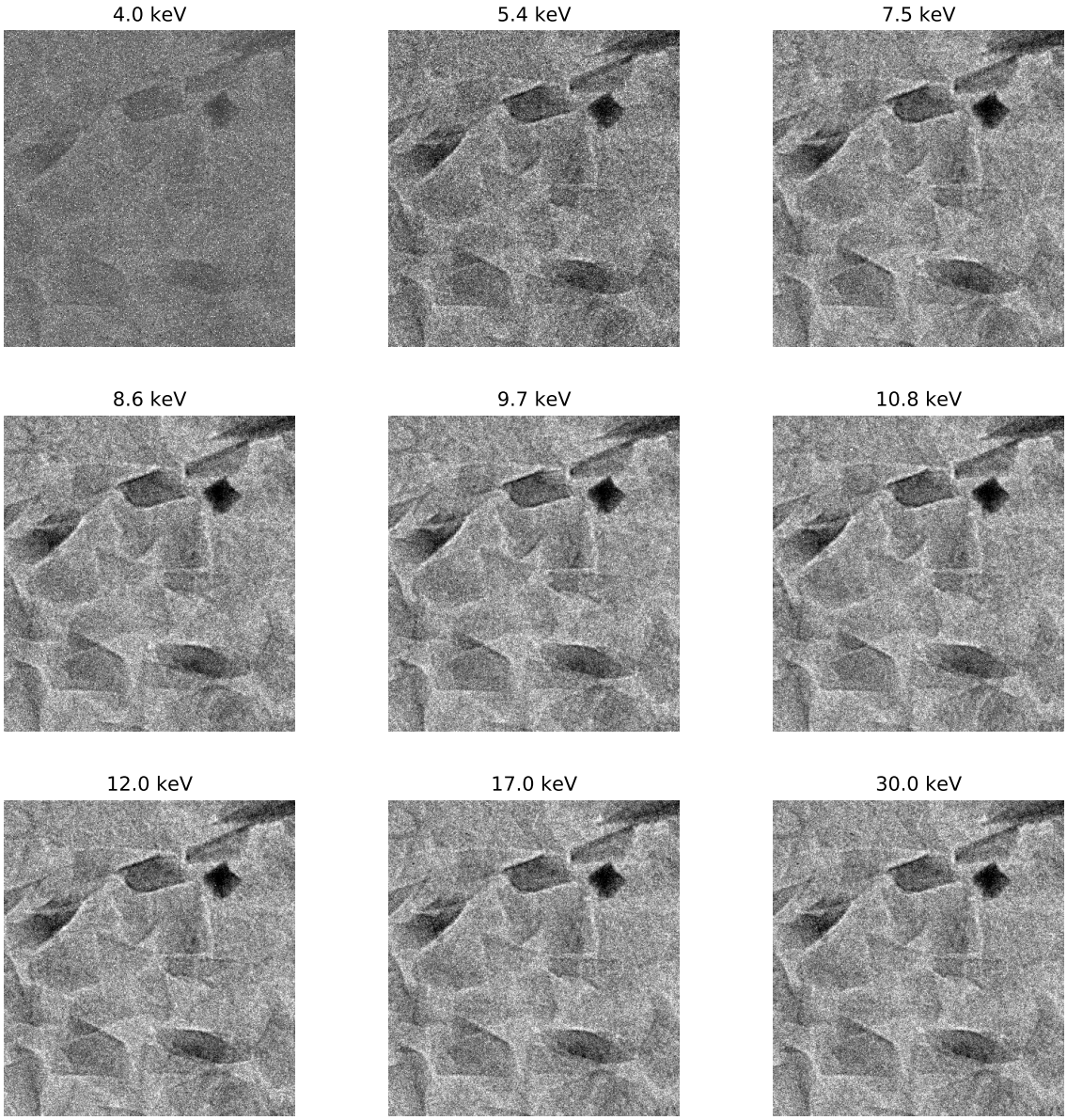

Figure 4.7.: Sample images for different upper energy thresholds (values above the images) of the energy bandpass detection. The part shown contains some SiC particles of a sandpaper. Comparable simulations are shown in fig. 3.8 b) and d)–f).

reliable. Also, charge sharing introduces a probabilistic energy weighting that weights higher energy x-ray photons more (which is detrimental for image quality). It should therefore be expected that any effects that rely on the energy resolution of the detector may appear weakly or not at all. Two images with different lower thresholds can acquired by this detector in one exposure, the difference of these images then contains the photons from the energy band which corresponds to the two thresholds.

A piece of sandpaper was used as the test phantom and parts of the resulting bandpass images are shown in fig. 4.7. The images with the lowest threshold shows strong unidentifiable noise and was not used for the further evaluation, the image with the next higher threshold (5.5 keV) shows this noise faintly–this should be considered in the interpretation of the results. The intensity in dependence on the upper energy threshold can be used to derive the x-ray spectra the detector determines, which is shown in fig. 4.8.

In fig. 4.9, the results of the SNR measurements for different detector energy thresholds are shown. As expected from the theory, photons above a specific energy threshold (here 10 keV) do not contribute

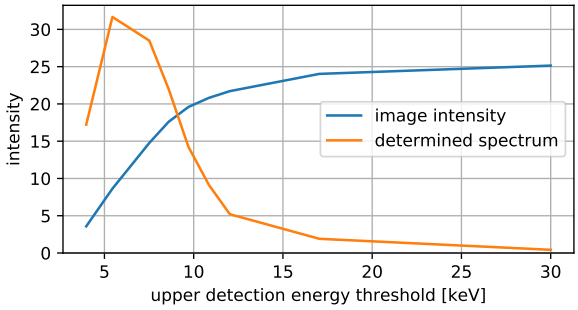

Figure 4.8.: X-ray energy spectrum derived from the intensity dependent on the upper energy threshold. The bin width is chosen as small as the detector allows.

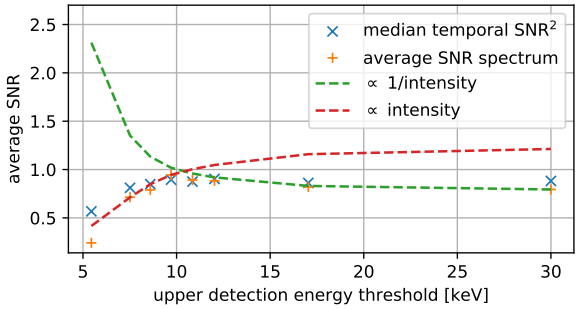

Figure 4.9.: SNR dependent from the upper energy threshold of the bandpass detection. Due to the fact that there is very little intensity above 17 keV (see fig. 4.8), significant SNR differences can only appear at 12 keV and below. While the SNR spectrum describes the image quality (including phase contrast), the temporal SNR only describes the absorption image quality. This explains the difference at the lowest energy bin. The two dashed curves describe the expected SNR curves for ideal superposition ($\kappa = \text{const.}$, red) and for additional intensity being noise only ($\kappa_{\text{add}} = 0$, green). Both curves are scaled such that the crossover is roughly at the optimal DEW threshold.

significantly to a higher SNR. The dashed lines are examples for $SNR \propto 1/I$ (photons only contribute noise) and $SNR \propto I$ (photons all contribute signal equally). While at 8–10 keV the latter law appears to hold, at $\geq$ 12 keV the former is true. The intermediate behavior is between these proportionalities (photons contribute signal differently), which can be seen at 11 keV.

This measurement thus appears to confirm the assumption that a bandpass detection is an effective form of CEW. A more precise measurement would require a detector with a better energy resolution. The bandpass detection method has been implemented in the XRM-II setup for daily use in nanoCT.

property	value
x-ray source	X-Ray WorX XWT-190-THCE PLUS, microfocus mode, "high energy", W transmission target (6 µm thick)
detector	Dexela NDT1512, Gd2O2S:Tb scintillator 75 µm pixelsize

Table 4.2.: MetRIC setup.

	U_{tube} [kV]	filter [mm]	material
A	60	none	sandpaper (Si, C)
B	140	1 Si, 1 Ge	aluminium (Al)
C	140	1 Si, 1 Ge	brass (Cu, Zn)
D	190	2 Fe, 2 Cu	brass (Cu, Zn)

Table 4.3.: Application cases for the SNR measurements with different scintillators. Sorted in ascending material thickness.

4.2.3. Different scintillators

The main properties of an indirect x-ray detector (see also section 3.7 on page 51) are given by:

- Thickness and density of the scintillator
  ⇒ absorption efficiency
- Material of the scintillator
  ⇒ absorption efficiency, light yield
- Optical properties for visual light
  ⇒ gathering efficiency (NA), MTF
- Electronic noise of the detector pixels
  ⇒ additive noise

Here, two different scintillator screens are compared while using the same detector optics and electronics. The first screen is a 30 μm thick Gadox powder screen and the second a 2 mm thick crystalline LuAG screen. Due to the higher light yield of the Gadox compared to LuAG and the fact that crystalline screens have a reduced gathering efficiency because of refraction at the crystal surface, the first screen is expected to have a much higher conversion factor c. On the other hand, the second screen has a much higher absorption efficiency due to a higher thickness and density. This higher thickness also results in a worse MTF due to

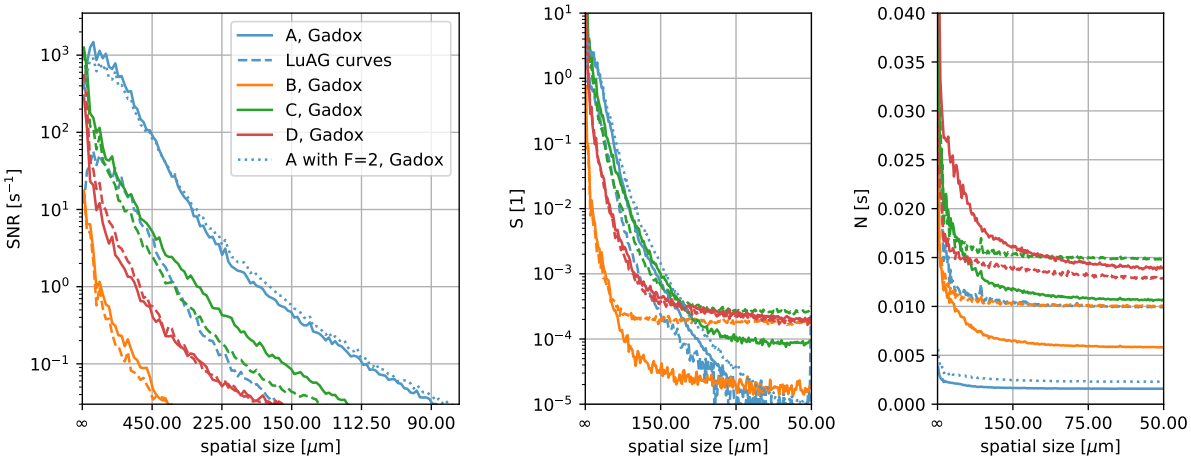

Figure 4.10.: SNR spectra measurement results for a range of applications and two different scintillator configurations ("LuAG", dashed lines and "Gadox", solid/dotted lines) on the same detector. The SNR plot is clipped in the y-direction to hide signal artifacts, they are visible in the signal power spectrum plot. See table 4.3 for a description of the cases A–D.

defect of focus.

Measurements were performed at the metRIC setup (see also table 4.5) with 9 W source power. Test phantoms were placed directly before the detector to eliminate source blurring influence.

Using the theory from section 3.4 on page 39, it is to be expected that the first screen performs better at lower x-ray energies and the other way around at higher energies. The exact point at which they are equally good is an interesting fact when deciding which screen is better for a specific use case.

To determine the relative performance, SNR spectra measurements were performed using different samples and different x-ray source spectra. The detector used is in-house developed and is called "KGSD" (KostenGünstiger SzintillationsDetektor). It uses a camera lens with adjustable f-number F, all measurements here use $F = 1.7$ except the one measurement with $F = 2$.

The different applications (test phantoms) are listed in table 4.3, results are shown in fig. 4.10. Measurements show that the Gadox screen performs much better at lower x-ray energies but for the 190 keV case, the LuAG screen is slightly better. The worse performance of the LuAG is not only caused by a higher noisiness (left plot), but also by a weaker signal (middle plot). The weaker signal was to be expected from the higher absorption efficiency of the LuAG screen, as it weights the higher energies stronger compared to the Gadox. At the higher energies, the lower optical conversion efficiency of the LuAG becomes less important while this screen benefits from its higher absorption efficiency. Noisiness is lower for the Gadox compared to LuAG for case A-C but higher for case D.

The measurement with $F = 2$ has a higher noise (lower intensity) and a better spatial resolution compared to $F = 1.7$, as expected for the thin Gadox screen. Cases B and C show the difference in absorption strength between aluminium and brass. After absorption through 1 mm Ge, aluminium produces almost no contrast (κ) while brass has good contrast.

From the shape of the noise power spectra we can derive that the Gadox screen has a much higher light conversion efficiency c. See also eq. (3.83) for c and section 3.7.3 for how detector properties shape the noise power spectrum. The values of c are roughly three times as high for the Gadox screen as for the LuAG screen, averaged over the respective detected x-ray spectra. As the average effective x-ray energy is higher for the LuAG screen, the difference in monochromatic light conversion efficiencies is higher than that factor.

4.2.4. X-ray magnification influence

As discussed in section 3.6, changing the x-ray magnification in a radiograpyh measurement scales the effective intensity according to eq. (3.82) ($SNR(u) \propto M^2$). This effect is separate from the effect that changes in the magnification have on the MTF and therefore $SNR(u)$. To test the prediction of the theory, it is therefore easiest to acquire SNR spectra measurements in a

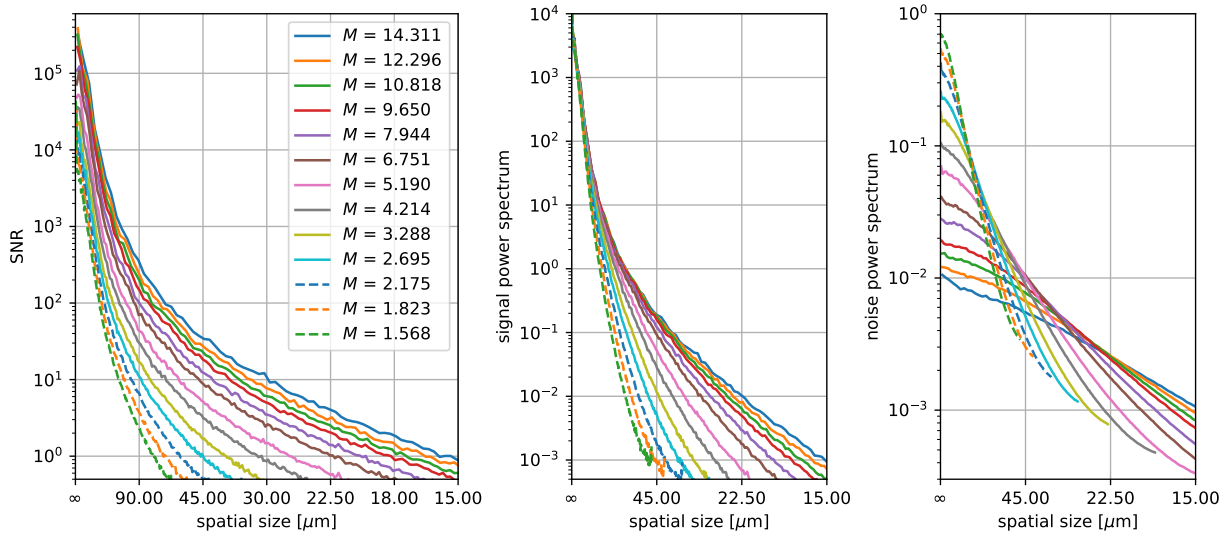

Figure 4.11.: Measured SNR spectra for the magnification sweep, see fig. 4.12 for an interpretation. Note that different choices of scaling the power spectra with the sampling distance are possible, but the SNR is unaffected by this choice. Here, signal power spectra have identical values if the same object is only sampled differently, although the higher spatial frequencies are distorted by MTF differences.

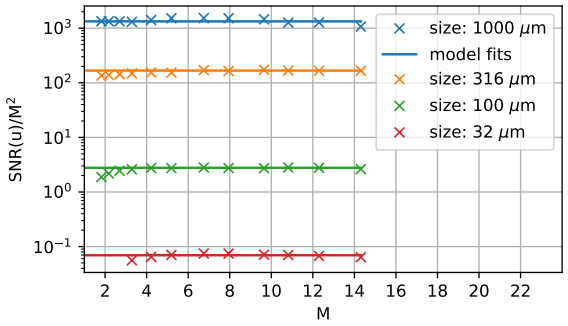

Figure 4.12.: SNR spectra measurement results for the magnification sweep. On the y-axis $SNR(u)/M^2$ is plotted, which should be constant with respect to M if the MTF is also constant. Towards lower magnifications and for smaller sizes, the SNR spectrum is reduced by a change in MTF.

parameter range where the system MTF of the setup is constant. Here, this situation was achieved by using a large x-ray source spot size and high magnifications.

SNR spectra measurements were performed on the MetRIC setup (see table 4.2. The x-ray magnification was varied by moving the sample along the beam axis and a SNR spetrum measurement was performed at every position, while the distance between source and detector was kept constant. A source setting of 20.0 W and 80 kV was used for all chosen x-ray magnifications. The detector exposure time was 100 ms and 50 projections were aquired per SNR measurement. As test phantom, a piece of sandpaper was used.

The relative difference in magnification values was determined by image registration. A high relative precision for the magnifications of the different measurements was therefore achieved (relative error $\approx 10^{-3}$). This high precision is required because wrongly scaling a steeply decreasing curve in the x-direction leads to large errors in the y-direction. The voxelsize was determined by comparing a known distance on the test phantom with the distance in pixels on the image (l_{PS} = 47.8 µm at the lowest magnification).

SNR spectra were computed from a central region on the detector with a size of 900x930 pixels. Therefore, lower magnification use larger sample areas. Slight differences in the particle density of the sandpaper may therefore introduce systematic deviations in $S(u)$ and $SNR(u)$ for large differences in magnification.

The measured SNR spectra are shown in fig. 4.11. At the lower spatial frequencies, the signal power spectrum is independent of M, but noise increases with higher M. The exact scaling of $SNR(u)$ with M is shown in fig. 4.12. In the latter figure, a good agreement of the measurements with the theoretical prediction (eq. (3.82)) is clearly visible. Even though the distance between source and detector is constant and the average number of incident x-ray photons per detector pixel is identical for all measurements, the noise power spectra show large differences. At the

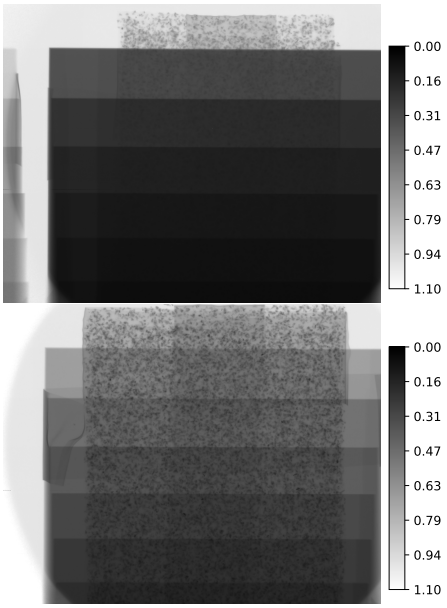

Figure 4.13.: Projection image examples (MetRIC) for the aluminium step wedge ($U_{\text{tube}} = 160\,\text{kV}$, top) and the plastic step wedge ($U_{\text{tube}} = 80\,\text{kV}$, bottom). The step wedges are oriented with downward increasing thickness, a step is 10 mm high. Sandpaper was fixed to the back of the step wedges and the regions chosen for SNR evaluation are where sandpaper is present. The topmost region is outside of the step wedge and is denoted as "0 mm".

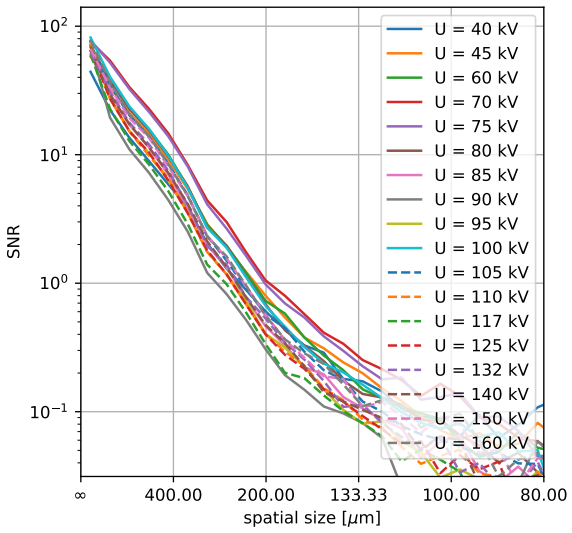

Figure 4.14.: One set of measured SNR spectra for the aluminium step wedge at 12 mm thickness (MetRIC). Overall, 12 such sets were evaluated and the results are shown in a comprehensible way in fig. 4.15.

property	value
x-ray source	Hamamatsu L8121-03 Microfocus, W reflection target
detector	Rayence 1215B, CsI scintillator, 50 µm pixelsize

Table 4.4.: CT500 setup.

lowest spatial frequencies of $N(u)$ (y-axis intercept), a magnification difference by a factor of ≈ 9 corresponds to a noise power spectrum difference by a factor of $\approx 9^2 \approx 80$.

In practical applications, the image quality can therefore be increased by a large amount if the sample is moved closer to the source—even when the MTF is purely source-limited. The field of view becomes correspondingly smaller, so this is only useful if the sample is small enough or it is sufficient to measure only a part of the sample (local tomography).

Both signal and noise power spectra are affected by the detector MTF, see eq. (3.96). Here, lower magnifications mean that the higher effective detector blur is present both in the nominator and denominator of the SNR spectra fraction, and both cancel each other out partially. Therefore, the magnification with the optimal SNR spectrum is shifted towards lower magnifications compared to the optimal magnification for MTF. This consideration excludes the effect of eq. (3.82) which shifts the optimum towards higher magnifications.

4.2.5. Optimal tube voltage

As discussed in section 3.4, the physical situation in x-ray imaging is given by polychromatic superposition of signal and noise, as well as strong energy dependencies in individual performance parameters (e.g. detector absorption efficiency). The approach here is therefore not to focus on evaluating in detail how a good or bad image quality emerges. Instead, the resulting image quality of a complex system is evaluated, with optimization as the aim. Drawing conclusions about the properties of the imaging setup from the measured $SNR(u)$ values is here of secondary importance.

Similar to the measurements described in the prior section, SNR measurements were also performed on the MetRIC setup and on the CT500 setup (see table 4.4), but here for different x-ray spectra.

These different spectra were generated by setting

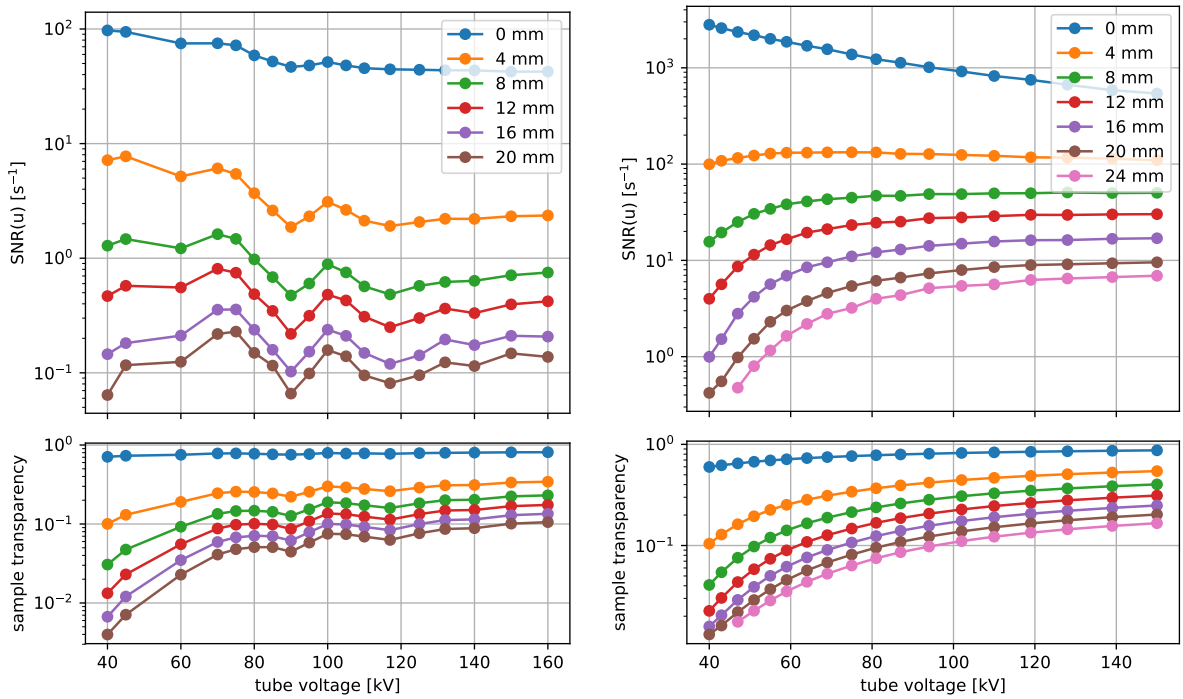

(a) Al material, Si contrast @ MetRIC

(b) Al material, Si contrast @ CT500

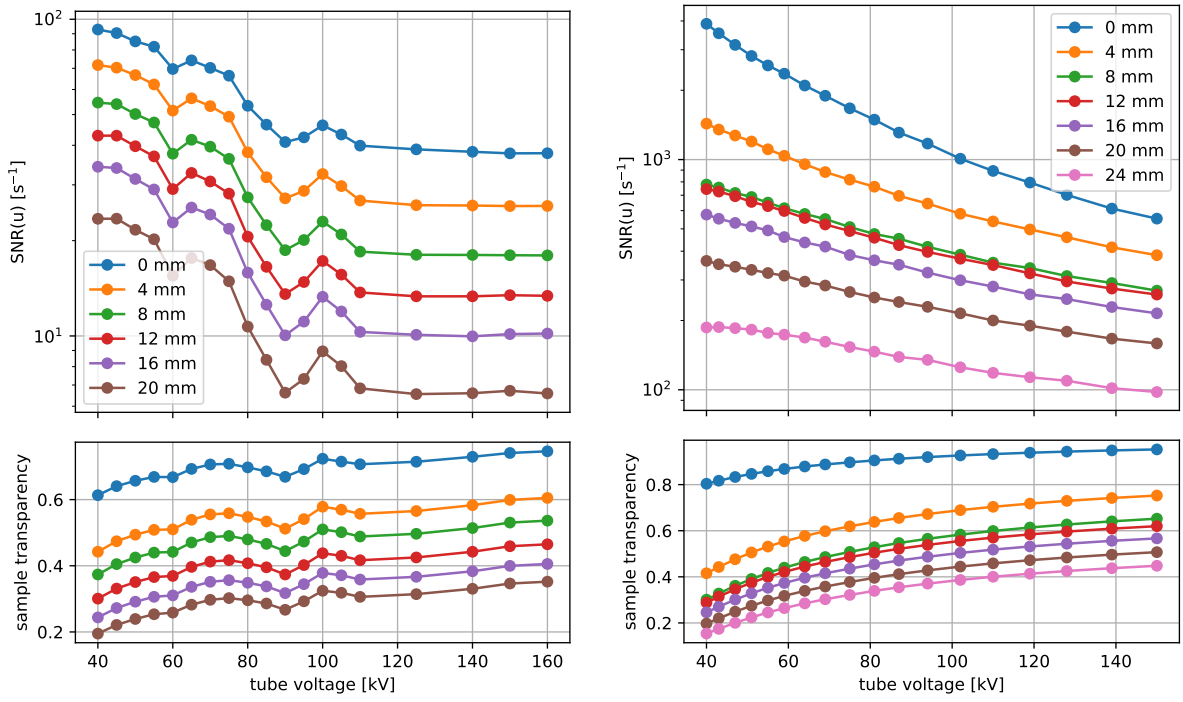

(c) C material, Si contrast @ MetRIC

(d) C material, Si contrast @ CT500

Figure 4.15.: Values of the SNR spectra averages and sample transparencies for different tube voltages for the two materials of the step wedges: aluminium (top) and plastic (bottom). Setups: MetRIC (left) and CT500 (right). In both cases, the material interface is mainly Si to air. Note that the absolute SNR values of the two setups differ by a constant factor due to component differences and source-detector distance.

different tube voltages on the x-ray source. Tube power was kept constant at 20.0 W (MetRIC) and 18.0 W (CT500) (thermally limited source), which means that the target current of the tube was adjusted to satisfy:

$$P_{\text{tube}} = U_{\text{tube}} I_{\text{target}} = \text{const.} \tag{4.15}$$

A test phantom as desribed in fig. 4.1 was used, two step wedges with materials aluminium and plastic (4 mm step thickness) were each combined with sandpaper as structure. Examples for the acquired projection images are shown in fig. 4.13. Both step wedges were placed beside each other and measured consecutively. Otherwise, the setup geometry was identical for all measurements. The material thicknesses in the step wedge represent different sample thicknesses, while the material interface of interest is silicon to air in both cases. For the MetRIC pixelsizes were determined by registering two measured projection images (horizontally shifted by 10 mm), resulting in $l_{\text{PS}} = 39.7\,\mu\text{m}$ for the aluminium wedge and $l_{\text{PS}} = 39.3\,\mu\text{m}$ for the plastic wedge. While this is not the optimal magnification for $SNR(u)$, the large field of view was required for the size of step wedge used.

SNR measurements were acquired for a set of 21 tube voltages. The detector exposure time was 100 ms (MetRIC) and 320 ms (CT500) and 50 projections were aquired per SNR measurement. 12 regions (6x aluminium and 6x plastic) were evaluated for every tube voltage, resulting in 252 measured $SNR(u)$ curves (one additional thickness at the CT500). At the MetRIC, some measurements were unusable because the measurement software did not execute a sample movement command (3 for aluminium and 2 for plastic). An example set of $SNR(u)$ curves for one thickness and one tube voltage is shown in fig. 4.14. At the spatial sizes of interest ($< 250\,\mu\text{m}$), changing the tube voltage mainly scales the whole SNR curve. This coarse structure size was chosen because the measurement error was sufficiently low at all combinations of tube voltages and material thicknesses only for the coarser structure sizes.

Two K absorption edges of materials are important here: The one for tungsten (W, source target material) at 69.53 keV (emission line) and the one for gadolinium at 50.24 keV (Detector at the MetRIC) or 35.98 keV (Detector at the CT500).

Measured $SNR(u)$ values are shown in fig. 4.15 for different tube voltages. To achieve a high data quality for all sample thicknesses, SNR spectra were averaged over spatial sizes of 150 µm to 250 µm. The higher spatial frequencies would be able to show MTF differences in addition to contrast/intensity differences, but have too high measurement errors for the higher thicknesses (signal artifacts due to low $S(u)$).

The results for the plastic wegde show a clear preference for low tube voltages (40 kV or 45 kV). For the aluminium wedge, the 4 mm sample thickness has its image quality optimum at 45 kV. Higher tube voltages are preferable for the higher sample thicknesses (70 kV for ≥ 8 mm Al). Local maxima in the $SNR(u)$ curves appear around 70 kV and 100 kV. The first can be explained by a significant portion of the x-ray spectrum lying above the absorption edge of the detector. For the second maximum, no reason comes to mind, as its energy level is above any absorption edges in the relevant materials.

From the standpoint of SNR optimization, the exact reasons for the shape of the SNR curve are not important — simply selecting the maximum of $SNR(u)$ results in the best image quality. As a general trend, thinner samples benefit from lower tube voltages (as one would expect). On the other hand, thicknesses of ≥ 12 mm Al show a general trend of increasing image quality for higher tube voltages. The specific results are also influenced by the choice of materials for the test phantom. A possible corresponding use case for the plastic step wedge is the detection of small aluminium particles embedded in organic material or plastic components. For the aluminium step wedge, the use case is e.g. the detection of cracks/voids in solid aluminium.

The measurements from the MetRIC show surprisingly strong peaks/valleys in the $SNR(u)$ curves, they are less pronounced for the plastic step wedge. In the most extreme case, a tube voltage of 70 kV yields a $SNR(u)$ three times as high as at 90 kV (e.g. 12 mm Al). While this difference may be caused by some peculiar (technical) problem with the setup, it is real and needs to be taken into account for an image quality optimization. Measurements from the CT500 do not show similar peaks/valleys.

There are cases where for the same SNR, very different sample transparencies appear. For 16–20 mm Al, tube voltages of 45 kV and 160 kV have similar SNR, but the higher voltage has a transparency 10 times higher. In the first case, this SNR is achieved by a high contrast but a low intensity. In the latter, the reverse is the case. The latter case also has less beam hardening and might thus be preferable from a standpoint of

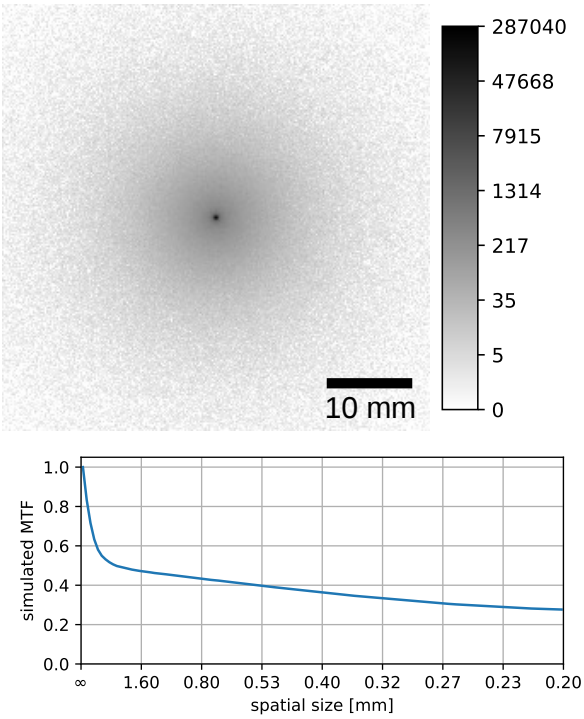

Figure 4.16.: Example for a simulated PSF (top) and derived MTF (bottom) that is caused by the addition of the detector side filter to the detector setup (here: 1 mm tungsten). The intensity gain of the detector side filter is approximately given by $1/\mathbf{h}(u_{ny}) \approx 4$, as the non-scattered intensity is given by the delta-peak in the center of the PSF.

image artifacts. Real samples usually have a range of sample thicknesses where a high image quality is required—the optimal tube voltage for the whole sample might thus be a compromise between different optima.

4.2.6. Detector side filters

The EMECT project was co-funded by the german DFG[2] and the swiss SNF. Its aim was to use detector side attenuation filters to improve the detection efficiency in high-energy (MeV) x-ray imaging. The basic idea is that the scattered radiation originating from a thin plate of highly absorbing material placed directly in front of the active area of the detector is detected as additional intensity. Because of the Compton shift reduced the energy of the scattered radiation, the absorption efficiency of the detector is higher. X-ray detectors generally have very poor absorption efficiencies at x-ray energies in the MeV range and simulations done by Carina Stritt (EMPA) [57] showed that the detected intensity can be increased by for example a factor of 4 this way (dependent on the material of the detector side filter).

[2]Geschäftszeichen: HA2904/2-2

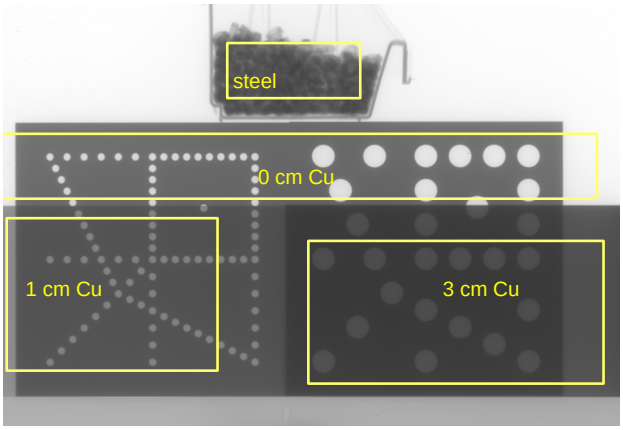

Figure 4.17.: Example image for the SNR measurements for the EMECT project. The different evaluation regions are marked in yellow. They correspond to different thicknesses of Cu plates placed before the steel test phantoms. Compare to fig. 4.1. At the top, a container with steel screws was placed.

Different measurements were performed for the EMECT project at the XXL-CT at the Fraunhofer EZRT in Fürth in cooperation with Richard Schielein and Nils Reims. The detector used was a Perkin Elmer XRD 1620 AN1 and the LINAC was operated at 7.5 MeV. Detector pixelsize is 200 µm and voxelsize was 181 µm.

As part of these measurements, SNR spectra measurements were performed to find out if the intensity gain from the detector side filters produces a corresponding image quality gain. Presented here are only the results of these measurements insofar as they concern the topic of x-ray image quality.

The simulations of the PSF/MTF are shown in fig. 4.16 (simulated without sample absorption). It is clearly visible that the additional intensity is heavily blurred. The high blurring is in part caused by the distance between the outer detector casing and the scintillator (geometrical spreading of x-rays). Tungsten plates of thicknesses 0.5 mm and 1.0 mm were used as detector side filters, all measurements were also performed without detector side filters. Measurements of the SNR spectra were performed on a test phantom (see fig. 4.17) consisting of perforated steel plates combined with copper plates of different thicknesses (without, 1 cm Cu and 3 cm Cu). As a fourth

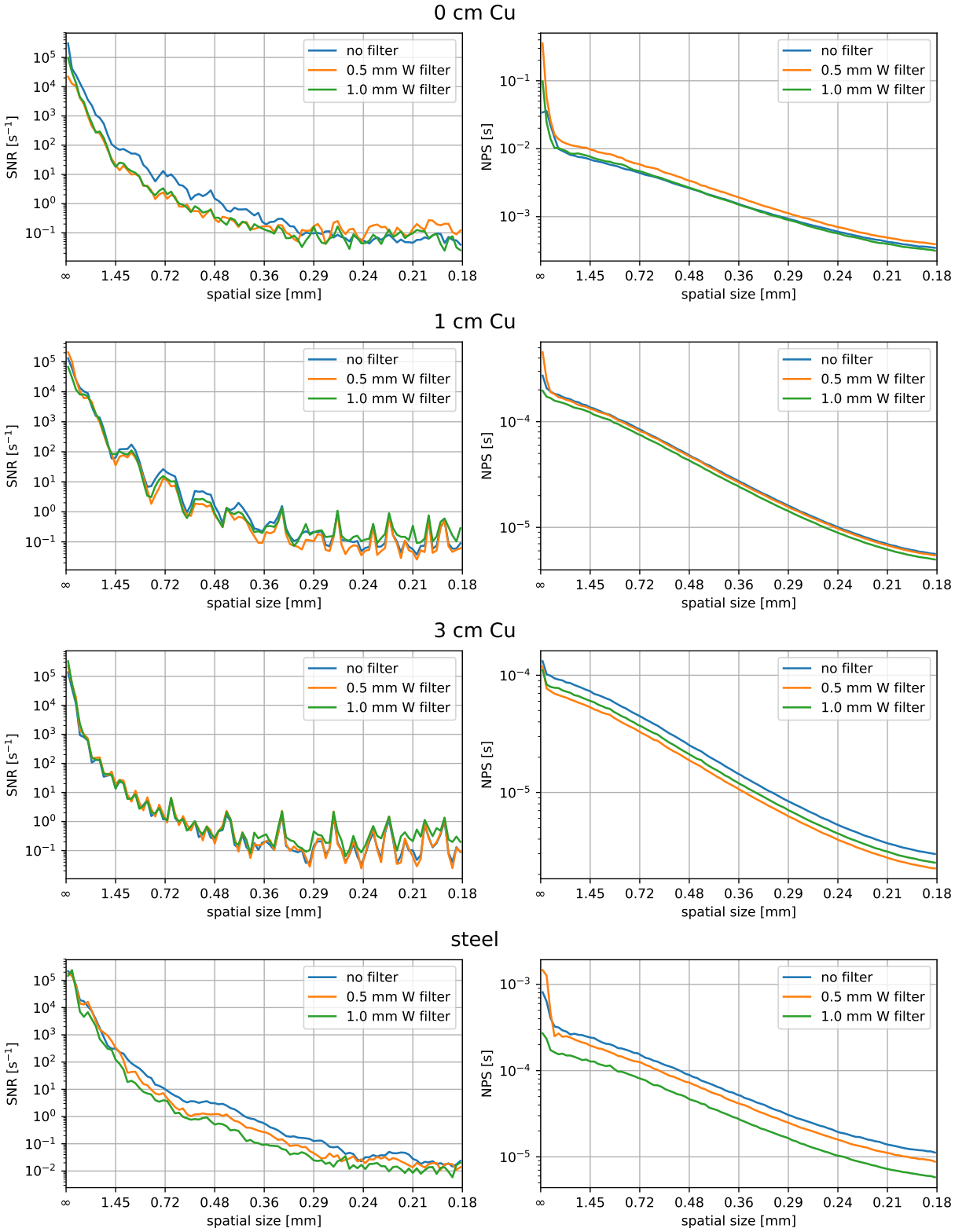

Figure 4.18.: SNR spectra measurement results (left) and noise spectra (right) for the different detector side filters in the EMECT project, top to bottom are different regions with different sample thicknesses. The different regions are shown in fig. 4.17. Due to radiation damage to the detector, SNR measurements show signal artifacts below 0.4 mm spatial size, useful data is therefore restricted to the left half of the SNR curves.

region, plastic container with steel screws was used.

The results are shown in fig. 4.18. If we consider the fact that adding a heavily blurred image should decrease the SNR spectrum (see section 3.4), the SNR measurements for thin samples (0 cm Cu and steel regions) confirm this expectation. For the thicker samples, this trend becomes weaker and in the region with the thickest sample the difference becomes negligibly small. As no simulations of the MTF were performed for thicker samples (different spectra), the expected effect of the detector side filter for thicker samples is unknown. The detector used has many dead pixels due to radiation damage and the SNR measurements show severe signal artifacts that could not be corrected fully.

The peak in the measured noise power spectra at the spatial frequency of zero corresponds to the indirect detection process of the detector side filter (see section 3.7 and compare to fig. 4.16). It becomes less pronounced for thicker test phantoms, which can be interpreted as the detector side filter having a weaker effect on the detected intensity. This peak is also stronger for 0.5 mm W than for 1.0 mm W, which would mean that the thicker filter absorbs a significant part of the additional intensity generated. The measurements without detector side filter also show this peak, which means that the x-ray scattering in the detector material (e.g. casing) itself is also significant.

The important facts are the following:

- It is confirmed here that an increase in intensity does not automatically translate to a higher image quality if the signal strength of the additional intensity is low (here: bad MTF). For the larger structure sizes, the detector side filter does produce the expected gain because there the MTF is good.
- The usefulness of the detector side filter depends heavily on the sample thickness and the corresponding transmitted x-ray spectrum.
- Detector side filters appear to produce an additional unidentified effect which increases the SNR. This effect becomes stronger for thicker samples and may in part be scattered radiation which is absorbed in the detector side filter—this is a physical reduction of noise. At higher sample thicknesses, this effect would probably be stronger than the decrease and the detector side filter may then achieve the original aim of increasing the image quality. CT measurements with thicker samples measured on the same setup seem to confirm this fact, but there were no SNR spectra measurements performed for this higher thicknesses.

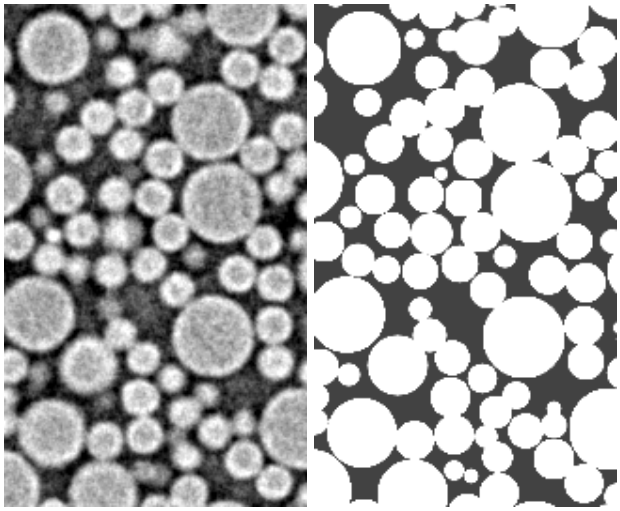

Figure 4.19.: Image slices of the 3D volumes with the CT reconstructed volume (left) and computed object shape (right) for the DE evaluation. The area shown is 0.3x0.5 mm.

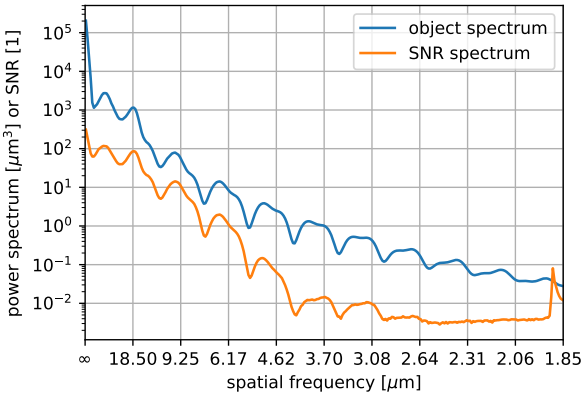

Figure 4.20.: Object spectrum computed from the object shape, see fig. 4.19 (right) and SNR spectrum determined from the 10 CT measurements. The maxima/minima correspond to the higher harmonics of the ball diameters. For the SNR spectrum, signal artifacts appear at $\approx 3 \cdot 10^{-3}$, so the lowest SNR values are artificial. At a structure size of 4 µm and coarser, the signal artifacts do not play a role. The peak at ≈ 1.9 µm is artificial.

property	value
source	50 keV, no filters, 2 W target power
geometry	335 mm source to detector distance, magnification 40
exposure time	400 ms per image, 0.333 hours per CT (only exposure times are counted)
number of projections	3000 per CT, 10 CTs (acquired as 3000 views with 10 projections per view)
test phantom	1:1 weight mix of 38 μm and 80 μm diameter PMMA balls, 2 mm diameter container of glass with 20 μm wall thickness.

Table 4.5.: Measurement parameters for the DE measurement at the MetRIC.

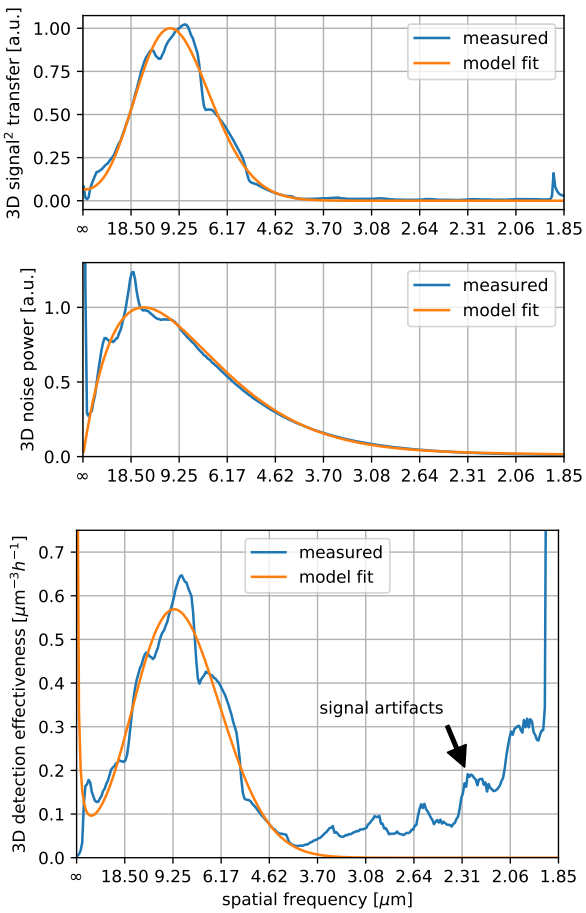

Figure 4.21.: Measured system signal transfer (top) and noise power spectrum (middle) and resulting $DE(u)$ (bottom) determined from the 3D SNR spectrum and the object spectrum. Both the measured data and the model fits are shown. The $DE(u)$ was normalized to a cumulative exposure time of one hour per CT. Deviations between measurement and fit at structures smaller than 4 μm are caused by signal artifacts in the SNR spectra measurement, the real $DE(u)$ is close to zero in this range.

4.3. Application in 3D

Measuring the SNR spectrum for a CT image requires that several CT images of the same object are acquired. In high-resolution x-ray imaging, this needs to be done with an acquisition of several images directly after each other for every CT view. If the thermal and mechanical instabilities are too high, acquiring several whole CT scans after each other would lead to shifts in the CT images. Such differences would produce artifacts in the SNR spectra measurement.

These projections need to be reconstructed into individual CT images, where all first, all second, ... projections are treated as one CT scan. Then, eq. (4.8) can be applied for a volume image series. Therefore, power spectra are computed from volume images. As in 2D, it is convenient to radially average in 3D, even though the CT reconstruction does add anisotropy to the volume image (ramp filter in xy).

The result is a 3D SNR spectrum. For a more reliable and comparable image quality evaluation, this procedure can be combined with an object spectrum determination to generate a DE spectrum (see section 4.1.5).

4.3.1. Measurement procedure

A first test of the procedure to measure the DE spectrum was performed at an in-house CT system (MetRIC), the parameters used are listed in table 4.5. Its purpose was to test if the proposed procedure works well in practice. The determination of the object spectrum was performed as described in section 4.1.6 and image slices from the CT volume are shown in fig. 4.19. Figure 4.20 shows the resulting object spectrum and the SNR spectrum computed from the 10 CT images. The object spectrum $P(u)$, the signal power spectrum $S_{3D}(u)$ and the noise power spectrum $N_{3D}(u)$ are the measured quantities which are used in the following to compute intermediate results and the $DE(u)$.

The squared 3D signal transfer is the transfer function from the object power spectrum to the signal power spectrum, see section 3.4.2 on page 39. It was fitted according to the following equation:

$$\frac{S_{3D}(u)}{P(u)} = \left[I\kappa_{abs}(1+p^2u^2)\mathbf{h}_S(u)\right]^2 \mathrm{sinc}(u)^{3.4} \quad (4.16)$$

where p is the phase contrast strength, relative to κ_{abs}, the absorption signal strength, $\mathbf{h}_S$ is modeled according to eq. (3.67) and the last part is explained in section 2.4. The signal MTF $\mathbf{h}_s$ is modeled as a part of the signal power spectrum according to eq. (3.32) and eq. (3.34) on page 41. $I\kappa_{abs}$ is treated as a single fit parameter—it corresponds to the term $\sum_E I(E)\kappa(E)$ in eq. (3.34). Note that the equations in the theory part refer to non-normalized images and this evaluation to normalized images.

The noise power spectrum was fitted using the same basic models which combine to:

$$\mathbf{N}_{3D}(u) = I\left(c + c^2\mathbf{h}_N(u)^2\right) u\,\mathrm{sinc}(u)^{3.4} \quad (4.17)$$

See section 3.7 and eq. (3.92) for an explanation of the first part. Both fits and the corresponding measured data are shown in fig. 4.21 and the fraction of both gives the $DE(u)$:

$$DE(u) = \frac{S_{3D}(u)}{P(u)N_{3D}(u)} = \frac{\left[I\kappa_{abs}(1+p^2u^2)\mathbf{h}_S(u)\right]^2}{Iu\left(c + c^2\mathbf{h}_N(u)^2\right)} \quad (4.18)$$

The resulting DE spectrum was computed from the object spectrum and the SNR spectrum and is shown in fig. 4.21. The model fit for the $DE(u)$ is computed from the two prior model fits according to the equation above.

As can be seen from the plots, this setup has an optimal image quality at $\approx 10\,\mu$m for this application and the highest achievable resolution is limited to $> 3\,\mu$m. The noise power spectrum shows some noticeable deviations between the fit and the measurement: (1) at u=0, the measured spectrum has a peak which is probably caused by some reconstruction artifact or ring artifacts (2) at roughly $17.5\,\mu$m there is a significant artificial peak in the NPS, this is probably caused by a slight mismatch of the corresponding peaks in the object spectrum and SNR spectrum (see fig. 4.20).

4.3.2. Micro CT round robin study

The round robin study [3] was organized by S. Zabler, used the SNR spectra measurement method introduced here and was evaluated by me using methods described in this work. Its aim was a quantitative performance comparison of different sub-μ CT scanners in practice. For the details refer to the publication, I will summarize the study design here.

The original aim was to compare the image quality of different (inline) phase contrast imaging devices. Different machines at various scientific institutions and from different manufacturers as well as three machines built in our group took part in the study. Measurement parameters were chosen by the machine operators who usually do measurements on the machines—the image quality determined is therefore the one the machine will produce in practice. Determining the image quality of CT images was the aim, therefore CT scans of comparable test phantoms were performed at all devices. The test phantoms consisted of a mixture of PMMA balls in glass cylinders with a diameter of 1 mm and $20\,\mu$m wall thickness.

Ideally, it would have been possible to apply the measurement scheme and evaluation as described before. Due to limitations in the machine control software, it was impossible to acquire a CT scan with several images per view, as would have been necessary for 3D SNR spectra measurements.

The evaluation was performed as described in the section before where possible, the system signal transfer and noise power spectra were instead produced by a fit to the data spectrum of the CT images.

Additionally, SNR spectra measurements of the same test phantom were done in 2D.

5. Conclusions

Different use cases

The technical capabilities of different x-ray imaging setups vary greatly. The samples are also very different: Imaging e.g. a 100 µm thick metallic sample at 100 nm resolution or a 500 mm organic sample at 500 µm resolution requires very different setups.

High resolution x-ray imaging (typical sampling $<$ 5 µm) generally uses lower energies (e.g. $<$ 10 keV) due to the higher x-ray transparency of thinner samples. Detecting smaller structures also intrinsically requires a higher *SNR*. The signal in high resolution x-ray imaging mainly consists of photoabsorption and phase contrast. In low resolution x-ray imaging, larger samples are investigated. They require higher x-ray energies. For the latter, Compton scattering produces a significant part of the attenuation signal.

Within the range of x-ray imaging applications, medical imaging represents a very narrow range. Models for image quality which may be appropriate for these cases can be inappropriate in a different context, e.g. in material science. Imaging scientists may therefore need to use models different from those used in medical imaging (e.g. DQE).

SNR spectra can be used to optimize image quality including phase contrast effects [8, 1], see also section 2.1.2 on page 10. The latter can be interpreted as a physical highpass filter [11]. For x-ray imaging setups with (sub-)micrometer resolution, phase contrast is often the strongest contribution to the detected signal.

If one imaging device is used for imaging very different samples, some compromise must be made on the setup components. Also, if one sample has very different attenuation lengths along the beam direction, a compromise must be made to optimize image quality for the corresponding different x-ray spectra.

It is not possible to derive general rules that apply to every case. For any specific use case, optimizing the *SNR* spectrum by measurements is required. For a set of similar use cases, one can derive general rules. Such a set can e.g. be imaging with a photoabsorption signal and a bremsstrahlung source. A general rule in this example is the fact that only lower x-ray energies contribute to image quality while higher energies deteriorate it. Additionally, simulations are an important method to discover ways in which an imaging setup may be optimized.

Structure size

Using *SNR* spectra implies that sample structure (of a specific size) is of interest. Because $SNR(u)$ usually strongly decreases to higher u (smaller structures), larger structures are always detected well in a specific imaging measurement. Smaller structures can only be detected down to a minimal size ("spatial resolution") which is given by the properties of the setup and the measurement configuration. As a trivial example, increasing the measurement time allows to resolve smaller details.

Depending on the structure size of interest, different imaging setups may be optimal. This fact is modeled well by *SNR* spectra. Optimal detection depends on what is intended to be detected, which in itself is a decision which needs to be made by the person doing the investigation.

Optimizing imaging setups

Designing a good imaging setup or operating it well is conceptually different in a polychromatic use case than in a monochromatic use case. For monochromatic imaging, an optimal setup generates the highest possible intensity and detects all photons. In the polychromatic case one can apply an energy weighting (e.g. CEW) and detecting or generating less photons may increase the *SNR*.

If optimal energy weighting is not possible, then the optimal polychromatic setup needs to detect as many photons as possible from some photon classes and no photons from the other photon classes, see eq. (3.43). Depending on the differentiating criterion, this may be very difficult to achieve. While a detector can be designed to less efficiently detect x-ray photons of a specific energy range, this is much more difficult for x-ray photons that were absorbed at a position in the

screen where the MTF is worse (e.g. higher distance from the focus plane).

Direct x-ray detectors which can set an upper limit to the x-ray energy of the counted detection events are ideally suited for DEW. Setting the upper limit in such a way that photons with comparatively low *SDS* are not counted may potentially result in a large increase in *SNR* (see fig. 3.14).

For an indirect detector, the *SNR* can be increased by choosing a thinner screen for lower energy imaging – even if the absorption efficiency at the relevant energy range may then be slightly lower (see fig. 3.15). This effect is separate from the better MTF of the thinner screen. In many imaging setups, the screen is already thin enough for its use cases due to technical limitations or MTF considerations.

Testable predictions

An image quality optimization based on *SNR* spectra makes predictions which can be tested directly. This is done with a direct measurement, see chapter 4 or [1] for a method. A *SNR* optimization should ideally be based on measurements for the specific use case. Using simulations instead requires that the simulation method was thoroughly tested with direct measurements on the same or a sufficiently similar device. This makes it possible to notice errors in the theory or in the assumptions made, which is a basic requirement if one wants to rely on such a model [58].

Concerning *DQE*, note that optimizing *SNR* may lead to a different optimal setting than optimizing polychromatically averaged *DQE*. This difference stems from the fact that a *DQE* analysis effectively assumes monochromaticity.

A model can both be tested by physical measurements and also by checking if it is without internal contradictions. Here, internal contradictions mainly mean that the model does not actually describe what it is supposed to describe. This is for example the case when temporal *SNR* is used to describe image quality.

Application-specificity

It would be desirable to describe the performance of an x-ray imaging device independently from the application case. As we have seen, it depends on the application case if this is possible. The special case in which the signal strength κ is (approximately) independent of the x-ray energy is the only such case.

In all other cases, the image quality is fundamentally dependent on the sample used—while on the same imaging setup a sample with predominantly low atomic number materials may satisfy the special case, a denser sample may not. Any realistic model for image quality therefore must consider the possibility that image quality is application-specific. Special models for non-application-specific cases *must* always clearly state the approximations used and where this model can be applied.

The models and methods described in this work are highly application specific. Nonetheless, if different use cases have a very similar imaging performance, even such an application specific method will yield similar results. Conversely, measuring the performance for one of these similar use cases may be representative for the others.

Extension to x-ray optics

The theory and methods presented here should be applicable to any imaging technique where the signal power spectrum can represent the information gathered by the measurement. Examples for such techniques are grating based interferometry and imaging with x-ray (diffraction) lenses. Even though the physics of image formation are very different from the imaging techniques analyzed in this work, both the theory and the measurement method for SNR spectra should work similarly well.

In both cases, the image formation is a much more complex process than e.g. for attenuation imaging. Directly measuring the resulting SNR spectra or signal and noise power spectra of different setups could therefore be even more useful than for simpler imaging techniques. Other use cases where additional aspects influence image quality (e.g. x-ray scattering noise) also benefit fr

Optimization instead of standardization

Optimizing image quality instead of standardizing the imaging device implies fundamentally different approaches. Sample properties and interactions between sample and the imaging device or between parts of the imaging device influence image quality. For the optimization, including these is a natural aspect and the model developed here does include them. Standardization excludes the sample influence and the device interactions, which is necessary if the aim is

to describe a device (or a single part of one). As we have seen, these simplifications can lead to a loss of accuracy.

Measurements

Measuring SNR spectra with the method proposed in this work (see chapter 4) is qualitatively different from prior work. Instead of measuring several different quantities (MTF, NPS, ...) with different methods, one quantity is determined by a single measurement. This one quantity includes all the effects of the different quantities. Thereby, interactions between parts of the experimental setup are represented correctly in the measurement result. For the aim of x-ray image quality optimization, the new approach is both simpler and more reliable. Such a measurement is also more complete, as it includes more physical effects than the sum of the different quantities.

Additionally, SNR spectra measurements can be performed on the actual sample on which the imaging measurement will be performed. This could enable an automated optimization of device parameters for a specific sample.

Normalizing the SNR spectrum with respect to the object spectrum $P(u)$ can be done by measuring $P(u)$ and dividing $SNR(u)$ by it. This procedure preserves the completeness and reliability of the SNR spectra while removing one specific influence. The resulting $DE(u)$ allows a comparison of different experimental setups on an absolute scale.

This difference can be made clear by comparing $DE(u)$ and CNR_{NDT}. While the two quantities are effectively identical for a monochromatic imaging theory, they differ fundamentally in how polychromaticity is represented and in how they are measured. CNR_{NDT} is defined as a combination of device parameters with the contrast of the sample. This approach means that a set of simple properties is combined, and the result is meant to describe image quality. The $DE(u)$ on the other hand is derived from a complete model ($SNR(u)$) that is simplified (normalized) by measuring an additional quantity ($P(u)$). The $DE(u)$ approach makes it much easier to understand what the physical model does *not* represent—only the effects modeled by $P(u)$.

Seen another way, the $DE(u)$ approach makes sure that only physical effects we do not want to represent are removed from the model. The other way is to only add effects we consider necessary to the model. We can see e.g. in section 3.6 that the latter approach may accidentally not include effects, which can lead to wrong conclusions. Making such an error is much more improbable with the measurement method introduced in this work.

6. Summary

The SNR spectra model and measurement method developed in this work yield reliable application-specific optima for image quality. This optimization can either be used to understand image quality, find out how to build a good imaging device or to (automatically) optimize the parameters of an existing setup.

SNR spectra are here defined as a fraction of power spectra instead of a product of device properties. In combination with the newly developed measurement method for this definition, a close correspondence between theory and measurement is achieved. Prior approaches suffer from a focus on theoretical definitions without fully considering if the defined quantities can be measured correctly. Additionally, discrepancies between assumptions and reality are common.

The new approach is more reliable and complete, but also more difficult to evaluate and interpret. The signal power spectrum in the numerator of this fraction allows to model the image quality of different contrast mechanisms that are used in high-resolution x-ray imaging. Superposition equations derived for signal and noise enable understanding how polychromaticity (or superposition in general) affects the image quality.

For the concept of detection energy weighting (section 3.4.6), a quantitative model for how it affects image quality was found. It was shown that—depending on sample properties—not detecting x-ray photons can increase image quality (eq. (3.43)). For optimal computational energy weighting (section 3.4.6), more general formula for the optimal weight was found, eq. (3.51). In addition to the signal strength, it includes noise and modulation transfer.

The novel method for measuring SNR spectra makes it possible to experimentally optimize image quality for different contrast mechanisms. This method uses one simple measurement to obtain a measure for image quality for a specific experimental setup. Comparable measurement methods typically require at least three more complex measurements, where the combination may then give a false result. SNR spectra measurements can be used to:

- Test theoretical predictions about image quality optima (section 4.2.2).
- Optimize image quality for a specific application (sections 4.2.1 and 4.2.5).
- Find new mechanisms to improve image quality (section 4.2.4).

The last item reveals an important limitation of x-ray imaging in general: The achievable image quality is limited by the amount of x-ray photons interacting with the sample, not by the amount incident per detector area (see section 3.6). If the rest of the imaging geometry is fixed, moving the detector only changes the field of view, not the image quality. A practical consequence is that moving the sample closer to the x-ray source increases image quality quadratically.

The results of a SNR spectra measurement represent the image quality only on a relative scale, but very reliable. This relative scale is sufficient for an optimization problem. Physical effects are often already clearly identifiable by the shape of the functional relationship between input parameter and measurement result.

SNR spectra as a quantity are not well suited for standardization, but instead allow a reliable optimization. Not satisfying the requirements of standardization allows to use methods which have other advantages. In this case, the SNR spectra method describes the image quality for a specific application. Consequently, additional physical effects can be taken into account. Additionally, the measurement method can be used to automate the setting of optimal machine parameters.

The newly proposed image quality measure detection effectiveness ($DE(u)$, eq. (3.31)) is better suited for standardization or setup comparison. This quantity is very similar to measures from other publications (e.g. $CNR_{\mathrm{NDT}}(u)$), when interpreted monochromatically. Polychromatic effects can only be modeled fully by the $DE(u)$. The measurement processes of both are different and the $DE(u)$ is fundamentally more reliable.

Information technology and digital data processing make it possible to determine SNR spectra from a measured image series. This measurement process was designed from the ground up to use these technical ca-

pabilities. Often, information technology is only used to make processes easier and more exact. Here, the whole measurement method would be infeasible without it. As this example shows, using the capabilities of digital data processing much more extensively opens many new possibilities. Information technology can be used to extract information from measured data in ways that analog data processing simply cannot.

The original purpose of the SNR spectra optimization theory and methods was to optimize high-resolution x-ray imaging only. During the course of this work, it has become clear that some of the results of this work affect x-ray imaging in general. In the future, these results could be applied to MI and NDT x-ray imaging. Future work on the same topic will also need to consider the relationship between SNR spectra or DE(u) and sufficient image quality. This question is about the minimal image quality required for a specific measurement task.

Zusammenfassung

Das in dieser Arbeit entwickelte Modell und die Messmethode für SNR Spektren ergeben zuverlässige anwendungsspezifische Optima für die Bildqualität. Diese Optimierung kann verwendet werden, entweder um Bildqualität zu verstehen, um herauszufinden wie ein gutes Bildgebungsgerät gebaut werden kann oder um die Parameter eines existierenden Aufbaus (automatisch) festzulegen.

SNR Spektren als das Verhältnis von Leistungsspektren zu definieren macht dieses Modell zuverlässiger und vollständiger, aber auch schwierieger auszuwerten und zu interpretieren. In Kombination mit der neu entwickelten Messmethode für diese Definition wird eine nähere Entsprechung zwischen Theorie und Messung erreicht. Vorherige Ansätze leiden under einem Fokus auf theoretische Definitionen ohne vollständig zu berücksichtigen ob die definierten Größen korrekt gemessen werden können. Zusätzlich sind Unstimmigkeiten zwsichen den Annahmen und der Realität üblich.

Der neue Ansatz ist zuverlässiger und vollständiger, aber auch schwieriger auszuwerten und zu interpretieren. Das Signalleistungsspektrum im Zähler des Bruchs ermöglicht es, die Bildqualität verschiedener in der hochauflösenden Röntgenbildgebung verwendeten Kontrastmechanismen zu modellieren. Hergeleitete Gleichungen für die Überlagerung von Signal und Rauschen ermöglichen es zu verstehen, wie Polychromatizität (oder im Allgemeinen Superposition) die Bildqualität beeinflusst.

Für das Konzept der Detektions-Energiegewichtung (Abschnitt 3.4.6) wurde ein quantitatives Modell dafür gefunden, wie sie die Bildqualität beeinflusst. Dabei wurde gezeigt dass – abhängig von den Probeneigenschaften – es die Bildqualität erhöhen kann Röntgenphotonen nicht zu detektieren. Für die rechnerische Energiegewichtung (Abschnitt 3.4.6) wurde eine allgemeinere Formel für deren optimale Gewichtung gefunden, gl. 3.51. Diese enthält zusätzlich zur Signalstärke auch Rauschen und Modulationstransfer.

Die neue Methode zum Messen von SNR Spektren ermöglicht es, die Bildqualität für verschiedene Kontrastmechanismen experimentell auszuwerten. Diese Methode benutzt eine einfache Messung um für einen spezifischen experimentellen Aufbau ein Maß für die Bildqualität zu erhalten. Sie kann dazu verwendet werden:

- Theoretische Vorhersagen über Optima der Bildqualität zu testen (Abschnitt 4.2.2).
- Die Bildqualität für eine bestimmte Anwendung zu optimieren (Abschnitt 4.2.1 und 4.2.5).
- Neue Mechanismen zu finden um die Bildqualität zu verbessern (Abschnitt 4.2.4).

Der letzte Punkt zeigt eine allgemeine Limitierung in der Röntgenbildgebung auf: Die erreichbare Bildqualität ist begrenzt durch die Anzahl an Röntgenphotonen, die mit der Probe wechselwirken, nicht durch die Anzahl der Photonen die pro Detektorfläche auftreffen (siehe Abschnitt 3.6). Wenn die restliche Bildgebungsgeometrie fest bleibt, dann verändert sich bei einer Bewegung des Detektors nur das Sichtfeld, nicht die Bildqualität. Eine praktische Konsequenz ist, dass die Bildqualität erhöht wird, wenn die Probe näher an die Röntgenquelle bewegt wird.

Das Ergebnis einer Messung eines SNR Spektrums gibt die Bildqualität nur auf einer relativen Skala wieder, ist aber sehr zuverlässig. Die relative Skala reicht für ein Optimierungsproblem aus. Physikalische Effekte können oft aus der Form der funktionellen Abhängigkeit zwischen Eingabeparameter und Messergebnis eindeutig erkannt werden.

SNR Spektren als Größe sind nicht gut geeignet für Standardisierung, aber stattdessen ermöglichen sie eine zuverlässige Optimierung. Die Anforderungen an Standardisierung nicht zu erfüllen, erlaubt es, Methoden zu verwenden, die andere Vorteile haben.

In diesem Fall beschreiben die SNR Spektren die tatsächliche Bildqualität für eine spezifische Anwendung. Deshalb können zusätzliche physikalische Effekte berücksichtigt werden.

Das neu vorgeschlagene Bildqualitätsmaß Detektionseffizienz ($DE(u)$, gl. 3.31) eignet sich besser für die Standardisierung oder den Vergleich verschiedener Aufbauten. Diese Größe ist Maßen aus anderen Publikationen ähnlich (z.B. $CNR_{\mathrm{NDT}}(u)$), wenn sie monochromatische interpretiert wird. Polychromatische Effekte können nur durch die $DE(u)$ vollständig modelliert werden. Die Messmethoden für beide sind grundsätzlich verschieden, da die $DE(u)$ die Anwendungsabhängige Bildqualität darstellt.

Informationstechnologie und digitale Datenverarbeitung ermöglichen es, SNR Spektren aus einer Messung einer Bildserie zu bestimmen. Der Messprozess wurde von Grund auf entwickelt um diese technischen Möglichkeiten zu nutzen. Oft wird die Informationstechnologie nur benutzt um bekannte Prozesse einfacher und exakter zu machen. Hier wäre der gesamte Messprozess ohne diese unrealistisch. Wie dieses Beispiel zeigt, eröffnet eine umfangreichere Nutzung der digitalen Datenverarbeitung neue Möglichkeiten. Informationstechnologie kann auf eine Art und Weise Informationen aus gemessen Daten extrahieren, die mit analoger Datenverarbeitung nicht möglich ist.

Der ursprüngiche Zweck der Theorie und Methoden zu Optimierung von SNR Spektren war es, die Bildqualität nur für die hochauflösende Röntgenbildbebung zu optimieren. Während der Durchführung dieser Arbeit wurde klar, dass einige der Ergebnisse die Röntgenbildbebung allgemein betreffen. Diese Ergebnisse könnten in der Zukunft auch für MI und NDT Röntgenbildgebung angewendet werden. Zukünftige Arbeit zum gleichen Thema muss auch den Zusammenhang zwischen SNR Spektren oder DE(u) und hinreichender Bildqualität betrachten. Diese Frage betrifft die minimal nötige Bildqualität für eine bestimmte Messaufgabe.

Acknowledgments

Randolf Hanke is thanked for making it possible to do the thesis work at the Chair for X-Ray Microscopy. I would especially like to thank Simon Zabler for doing the main work in guidance and supervision. I would also like to thank the colleagues with whom I worked together for specific measurements: Andreas Balles, Christian Fella and Fabian Lutter.

Glossary

abbreviation	equation/section	description
CNR_t	eq. (3.4)	contrast to noise ratio
CNR_{NDT}	eq. (3.5)	contrast to noise ration which includes modulation transfer and noise power spectra effects
CEW	section 3.4.6	computational energy weighting, weighting after detection (requires energy-resolving detector)
DEW	section 3.4.6	detection energy weighting, weighting before detection (effective x-ray spectrum)
DE(u)	eq. (3.31)	detection effectiveness (normalized SNR spectrum)
IPC	section 2.1.2	inline phase contrast
MTF	eq. (2.12)	modulation transfer function
SDS	eq. (3.45)	signal detection strength
SNR_t	eq. (3.17)	(temporal) signal to noise ratio (property of one image pixel)
SNR(u)	eq. (3.30)	signal to noise ratio spectrum (property of an image area)

Bibliography

[1] M. Ullherr et al. “Using measurements of the spatial SNR to optimize phase contrast X-ray imaging”. In: *Nucl Instr Meth A* 877 (2018), pp. 44–50. DOI: 10.1016/j.nima.2017.09.044.

[2] M. Ullherr and S. Zabler. “SNR spectra as a quantitative model for image quality in polychromatic X-ray imaging”. In: *Nucl Instr Meth A* 943 (2019), p. 162385. ISSN: 0168-9002. DOI: 10.1016/j.nima.2019.162385. URL: https://arxiv.org/abs/1904.13313.

[3] S. Zabler et al. “Comparing image quality in phase contrast submu X-ray tomography—A round-robin study”. In: *Nucl Instr Meth A* (2019), p. 162992. ISSN: 0168-9002. DOI: 10.1016/j.nima.2019.162992. URL: https://arxiv.org/abs/1905.02651.

[4] M. Ullherr and S. Zabler. “Correcting multi material artifacts from single material phase retrieved holo-tomograms with a simple 3D Fourier method”. In: *Optics Express* 23.25 (2015), pp. 32718–32727. DOI: 10.1364/OE.23.032718.

[5] S. Zabler et al. “Characterization of aluminum alloy microstructures by means of synchrotron X-ray micro-tomography – a simple toolchain for extracting quantitative 3D morphological features”. In: *Int. J. Mater. Res.* 110 (2019). DOI: 10.3139/146.111854.

[6] W. C. Röntgen. “Uber eine neue Art von Strahlen”. In: *Sitzungsber Phys Med Ges Wurtzburg* 9 (1895), pp. 132–141.

[7] M. Born and E. Wolf. *Principles of Optics*. Cambridge University Press, 1999.

[8] D. M. Paganin. *Coherent X-Ray Optics*. Oxford University Press, 2006. ISBN: 9780199673865.

[9] P. Cloetens et al. “Holotomography: Quantitative phase tomography with micrometer resolution using hard synchrotron radiation x rays”. In: *Appl. Phys. Lett.* 75.19 (1999), pp. 2912–2914. DOI: 10.1063/1.125225.

[10] T. Weitkamp et al. “ANKAphase: software for single-distance phase retrieval from inline X-ray phase-contrast radiographs”. In: *Journal of synchrotron radiation* 18.4 (2011), pp. 617–629. DOI: 10.1107/S0909049511002895.

[11] D. Paganin et al. “Simultaneous phase and amplitude extraction from a single defocused image of a homogeneous object”. In: *J Microsc* 206.1 (2002), pp. 33–40. DOI: 10.1046/j.1365-2818.2002.01010.x.

[12] R. Bracewell. *The Fourier Transform and Its Applications*. McGraw-Hill, 1986. ISBN: 0-306-48187-1.

[13] H. Fujita et al. “A simple method for determining the modulation transfer function in digital radiography”. In: *IEEE Transactions on Medical Imaging* 11.1 (Mar. 1992), pp. 34–39. DOI: 10.1109/42.126908.

[14] E. Jaynes. *Probability Theory – The Logic of Science*. Ed. by G. L. Bretthorst. Cambridge Univ. Press, 2003.

[15] R. T. Cox. *The Algebra of Probable Inference*. The Johns Hopkins Press, 1961.

[16] T. A. Enßlin and M. Frommert. “Reconstruction of signals with unknown spectra in information field theory with parameter uncertainty”. In: *Physical Review D* 83.10 (May 2011). DOI: 10.1103/PhysRevD.83.105014.

[17] C. Gardiner. *Stochastic Methods: A Handbook for the Natural and Social Sciences*. Springer, 2009.

[18] N. Wiener. *Extrapolation, interpolation, and smoothing of stationary time series*. MIT Press, 1949.

[19] A. P. Dhawan, R. M. Rangayyan, and R. Gordon. “Image restoration by Wiener deconvolution in limited-view computed tomography”. In: *Applied optics* 24.23 (1985), pp. 4013–4020. DOI: 10.1364/AO.24.004013.

[20] T. M. Buzug. “Introduction to Computed Tomography”. In: Springer, 2008.

[21] L. A. Feldkamp, L. Davis, and J. W. Kress. "Practical cone-beam algorithm". In: *JOSA A* 1.6 (1984), pp. 612–619.

[22] K. M. Hanson. "Detectability in the presence of computed tomographic reconstruction noise". In: *Application of Optical Instrumentation in Medicine VI*. Vol. 127. 1977, pp. 304–312.

[23] J. Sauvola and M. Pietikäinen. "Adaptive document image binarization". In: *Pattern recognition* 33.2 (2000), pp. 225–236. DOI: 10.1016/S0031-3203(99)00055-2.

[24] I. A. Cunningham and R. Shaw. "Signal-to-noise optimization of medical imaging systems". In: *J Opt Soc Am A* 16.3 (1999), pp. 621–632. DOI: 10.1364/josaa.16.000621.

[25] J. H. Siewerdsen et al. "Spektr: A computational tool for x-ray spectral analysis and imaging system optimization". In: *Med Phys* 31.11 (Oct. 2004), pp. 3057–3067. DOI: 10.1118/1.1758350.

[26] H. Illers, E. Buhr, and C. Hoeschen. "Measurement of the detective quantum efficiency (DQE) of digital X-ray detectors according to the novel standard IEC 62220-1". In: *Radiat Prot Dosimetry* 114.1-3 (2005), pp. 39–44. DOI: 10.1093/rpd/nch507.

[27] K. Bavendiek and U. Zscherpel. "Limits of radiographic testing. New high contrast sensitivity technique-examples and analysis by system theory; Die Grenzen der radiographischen Pruefung. Eine neue Hochkontrastempfindlichkeitstechnik-Beispiele und systemtheoretische Analyse". In: *ZfP Zeitung* 105 (2007).

[28] U. Ewert et al. "Visibility of Image Quality Indicators (IQI) by Human Observers in Digital Radiography in Dependence on Measured MTFs and Noise Power Spectra". In: *ECNDT 2018* (2018).

[29] M. J. Tapiovaara and R. Wagner. "SNR and DQE analysis of broad spectrum X-ray imaging". In: *Phys Med Biol* 30.6 (June 1985), pp. 519–529. DOI: 10.1088/0031-9155/30/6/002.

[30] A. Koch et al. "X-ray imaging with submicrometer resolution employing transparent luminescent screens". In: *J Opt Soc Am A* 15.7 (1998), pp. 1940–1951. DOI: 10.1364/JOSAA.15.001940.

[31] H. Hopkins. "The frequency response of a defocused optical system". In: *Proceedings of the Royal Society of London. Series A. Mathematical and Physical Sciences* 231.1184 (1955), pp. 91–103.

[32] J. Guigay. "Analyse spectrale (frequences spatiales) dúne figure de diffraction de Fresnel". In: *CR Acad. Sc. Paris* 284 (1977), pp. 193–196.

[33] D. Pelliccia et al. "Experimental characterization of the coherence properties of hard x-ray sources". In: *Optics express* 19.9 (2011), pp. 8073–8078.

[34] *IEC 62220-1: Medical electrical equipment – Characteristics of digital X-ray imaging devices – Part 1: Determination of the detective quantum efficiency*. IEC. Oct. 2003.

[35] B. Jähne. "EMVA 1288 Standard for Machine Vision: Objective specification of vital camera data". In: *Optik & Photonik* 5.1 (2010), pp. 53–54. DOI: 10.1002/opph.201190082.

[36] G. Patatoukas et al. "The effect of energy weighting on the SNR under the influence of non-ideal detectors in mammographic applications". In: *Nucl Instr Meth A* 569.2 (2006), pp. 260–263.

[37] R. Cahn et al. "Detective quantum efficiency dependence on x-ray energy weighting in mammography". In: *Med Phys* 26.12 (1999), pp. 2680–2683. DOI: 10.1118/1.598807.

[38] I. A. Cunningham, M. Westmore, and A. Fenster. "A spatial-frequency dependent quantum accounting diagram and detective quantum efficiency model of signal and noise propagation in cascaded imaging systems". In: *Med Phys* 21.3 (1994), pp. 417–427. DOI: 10.1118/1.597401.

[39] A. van der Schaaf and J. van Hateren. "Modelling the Power Spectra of Natural Images: Statistics and Information". In: *Vision Research* 36.17 (Sept. 1996), pp. 2759–2770. DOI: 10.1016/0042-6989(96)00002-8.

[40] J. Berglund et al. "Energy weighting improves dose efficiency in clinical practice: implementation on a spectral photon-counting mammography system". In: *Journal of Medical Imaging* 1.3 (2014), p. 031003.

[41] R. K. Swank. "Absorption and noise in x-ray phosphors". In: *Journal of Applied Physics* 44.9 (Sept. 1973), pp. 4199–4203. DOI: 10.1063/1.1662918. URL: https://doi.org/10.1063%2F1.1662918.

[42] J. Tanguay, H. K. Kim, and I. A. Cunningham. "The role of x-ray Swank factor in energy-resolving photon-counting imaging". In: *Med Phys* 37.12 (Nov. 2010), pp. 6205–6211. DOI: 10.1118/1.3512794. URL: https://doi.org/10.1118%2F1.3512794.

[43] A. Korn et al. "Investigation of charge carrier transport and charge sharing in X-ray semiconductor pixel detectors such as Medipix2". In: *Nucl Instr Meth A* 576.1 (2007), pp. 239–242.

[44] S. N. Friedman et al. "A simple approach to measure computed tomography (CT) modulation transfer function (MTF) and noise-power spectrum (NPS) using the American College of Radiology (ACR) accreditation phantom". In: *Med Phys* 40.5 (Apr. 2013), p. 051907. DOI: 10.1118/1.4800795.

[45] F. J. Harris. "On the use of windows for harmonic analysis with the discrete Fourier transform". In: *Proceedings of the IEEE* 66.1 (1978), pp. 51–83.

[46] G. Heinzel, A. Ruediger, and R. Schilling. "Spectrum and spectral density estimation by the Discrete Fourier transform (DFT), including a comprehensive list of window functions and some new at-top windows." In: (2002). URL: http://hdl.handle.net/11858/00-001M-0000-0013-557A-5.

[47] Y. I. Nesterets et al. "On the optimization of experimental parameters for x-ray in-line phase-contrast imaging". In: *Review of Scientific Instruments* 76.9 (Sept. 2005), p. 093706. DOI: 10.1063/1.2038107.

[48] T. E. Gureyev et al. "Some simple rules for contrast, signal-to-noise and resolution in in-line x-ray phase-contrast imaging". In: *Optics express* 16.5 (2008), pp. 3223–3241.

[49] A. Balles et al. "Propagator based formalism for optimizing in-line phase contrast imaging in laboratory X-ray setups". In: *Review of Scientific Instruments* 87.9 (Sept. 2016), p. 093707. DOI: 10.1063/1.4962713.

[50] C. Fella et al. "Hybrid setup for micro-and nano-computed tomography in the hard X-ray range". In: *Review of Scientific Instruments* 88.12 (2017), p. 123702.

[51] O. Hemberg, M. Otendal, and H. M. Hertz. "Liquid-metal-jet anode electron-impact x-ray source". In: *Applied Physics Letters* 83.7 (Aug. 2003), pp. 1483–1485. DOI: 10.1063/1.1602157.

[52] M. Otendal et al. "A 9keV electron-impact liquid-gallium-jet x-ray source". In: *Review of Scientific Instruments* 79.1 (Jan. 2008), p. 016102. DOI: 10.1063/1.2833838.

[53] M. Stampanoni et al. "High resolution X-ray detector for synchrotron-based microtomography". In: *Nucl Intrum Meth A* 491.1 (2002), pp. 291–301. DOI: 10.1016/S0168-9002(02)01167.

[54] C. Fella et al. "Laboratory source based full-field x-ray microscopy at 9 keV". In: *AIP Conference Proceedings* 1696.1 (2016), p. 020025. DOI: 10.1063/1.4937519. eprint: http://aip.scitation.org/doi/pdf/10.1063/1.4937519.

[55] P. Stahlhut et al. "Laboratory x-ray microscopy using a reflection target system and geometric magnification". In: 463.1 (2013), p. 012007.

[56] J. Jakubek. "Energy-sensitive X-ray radiography and charge sharing effect in pixelated detector". In: *Nucl Instr Meth A* 607.1 (2009), pp. 192–195.

[57] C. Stritt. "Assessment and Correction of Image Degradation in MeV Cone Beam Computed Tomography". PhD thesis. ETH Zurich, 2017.

[58] K. Popper. *The logic of scientific discovery*. Routledge, 2005. DOI: 10.4324/9780203994627.

A. Appendix

A.1. Incomplete work: Sufficient image quality

This section describes work on sufficient image quality which did not give easily understandable results. It is meant as a starting point for further work.

Sufficient image quality is here meant to describe an evaluation which derives image quality thresholds for the detection of specific objects. The well known work on this topic was done by Rose [24, 28], although these derivations only consider the object area and some do not even consider modulation transfer effects.

Here, a simple detection model is assumed in which the average gray value inside the area of the object to detect is considered. Detecting an object is therefore done by thresholding this average. The value and variance of this mean value are used to signify the image quality, similar to SNR.

To simplify the computation, we assume that the image has white noise.

If the object (detail) has a density function $\rho_o(x)$, then we can extend eq. (3.24) to compute average signal and noise:

$$\overline{s^2} = \left(\int \mathrm{d}x \; \rho_o(x) I\kappa(\rho * h_s * h_n^{-1})(x) \right)^2 \tag{A.1}$$

$$\overline{n^2} = \int \mathrm{d}x \; \rho_o(x) n^2 \tag{A.2}$$

$$SNR_o = \frac{\overline{s^2}}{\overline{n^2}} \tag{A.3}$$

Where h_s is the signal PSF. A sufficient detection threshold for SNR_o then depends on the desired reliability of the measurement. It is impossible to provide generally usable thresholds, as the cost of false positive and false negative errors varies by a large amount between different applications. In this model, a blurring PSF "transports" amplitude out of the object area and therefore reduces the signal strength and SNR_o. The effect of this transport is weaker for larger objects. Amplitude may also be "transported in" from surrounding material.

If we consider the SNR of an object area embedded in material of the same kind, its SNR is not influenced by the PSF of the imaging system. On the other hand, the influences of the PSF is strongest for an object surrounded completely by different material.

The facts discussed above make it difficult to derive a simplified equation that e.g. only depends on the object area. Even if we simplify by only considering objects without surrounding material, the object shape is still a significant influence. Furthermore, the differences between applications make a general formulation largely impossible.

A.2. File attachments

The digital version of this document includes the computer code used for simulations and measurement evaluations in a file attachment. Most of the code is written in Python, with some parts in OpenCl C. This attachment can only be opened by software which supports the PDF standard fully and can be downloaded by clicking on the following symbols:

description	attachment
code notebooks	
tomis Python package (whl), includes pyXIT	
readme for tomis	

The code notebooks are various Jupyter notebooks containing the Python code that was used to generate figures which show simulations (mainly in chapter 3, for example figures 3.3, 3.8 and 3.15).

The different implementations of measurement evaluation algorithms used in this work are gathered into a collection of Python code under the name tomis (TOMographic Imaging Software). It includes several subpackages, one of which is pyXIT (see section 2.4.4). For scientific evaluations, mainly the tomis.evaluation subpackage is of interest. The tomis package is provided in the Python wheel (.whl) format, it can be installed with the `pip` tool.[1] The .whl file is actually a zip file containing all code sources, it can also be used this way. Note that the submodule tomis.control is not included in this file.

[1] Type `pip install [path to whl]` into a command line.

A.3. Poster for pyXIT

(see section 2.4.4 on page 20)

Julius-Maximilians-
UNIVERSITÄT
WÜRZBURG

LRM
LEHRSTUHL
RÖNTGENMIKROSKOPIE

pyXIT: Python GUI Software for CT Imaging, Learning and Experimental Algorithms; Example: Multi Material Phase Retrieval

M. Ullherr[a,*], S. Zabler[a,b], J. Graetz[b] and R. Hanke[a,b]

[a]Lehrstuhl für Röntgenmikroskopie, Universität Würzburg, Josef-Martin-Weg 63, 97074 Würzburg, Germany
[b]Fraunhofer Development Center X-Ray Technology EZRT, Josef-Martin Weg 63, 97074 Würzburg, Germany
software download: www.physik.uni-wuerzburg.de/en/lrm/research/software *maximilian.ullherr@physik.uni-wuerzburg.de

Overview

pyXIT (the Python X-Ray Imaging Tool) is a software for data processing in x-ray computed tomography (CT) imaging, intended for use in a scientific or development context. It was developed because no CT imaging software existed that combined a GUI, fast preview and the ability to integrate existing Python code.
The software is ideally suited for experimental algorithms, hardware or software development and teaching/learning.
The programming language Python is easy to learn and suited for rapid development. Here, it is used as a common interface for algorithms implemented in different ways.
pyXIT is not intended to replace commercial software, as the use cases are different.

Comparable software: ASTRA* [1], pyHST* [2], tomopy* [3] and MuhRec [4] (* no GUI).

Features

- Computed tomography reconstruction with cone FBP
- Plugin-based image filters for 2D and 3D (see right side), extendable by users
- Fast slice preview and parameter sweep for CT and image/volume processing
- Written in Python/PyQt and OpenCl, high CT reconstruction speed
- Multiple input formats (tif, raw, ...)
- Free/libre software: can be inspected and changed by users (FreeBSD license)
- Software parts can be used independently (e.g. OpenCl to Python API layer)

User Interface

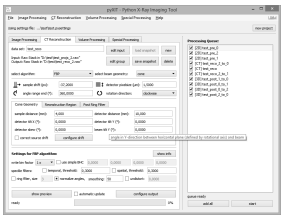

Main window, Cone FBP CT panel with the processing queue enabled

- Control hub, manage multiple data sets
- Set parameters for plugins/algorithms
- Tool tips explain user interface

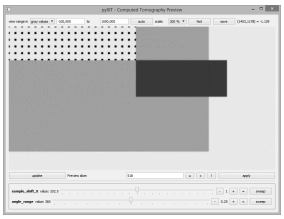

CT preview window (simulated test data)

- Shows result preview
- Selectable area (slice or subvolume)
- Prior results are cached
- Automatic or manual update

Plugin Example: Multi Material Phase Retrieval

This is an example of a custom algorithm which is made easily usable with a pyXIT plugin. It applies phase retrieval to inline phase contrast volume images with multiple materials present in the sample [5].
The sample is a rose stem; ESRF ID19, 1.1 µm pixelsize, 300x600 µm shown.

Top right: Single material phase retrieval produces long range blurring artifacts around the material with the higher absorption (black = calcium oxalate).
Bottom right: Our own algorithm.

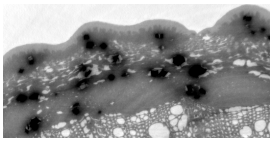

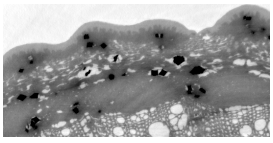

Image Enhancement and Artifact Correction

Enhancing the image quality or removing image artifacts makes the CT images easier to evaluate and use. Artifact correction is necessary in some cases.
The following plugins/features of pyXIT are especially useful for high resolution and inline phase contrast x-ray imaging:

- Wiener deconvolution
- Phase retrieval, multi material [5]
- Ring filters, partial and full rings
- Background variation removal

For the cone FBP CT reconstruction:

- Drift correction from rewind images
- Detector lens distortion correction
- Field of view extension (half-scan)

Processing Examples

Image enhancement for inline phase contrast CT (Click-CT scanner).
Volume slices of a polymer granulate for 3D printing.
0.62 µm voxelsize (2x binned), 400x400 µm shown.

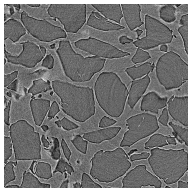

Step 1: CT reconstruction (with simple ring filter)

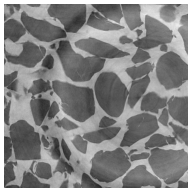

Step 2: Phase retrieval + wiener deconvolution

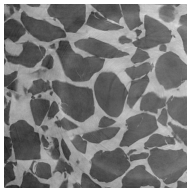

Step 3: Slice ring filters (can be applied in CT)

Drift correction (LRM-LMJ CT setup).
Volume slices of a polymer fiber mesh sample.
Extreme case, up to 30 pixels thermal drift and sample holder defect.

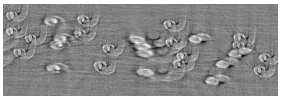

Blur from drifting sample or source

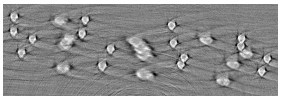

With drift correction from rewind images

Implementation Details

Reconstruction Speed for FBP

(GeForce 980 Ti, without file access)

size	parallel	cone
1000	105 s^{-1}	64 s^{-1}
2000	930 min^{-1}	540 min^{-1}
4000	125 min^{-1}	70 min^{-1}

Size is detector width and nprojs, speed is given in slices per time.

Blockwise Volume Processing

Basic problem: The volume image is too large to fit into RAM due to memory overhead.
Solution: Divide the volume into overlapping blocks, process them in parallel. Speed up the FFT by choosing side lengths in $2^k 3^m 5^n$ ($k \geq 3$). Algorithms must have a known range, but need not be adjusted otherwise.

For both, file access is efficient and concurrent, up to 110 MB/s for Gbit LAN NAS.

References

[1] W. van Aarle et al. In: *Ultramicroscopy* 157 (2015). DOI: 10.1016/j.ultramic.2015.05.002.
[2] A. Mirone et al. In: *NIM B* 324 (2014). DOI: 10.1016/j.nimb.2013.09.030.
[3] D. Gürsoy et al. In: *J. Synchr. Rad.* 21.5 (2014). DOI: 10.1107/S1600577514013939.
[4] A. P. Kaestner. In: *NIM A* 651.1 (2011). DOI: 10.1016/j.nima.2011.01.129.
[5] M. Ullherr and S. Zabler. In: *Optics Express* 23.25 (2015). DOI: 10.1364/OE.23.032718.

Presented at the DIR2019, International Symposium on Digital Industrial Radiology and Computed Tomography, 2 – 4 July 2019 in Fürth, Germany | | Generated using LaTeX/tikzposter